Commissioning and Sensitivity Studies for the SuperNEMO Demonstrator Module

Lauren Dawson
University College London

Submitted to University College London in fulfilment
of the requirements for the award of the
degree of **Doctor of Philosophy**

May 12, 2023

Declaration

I, Lauren Dawson, confirm that the work presented in this thesis is my own. Where information has been derived from other sources, I confirm that this has been indicated in the thesis.

Lauren Dawson

Abstract

The SuperNEMO experiment will search for neutrinoless double-beta decay. It is a tracker-calorimeter detector, designed to reach a $0\nu\beta\beta$ half life sensitivity of $T_{1/2} > 10^{26}$ years, corresponding to an effective Majorana neutrino mass of 50 - 100 meV.

Successful operation of the SuperNEMO tracker requires a precise mixture of gases to be supplied continuously to the detector volume. The purpose of the gas system is to control the fractions of gases, at a given flow rate. Improvements have been made to meet the basic requirements of a safe, radio-pure, remotely monitored and controlled gas-delivery system.

The SuperNEMO demonstrator module is the first phase of the experiment, with 7 kg of ^{82}Se. Construction and commissioning of the module is well underway, with first data expected in 2022. In preparation for data taking, sensitivity studies have been performed on simulated data.

Results of the sensitivity and relative errors of two key backgrounds, ^{208}Tl and ^{214}Bi, for the demonstrator module will be presented here. The enhancement of the gas system and integration with slow control will also be presented.

Acknowledgements

I would like to begin by expressing my sincere gratitude to my supervisor, Prof. David Waters, without whose continued support, guidance, belief and (seemingly) unending patience, this thesis would not have been completed. A deep thank you is owed to the Spreadbury family for funding my PhD. Thank you also to Derek Attree who was there to help me with all of the hardware tasks undertaken. It was a pleasure to learn from him, and I always enjoyed his company in the workshop. The analysis work undertaken as part of this PhD would not have been possible without the advice and guidance of Dr. Cheryl Patrick. I really appreciate all the time taken to discuss the best approach.

I have many happy memories from my time spent in the D25 office, and am grateful to all of its occupants over the years. A particular thanks is owed to Vincenzo Monachello for always bringing much needed energy, joy, and silliness into the room (along with far too many plastic bottles). Thank you to the one and only Xin Ran Liu who I first met when I began my MSci studies at UCL, and always made me feel very welcome.

At times, the journey towards finishing this thesis was incredibly challenging. I could not have overcome these moments without the help of many people who have supported me in different ways. My heartfelt thanks to Anastasia Basharina-Freshville for always being there to listen, to encourage, and to be a shoulder to cry on. I am honoured to have met her. Thank you to Ashwin Chopra for his friendship, understanding, and ability to push me outside of my comfort zone. To the Intelligent Yoga Teacher Training (IYTT) Queens, I extend my gratitude for supporting me through a very difficult time and helping me find myself again.

I owe an enormous thanks to my parter, Andy Thain, whose nonchalance has helped me keep things in perspective, and who is always able to make me smile. Thank you for putting up with me during these last few months. I am grateful

also, to our golden retriever Harley, for always acting the fool, and for staring at me when I have been writing too long and need to walk her.

Finally, my deepest gratitude goes to my family. Thank you for being there to support me, no matter my choices, and for reminding me to be compassionate towards myself.

Dedicated to my wonderful Grandad, Chris Custons-Cole, who passed away peacefully on July 4th 2022. I have never known someone with such unbounded love and creativity. He will be deeply missed.

Vive la révolution!

Impact Statement

In the field of particle physics, the impact of this work is an increased understanding of how to constrain key internal backgrounds to the SuperNEMO experiment, important for its search for neutrinoless double-beta decay. The simulation studies undertaken during the course of this thesis provide initial estimations of the sensitivity of the SuperNEMO demonstrator to some of the key backgrounds, ^{214}Bi and ^{208}Tl present in the source foil. Relative errors on the activities as a function of exposure are also calculated for ^{214}Bi throughout the detector volume, and ^{208}Tl in the source foil. These are explored for the target background activities, but also (for the first time) the most recent activity measurements. With full detector commissioning now underway, these results give an indication of how long an exposure is needed to confirm the background activity levels present within the detector.

In addition to the analysis work, the development of hardware and software for the monitoring of the SuperNEMO gas system has a great impact on the successful running of the experiment. Remote monitoring of key variables is essential for ensuring that the correct mixture of gas is supplied to the detector at the correct flow rate. If flow rates were to drop or the supply run out, this could increase contaminant build up in the detector. If there is a fault in the system, it needs to be detected immediately. Furthermore, if an engineer is not on site, it must be possible to remotely operate the gas system to make it safe.

For the remote monitoring of the gas system at the Laboratoire Souterrain de Modane (LSM) in France, a Raspberry-Pi was used. Successful remote operation of Raspberry-Pi devices in non-conventional environments can have impact across a wide range of industries outside of academia. Raspberry-Pi's are highly customisable, cheap, light, and compact devices. This enables the use of computers in situations where they cannot usually be installed. As an example, they are already used for information screens and digital signage. With the ability to attach sensors, such as cameras, it can become a powerful internet of things device.

Finally, the data analysis skills gained during the completion of the analysis allowed the author to begin a career as a data coach for Level 4 Data Analyst Apprenticeship. There is currently a digital skills gap, and a lack of diversity in these roles. The apprenticeship opens up opportunities for young people, and established professionals, to develop these skills, applying them to their roles across a variety of industries.

Contents

List of figures **11**

List of tables **17**

1 Introduction **20**

2 Theoretical Background **22**

2.1 Standard Model Neutrinos 22

2.1.1 A History 22

2.1.2 Neutrino Interactions 23

2.1.3 Neutrino Properties 23

2.1.4 Neutrino Flavours 24

2.2 Neutrinos Beyond the Standard Model 25

2.2.1 Neutrino Oscillations 25

2.2.2 Oscillation Parameters 30

2.2.3 Neutrino Mass Hierarchy 31

2.2.4 Neutrino Mass 31

2.2.5 Constraints on Neutrino Mass 35

3 Double-Beta Decay **42**

3.1 Beta Decay 42

3.2 Two Neutrino Double-beta Decay 44

3.2.1 Neutrinoless Double-beta Decay 46

4 Current Status of $\beta\beta$ Decay Experiments **54**

4.1 Detection Principles 54

4.1.1 Isotope Selection 55

4.1.2 Low Background 57

4.2 Overview of Approaches . . . 58
4.2.1 Germanium Semiconductor Detectors . . . 59
4.2.2 Cryogenic Bolometers . . . 61
4.2.3 Liquid Scintillators . . . 63
4.2.4 Xenon Time Projection Chamber (TPC) . . . 66

5 The SuperNEMO Experiment 70
5.1 NEMO-3 . . . 70
5.2 SuperNEMO Detector Geometry . . . 73
5.3 Source Foil . . . 74
5.4 Tracker . . . 75
5.5 Calorimeter . . . 76
5.6 Magnetic Field and Shielding . . . 77
5.7 Current Status of the SuperNEMO Demonstrator . . . 79
5.7.1 Calorimeter Commissioning . . . 79
5.7.2 Tracker Commissioning . . . 84
5.7.3 Next Steps . . . 86

6 SuperNEMO Sensitivity to Backgrounds 88
6.1 SuperNEMO Backgrounds . . . 88
6.1.1 External Backgrounds . . . 88
6.1.2 Radon Background . . . 89
6.1.3 Internal Backgrounds . . . 91
6.1.4 Background Activities . . . 92
6.1.5 Background Topologies . . . 93
6.2 Simulation and Reconstruction using SuperNEMO Analysis Software . . . 94
6.2.1 SuperNEMO Software . . . 95
6.2.2 Sensitivity Module . . . 98
6.2.3 Alpha Finder . . . 98
6.3 Internal Background Sensitivities . . . 103
6.3.1 Event Generation . . . 103
6.3.2 Background Efficiency . . . 104
6.3.3 ^{208}Tl in the Foil . . . 109
6.3.4 ^{214}Bi in the Foil . . . 111
6.4 Relative Errors on Background Activities . . . 115
6.4.1 Search for Discriminating Variable . . . 115

6.4.2 Pseudo Data & Fitted Activities . . . 119
6.4.3 Relative error on ^{208}Tl activities . . . 129

7 The SuperNEMO Gas System **136**
7.1 Gas System Operation . . . 137
7.2 Additional of Ethanol . . . 138
7.3 System Requirements . . . 142
7.4 Additional Hardware . . . 143
7.4.1 Testing the Readout Chain . . . 144
7.4.2 Electronics Crate . . . 146
7.5 Slow Control & Monitoring . . . 150
7.5.1 Software . . . 153
7.5.2 Applications . . . 156
7.5.3 Use in the Commissioning of the Demonstrator Module . . . 166

8 Conclusions **172**

Bibliography **175**

List of figures

2.1 Charged current and neutral current neutrino interactions 24

2.2 Measurements of the hadron production cross-section around the Z resonance 26

2.3 Diagram showing the‘normal’ and ‘inverted’ hierarchies for the absolute neutrino masses 31

2.4 Feynman diagram showing the propagator $-m_D\overline{\nu_L}\nu_R$ for the Dirac mass term 32

2.5 Feynman diagram showing the propagator $-m_L\overline{\nu}_L^C\nu_L$ for the Majorana mass term 33

2.6 Electron energy spectrum in the β-decay of tritium 36

2.7 Effective Mass Measurements from Tritium Decay Experiments 37

2.8 Magnetic Adiabatic Collimation + Electrostatic Filter (MAC-E-Filter) 38

2.9 Baryon Density Distributions with massless and massive neutrinos . . 39

2.10 Effective Majorana neutrino mass as a function of the lightest neutrino mass 40

3.1 Predictions of the masses of even A atomic mass number from the Semi-Empirical Mass Formula (SEMF) 44

3.2 Feynman Diagram of the $2\nu\beta\beta$ decay 45

3.3 Feynman Diagram of the $0\nu\beta\beta$ decay 46

3.4 Distribution of the sum of the electron energies for $2\nu\beta\beta$ and $0\nu\beta\beta$. 47

3.5 Feynman diagram illustrating Schechter-Valle theorem 47

3.6 Feynman diagram of $0\nu\beta\beta$ mediated by light neutrino exchange . . . 48

3.7 Feynman diagram of $0\nu\beta\beta$ mediated by Majoron emission 49

3.8 Feynman diagram of $0\nu\beta\beta$ mediated by right-handed current 50

3.9 Comparing distributions for the different mass mechanisms 51

3.10 Nuclear matrix elements for light-neutrino exchange from different many-body methods 52

3.11 $0\nu\beta\beta$ decay half-lives for different isoptopes, using several nuclear matrix element approaches 53

4.1 ^{208}Tl and ^{214}Bi decay schemes 57

4.2 GERmanium Detector Array (GERDA) setup 60

4.3 Kamioka Liquid Scintillator Antineutrino Detector (KamLAND)-Zen setup 64

4.4 Sudbury Neutrino Observatory (SNO)+ detector 66

4.5 Schematic of TPC and 3D drawing of Enriched Xenon Observatory (EXO-200) 67

4.6 Next Enriched Xenon Observatory (EXO) (nEXO) potential sensitivity [1] 68

4.7 Cross section of the Neutrino Experiment with a Xenon TPC (NEXT)-100 detector [2] 69

5.1 NEMO-3 setup 71

5.2 Single electron energy and opening angle for metallic ^{100}Mo 72

5.3 An exploded view of the SuperNEMO demonstrator module and an illustration of the detection principles 74

5.4 Diagram of the layout of a tracking cell and an example of the electrical readout when a charged particle traverses the cell. 75

5.5 Two Optical Moduless (OMs) configurations used for SuperNEMO main walls, and Veto and x-walls respectively 77

5.6 Image of the copper coil installed around the demonstator module . . 78

5.7 Schematic of the anti-radon tent and pure iron shielding 78

5.8 Colour scale map of the timing offsets measured for each of the calorimeters in the Italian main wall. 80

5.9 Colour scale map of the timing resolutions measured for each of the calorimeters in the Italian main wall. 81

5.10 Absolute energy calibration of OMs using ambient radioactivity sources . . . 82

5.11 ^{207}Bi source, containing envelope and diagram of deployment system in SuperNEMO demonstrator . . . 82

5.12 Electron energy spectrum of ^{207}Bi, expected energies (points) and simulated detector response . . . 83

5.13 Charge spectra during commissioning of the detector, with and without ^{207}Bi sources . . . 84

5.14 Top down diagram of the SuperNEMO tracker and calorimeter showing the assigned areas and associated high voltage crates . . . 85

5.15 Examples of the reconstructed first light background events in the SuperNEMO detector . . . 85

5.16 Heat map of tracker cell hits in the SuperNEMO detector with ^{207}Bi sources present . . . 86

5.17 Heat map of tracker cell hits in the SuperNEMO detector with ^{207}Bi sources present, with a selection on the triggering of a chosen calorimeter . . . 87

6.1 Mechanisms by which externally created gammas can mimic the two electron event topology . . . 89

6.2 The two naturally occurring decay chains that emit ^{222}Rn and ^{220}Rn respectively . . . 90

6.3 Mechanisms by which two electron events can be created from beta decay inside the foils . . . 91

6.4 Visualisation of a simulation of a 1e event in the SuperNEMO demonstrator. . . . 96

6.5 Summary of the Falaise simulation and reconstruction pipeline. . . . 96

6.6 Visualisation of a simulation of a 1e1γ event in the SuperNEMO demonstrator. . . . 97

6.7 Visualisation of a typical alpha track originating in the source foil. . . . 99

6.8 Alpha reconstruction for one, two and more than two delayed Geiger hits. . . . 101

6.9 Alpha track length and projected track length for one delayed hit. . . . 102

6.10 Alpha track length and projected track length for two delayed hits. . . . 102

6.11 Alpha track length and projected track length for more than two delayed hits. . . . 103

6.12 Total gamma energy spectrum for ^{214}Bi and ^{208}Tl events in the bulk of the foil. . . . 107

6.13 Reminder of the ^{214}Bi and ^{208}Tl decay schemes . . . 108

6.14 SuperNEMO Demonstrator Background Sensitivity to ^{208}Tl as a function of time . . . 110

6.15 SuperNEMO Demonstrator Background Sensitivity to ^{208}Tl and ^{214}Bi as a function of time . . . 112

6.16 Receiver Operating Characteristic (ROC) curve result for a Boosted Decision Tree (BDT) trained to separate the $0\nu\beta\beta$ signal from the internal backgrounds . . . 113

6.17 ROC curve result for a multi-class BDT trained to separate out each type of internal background . . . 114

6.18 Zoomed view of SuperNEMO Demonstrator Background Sensitivity to ^{208}Tl and ^{214}Bi as a function of time . . . 114

6.19 Alpha track lengths for ^{214}Bi events in the foil bulk, foil surface and tracker wires . . . 118

6.20 Reference activity distributions for ^{214}Bi in the bulk, surface and tracker, weighted by the target activities and summed . . . 120

6.21 Example pseudo experiment for target ^{214}Bi activity . . . 121

6.22 Pseudo data histograms for alpha track lengths, before and after smoothing . . . 121

6.23 Example pseudo experiment for target ^{214}Bi activity after an exposure of 410 days, with TFractionFitter results . . . 122

6.24 Fitted activities after 10^5 runs for ^{214}Bi events in the foil bulk, foil surface and tracker wires. . . . 124

6.25 Fitted activities after 10^5 runs for ^{214}Bi events in the foil bulk, with an exposure of 1000 days . . . 125

6.26 TFractionFitter calculated activities plotted against varying input activities for ^{214}Bi on the surface of the foil . . . 126

6.27 Example pseudo experiment for target ^{214}Bi activity after an exposure of 180 days, with TFractionFitter results . . . 127

6.28 Fitted activities after 10^5 runs for ^{214}Bi events in the foil bulk, foil surface and tracker wires, with a bulk activity of 4.1 mBq. 128

6.29 Plot of relative errors on ^{214}Bi activities with varying exposures for a foil bulk activity of 4.1 mBq. 129

6.30 Example pseudo experiment for ^{214}Bi activity of 1.8 mBq and exposure of 180 days, with TFractionFitter results 130

6.31 Plot of relative errors on ^{214}Bi activities with varying exposures for a foil bulk activity of 1.8 mBq. 130

6.32 Electron energy and total gamma energy for 1eNγ events from ^{214}Bi and ^{208}Tl with an electron energy cut of > 0.5MeV. 131

6.33 Example pseudo experiment for 370 µBq ^{208}Tl in the bulk of the foil, and combined ^{214}Bi activity, with TFractionFitter results 132

6.34 Plot of relative errors on 370 µBq of ^{208}Tl in the foil bulk and the combined ^{214}Bi activity in the foil bulk, on the surface of the foil and on the tracker wires. 133

6.35 Fitted activities after 10^5 runs for ^{214}Bi and ^{208}Tl events in the foil bulk. 134

6.36 Fitted activities after 10^5 runs for ^{214}Bi combined in the foil bulk. . . 135

7.1 Flow diagram of the gas system configuration 139

7.2 Dependence of ethanol volume fraction on temperature and pressure . 141

7.3 Connections between gas system sensors and readout computer 143

7.4 Raspberry-Pi 2 Model B 144

7.5 Readout chain for data transfer to Raspberry-Pi 145

7.6 Analogue-Digital Converter (ADC) output vs temperature during ice water tests. 146

7.7 Schematics for the crate panel design 147

7.8 Connections from gas system to the electronics crate 148

7.9 Final location of the electronics crate in the gas system rig 148

7.10 Photo of the Pimoroni Pan-Tilt HAT 149

7.11 Workflow of the SuperNEMO Control & Monitoring System (CMS) . 150

7.12 Flow diagram of the client-server communications 152

7.13 Information flow from server method call to hardware device. 152

7.14 Graphical User Interface (GUI) for the gas system. 155

7.15 Ice forming on the cooling element of the EK20 unit 157

7.16 Diagram of the setup of the Haake DL30 thermal water bath, with the EK20 cooling coil and temperature probes 157

7.17 Graphical display of the water bath temperatures from ProSys client 158

7.18 Graphical display of the water bath temperatures from ProSys client, during EK90 testing 159

7.19 Barometric pressure USB data logger 160

7.20 Ambient pressure fluctuations over a four hour period at the LSM on the 7th of June 2017 161

7.21 Ambient pressure fluctuations at the LSM over a four hour period on the 8th of June 2017 162

7.22 Ambient pressure fluctuations at the LSM over a 6 day period in June 2017 162

7.23 Plot from the client during pressurisation of the Bulleur Primaire (primary bubbler) (BP) with ethanol. 163

7.24 Plot from the client during pressurisation of the BP without ethanol. 164

7.25 First order polynomial fitted to data recorded from pressurisation of the BP with ethanol present. 164

7.26 First order polynomial fitted to data recorded from pressurisation of the BP without ethanol present. 165

7.27 Pressurisation over time during the filling of the ethanol bubbler to $\approx 6\ \ell$ and $11\ \ell$. 167

7.28 Comparison of the expected ethanol level vs the measured ethanol level 168

7.29 Gas system in position at the LSM 168

7.30 Configuration of gas system supply and exhaust lines 169

7.31 Schematics of the gas top inputs to the detector and the exhausts. . . 170

7.32 Example of the plots created from regular gas system monitoring during tracker use at the LSM 171

List of tables

2.1 Summary of oscillation parameters 30

4.1 Summary of commonly used $\beta\beta$ decaying isotopes [3] 56

5.1 Summary of the key experimental properties of the NEMO-3 experiment and the planned improvements for SuperNEMO 73

6.1 Summary of the different scenarios studied for the analysis of the sensitivity to internal backgrounds. 92

6.2 Table showing the radon suppression factors and achievable activities (a) in the SuperNEMO tracker for different input flow rates . . . 93

6.3 Vertex generators used for the simulation of different background samples 104

6.4 ^{214}Bi Foil Bulk efficiencies for different cut selections made based on topology, electron energy and vertex position 105

6.5 ^{214}Bi Tracker Wires efficiencies for different cut selections made based on topology, electron energy and vertex position 105

6.6 ^{208}Tl Foil Bulk efficiencies for different cut selections made based on topology, electron energy and vertex position 106

6.7 ^{214}Bi Foil Bulk and ^{208}Tl Foil Bulk efficiencies for varying total gamma energy cuts. 108

6.8 Table of the calculated efficiencies for ^{214}Bi in the foil and the tracker wires, as well as ^{208}Tl in the foil, with the expected time for one event 109

6.9 ^{214}Bi Foil Bulk efficiencies for different cut selections made based on topology, and vertex position 116

6.10 ^{214}Bi Foil Surface efficiencies for different cut selections made based on topology, and vertex position 116

6.11 ^{214}Bi Foil Tracker Wires efficiencies for different cut selections made based on topology, and vertex position 117

6.12 Table of example TFractionFitter (TFF) results when fitting pseudo ^{214}Bi data with the bulk, surface and tracker background contributions. These are compared with the known initial fractions. 123

6.13 Table of example calculated activities for ^{214}Bi from TFF results, compared with known input activities. 123

6.14 Table of the ^{214}Bi activities, alongside the mean, standard deviations, and calculated relative error from the Gaussian fit. 124

6.15 Table of the ^{214}Bi activities alongside the mean, standard deviations, and calculated relative error for case 2 from the Gaussian fit. 127

7.1 Gas system monitoring variables 151

Chapter 1

Introduction

In the field of particle physics, the Standard Model (SM) has been a very successful theory. Many experiments have validated its predictions, including the discovery of the Higgs Boson. Despite this, it fails to account for the properties of the most abundant matter particle in our Universe, the neutrino. Neutrinos remain the least well understood particle, owing to the fact that they only interact via the weak interaction, and have extremely small cross sections. Whilst the SM predicts these particles should be massless, the experimental observation of neutrino oscillations between three distinct flavours requires a non zero mass. As a result, there are several other unknown properties, including the value and ordering of their mass eigenstates. In addition to this, the very nature of the neutrino is unknown. The theory of weak interactions suggests it is possible for neutral particles, like the neutrino, to be either Dirac or Majorana particles. If it is a Dirac particle, the anti-neutrino would be distinct from the neutrino, as is the case for all other SM fermions. However, in the case that it is a Majorana particle, the neutrino is its own anti-particle.

The search for neutrinoless double-beta decay ($0\nu\beta\beta$) provides a mechanism for uncovering the nature of the neutrino, and constraining its mass. It consists of two simultaneous beta-decays from a nucleus, without the emission of neutrinos. It is a lepton-number violating process that is forbidden by the SM. As of yet, only the SM allowed $2\nu\beta\beta$ process has been observed. Given the potential of $0\nu\beta\beta$ to unlock our understanding of the neutrino, it is a field of great interest in particle physics.

The SuperNEMO experiment builds on the knowledge and principles of its predecessor, NEMO-3. It is one of many experimental approaches in the search for $0\nu\beta\beta$. SuperNEMO utilises a modular tracker-calorimeter design around a central, interchangeable, source. This enables three dimensional reconstruction of β-decay electron paths and measurement of individual particle energies. With both Particle Identification (PID) and full kinematic reconstruction, it is possible to reject background events with a high efficiency. In the event of $0\nu\beta\beta$ discovery, these properties also allow SuperNEMO to distinguish between the different underlying $0\nu\beta\beta$ mechanisms. The SuperNEMO demonstrator is now constructed at the LSM, and full detector commissioning is underway.

Chapter 2 begins with an introduction to the theory behind neutrinos and their properties, including that which goes beyond the SM. Current experimental constraints on the mixing angles, mass splittings, and absolute masses are also included. Chapter 3 builds on this theory by discussing double beta-decay and the different mechanisms by which $0\nu\beta\beta$ could occur. In Chapter 4 there is an overview of the different experimental approaches, beginning with a discussion around the key detection principles. Current results from each of these experiments is also presented. Chapter 5 presents the SuperNEMO experiment, starting with an overview of NEMO-3 results and how this informed the development of the SuperNEMO demonstrator. The design of the detector is then discussed, alongside the current status and next steps for the demonstrator module at the LSM.

The author's main contributions to the SuperNEMO experiment are then detailed in Chapter 6 and Chapter 7. Internal and external backgrounds to the SuperNEMO experiment are discussed at the start of Chapter 6, before the analysis software is introduced and sensitivity studies conducted for internal backgrounds. The end of the chapter presents the results of the relative errors for key internal backgrounds as a function of the exposure of the demonstrator. In Chapter 7, the SuperNEMO gas system (introduced in Chapter 5) is discussed in more detail with a focus on the hardware and software required to accurately, and reliably, monitor the system remotely. Examples of the successful operation of this system, and its use in recent commissioning efforts are included. Finally, conclusions are presented in Chapter 8.

Chapter 2

Theoretical Background

"Nothing in life is to be feared, it is only to be understood. Now is the time to understand more, so that we may fear less.."

- Marie Curie

2.1 Standard Model Neutrinos

2.1.1 A History

The history of the neutrino began with the study of radioactive beta decay. Evidence of radioactivity was first discovered in 1896 by Henri Becquerel, with continued research by others such as Marie Curie and Ernest Rutherford. By the end of the 19th century, radioactive emissions had been categorised into three types: alpha, beta and gamma rays. In 1914 James Chadwick measured the energy spectrum of emitted electrons in beta decay [4]. The result of his experiment was controversial. Chadwick found that the electron emitted a continuous energy spectrum, that appeared to go against the energy conservation principle. This problem was left unsolved until 1930, when Wolfgang Pauli proposed that a mysterious, undetectable, new particle could be carrying away the energy [5]. The particle would be weakly interacting, have no charge, and be very light. Pauli initially called this proposed particle a neutron.

In 1932 Chadwick discovered a heavier, electrically neutral particle that he gave the same name. To distinguish the two Edoardo Amaldi named Pauli's particle a

neutrino, meaning 'little neutral one' in Italian. This was then adopted by Enrico Fermi in 1933. Fermi included the neutrino in his theory of beta decay published in 1934 [6], but the particle was not discovered until 26 years after its initial prediction.

The properties that led Pauli to dub the neutrino 'undetectable' kept a discovery out of reach until 1956. To combat the very weak interaction, a large flux of the hypothetical particle was required. This was achieved by using nuclear reactors. Clyde L. Cowan and Frederick Reines observed the signature of an anti-neutrino interaction in their inverse-beta decay experiment [7].

2.1.2 Neutrino Interactions

Neutrinos are detected indirectly by observing the products of two types of interactions. SM neutrinos can only interact via the electroweak force. The mediators of the weak force are the $W^{\pm}$ and Z^0 bosons. In the case of Charge Current (CC) interactions, the neutrino scatters off the electron or the nucleus (as in Figure 2.1b) and the final state lepton can be observed. This can be seen in Figure 2.1a and Figure 2.1b. In this case the initial neutrino is converted into the equivalent charged lepton. The cross section for the nucleon interaction is generally larger than the electron scattering case. Figure 2.1c and Figure 2.1d show Neutral Current (NC) interactions where the neutrino does not convert but instead transfers energy and momentum to the target particle. When the neutrino scatters off an electron the energy transfer is measured by the recoil of the electron. NC scattering from a nucleon can result in recoil or even the break-up of the target nucleon.

2.1.3 Neutrino Properties

Experiments in the the 1950s discovered several important properties of the neutrino. In 1956 Chien-Shiung Wu conducted an experiment to test whether parity was conserved in weak interactions. In both electromagnetic and strong interactions parity conservation had already been established. The experiment was proposed after reports from Lee and Yang that as of 1956 there was no strong evidence to reject or support parity violation or conservation [8]. To determine

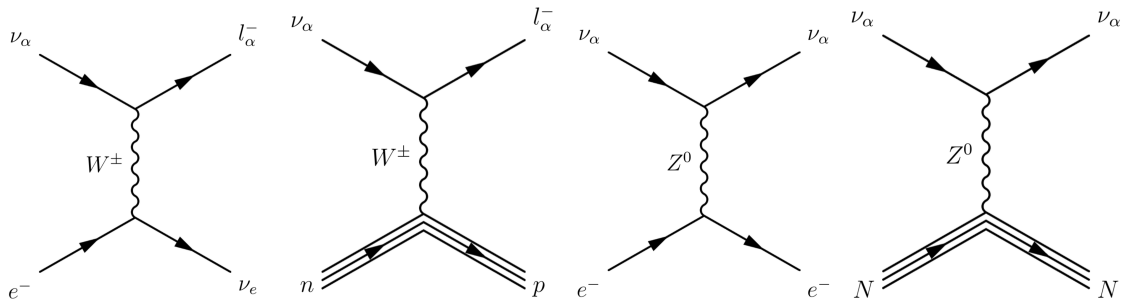

(a) CC ν-e^- scattering **(b)** CC ν-N scattering **(c)** NC ν-e^- scattering **(d)** NC ν-N scattering

Figure 2.1: Feynman diagrams showing the different types of neutrino interactions with electrons and nucleons.

whether parity was violated, Wu polarised ^{60}Co nuclei using a magnetic field. The polarisation of the ^{60}Co nuclei gives rise to a forward-backward asymmetry in the case of parity violation. The following decay was observed:

$$^{60}_{27}\mathrm{Co} \rightarrow {}^{60}_{28}\mathrm{Ni} + e^- + \bar{\nu_e} + 2\gamma.$$

When the ^{60}Co beta decays it releases an electron and anti-electron neutrino as shown above. The nickel is in an excited state and decays emitting two photons. As electromagnetic interactions were known to respect parity conservation, when the electrons did not match the distribution of the gammas, this was evidence that parity is not conserved in weak interactions [9].

Another important property of the neutrino was discovered in 1957 by Maurice Goldhaber. A neutrino and a photon are released in the electron capture of an ^{152}Eu nucleus. Neutrinos were found to be left handed by measuring the polarisation of the gamma in the case where it was emitted in the opposite direction to the neutrino [10].

All of the above experiments involved electron neutrinos (ν_e). Other flavours of neutrino will be introduced below.

2.1.4 Neutrino Flavours

Before 1962 only one type of neutrino had been observed, the electron neutrino. Given the existence of higher mass charged leptons such as the muon , it was ex-

pected the neutrino would have associated counterparts. The muon neutrino was first discovered by researchers at Brookhaven National Laboratory. This was the first experiment to use an an accelerator as its source of neutrinos. Muon tracks produced by the CC interaction were observed in a spark chamber, providing evidence of the muon neutrino (ν_μ) [11].

The discovery of the tau particle in 1975 by scientists at Stanford Linear Accelerator Center (SLAC) indicated the possibility of a third generation of neutrino [12]. It was not until 2000 that the Direct Observation of the NU Tau (DONUT) experiment detected the tau neutrino (ν_τ). DONUT used a 800 GeV beam of protons from the Tevatron at Fermilab, fired at a tungsten beam dump. The short decay time of the τ leads to a clear track signature featuring a kink after 2 mm. This was observed in a nuclear emulsion [13].

The above experiments identified three generations of neutrino, known as flavours, ν_e, ν_μ, and ν_τ. Strong evidence confirming the number of light neutrino species came from 4 experiments at the Large Electron Positron collider (LEP). This was done by precisely measuring the decay width of the Z^0 boson. A prediction for the number of neutrinos can be calculated by comparing the results with the SM expectations. Three cases for the predicted number of light neutrino species are shown in Figure 2.2. There is strong agreement between the average results and the 3 neutrino curve. When combining results from all four electron-positron experiments, the measured number of neutrinos was $N_\nu = 2.9840 \pm 0.0082$ [14].

With the discovery of the above properties, neutrinos were incorporated into the SM as massless particles. The next section (§2.2) will discuss results that pushed the study of neutrinos beyond the SM predictions.

2.2 Neutrinos Beyond the Standard Model

2.2.1 Neutrino Oscillations

Motivated by kaon oscillations, Bruno Pontecorvo first proposed neutrino oscillations in 1957. Initially he investigated the idea of neutrino to antineutrino transi-

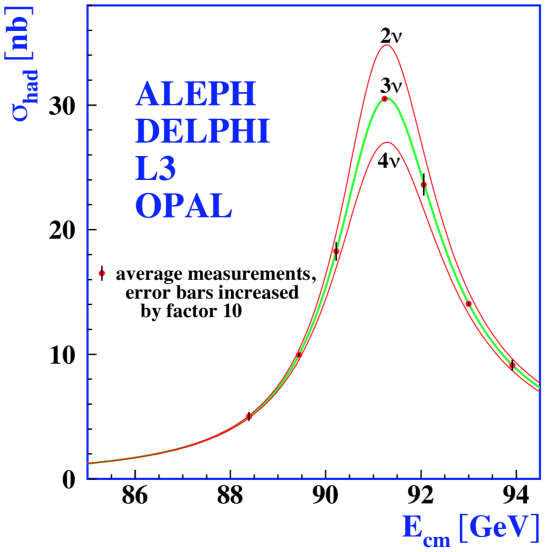

Figure 2.2: Measurements of the hadron production cross-section around the Z resonance. Results are average measurements across the four experiments, ALEPHI, DELPHI, L3 and OPAL [14]

tions [15]. Whilst this has not been observed, it paved the way for further theoretical work on oscillations.

The first indication of oscillatory behaviour came from the Homestake Experiment in 1968. This was a solar neutrino detector located 4850 ft underground at a gold mine in South Dakota. Neutrinos from the sun were detected through the CC interaction with chlorine nuclei as below.

$$\nu_e + {}^{37}\mathrm{Cl} \rightarrow {}^{37}\mathrm{Ar} + e^-$$

The argon was then extracted and counted (using the decay of ^{37}Ar) to measure the number of electron neutrino captures. A surprising result was observed. Only a third of the neutrinos predicted by the current solar models were detected [16]. This discrepancy between theory and experimental findings became known as the 'solar neutrino problem'. It was initially thought to be a problem with the Homestake experiment, but similar results were found by later experiments in the 1990s.

As the Homestake experiment was only sensitive to one flavour of neutrino, ν_e, the reduction in expected flux could be due to neutrinos at the detector arriving

as a different flavour. In 1962, Maki, Nakagawa and Sakata explored the idea of neutrino masses and mixing. They proposed that the fields of the weak neutrinos ν_e and ν_μ were connected with those of fixed masses or 'true neutrinos', ν_1 and ν_2. Whilst neutrino oscillations were not specifically mentioned, there was a suggestion of 'virtual transmutation' between ν_e and ν_μ [17]. In Pontecorvo's second neutrino oscillation paper he developed these ideas into neutrino flavour oscillation $\nu_e \Leftrightarrow \nu_\mu$. A year before the results from Homestake were published, Pontecorvo suggested that due to flavour oscillation the measured flux of ν_e from the sun could be two times smaller than expected [18].

Confirmation of Pontecorvo's theory, and the resolution to the so called 'solar neutrino problem' came in 2001. SNO was a solar neutrino experiment 2100 m underground in Sudbury, Canada. The heavy water Cherenkov detector observed the neutrino flux from ^{8}B decays in the sun. Neutrinos were observed via reactions with the deuterium nuclei in the CC and NC, and via atomic electrons in the Elastic Scattering (ES) channel [19]:

$$\nu_e + d \rightarrow p + p + e^-$$
$$\nu_x + d \rightarrow p + n + \nu_x$$
$$\nu_x + e^- \rightarrow \nu_x + e^-$$

CC reactions are only sensitive to electron neutrinos, whereas NC reactions have an equal sensitivity to all flavours (x =e,μ,τ). Expressed another way, only electron neutrinos can partake in both NC and CC interactions. As previously seen in the Homestake experiment, SNO saw a deficit in the CC channel. This was indicative of the fact that electron neutrinos could be changing flavour. Furthermore, the neutrino flux from the NC were consistent with the standard solar model. This was strong evidence in favour of neutrino oscillations.

Observations of oscillations in atmospheric neutrinos confirmed the model in 1998. Super-Kamiokande conducted this study using a 50 kt water Cherenkov detector. When cosmic rays collide with particles in the upper atmosphere, hadronic showers occur and neutrinos are produced in these decays. Given the weakly interacting properties of neutrinos, they can pass through the Earth. Therefore it was possible for Super-Kamiokande to detect neutrinos from all directions. Upward-going neutrinos, those that have passed through the Earth, have travelled a longer

distance than the downward-going neutrinos produced above the detector. A large deficit was measured in the number of upward-going ν_μ. This was consistent with neutrinos oscillating ($\nu_\mu \Leftrightarrow \nu_\tau$) as they propagate [20].

Oscillation Phenomenology

The discovery of oscillations ended the long standing belief that neutrinos were massless. Oscillations can occur due to the mixing of the flavour and mass eigenstates. This can be expressed as shown in Equation (2.1), where $|\nu_\alpha\rangle$ and $|\nu_i\rangle$ are the flavour and mass states respectively. α are the neutrino favours (e,μ,τ) and i are the mass eigenstates (m_1, m_2, m_3).

$$|\nu_\alpha\rangle = \sum_i U^*_{\alpha i} |\nu_i\rangle \tag{2.1}$$

The superposition of the mass eigenstates is the neutrino flavour. U is a unitary leptonic mixing matrix commonly referred to as the Pontecorvo-Maki-Nakagawa-Sakata (PMNS) matrix. To better understand the matrix it can be helpful to show it in the form below (2.2) [21].

$$U = \overbrace{\begin{pmatrix} 1 & 0 & 0 \\ 0 & c_{23} & s_{23} \\ 0 & -s_{23} & c_{23} \end{pmatrix}}^{\text{Atmospheric}} \overbrace{\begin{pmatrix} c_{13} & 0 & s_{13}e^{-i\delta} \\ 0 & 1 & 0 \\ -s_{13}e^{i\delta} & 0 & c_{13} \end{pmatrix}}^{\text{Cross-mixing}} \overbrace{\begin{pmatrix} c_{12} & s_{12} & 0 \\ -s_{12} & c_{12} & 0 \\ 0 & 0 & 1 \end{pmatrix}}^{\text{Solar}} D_M \tag{2.2}$$

Above, $c_{ij} \equiv \cos\theta_{ij}$ and $s_{ij} \equiv \sin\theta_{ij}$. The mixing angle, θ_{ij}, quantifies the extent of mixing between i and j. The Dirac CP-violating phase is δ. The first matrix dominates mixing that occurs in atmospheric neutrinos. Likewise, mixing in solar neutrinos is dominated by the third matrix. The last component in the above is a diagonal matrix (2.3) including the Majorana CP-violating phases α and β [22].

$$D_M = \overbrace{\begin{pmatrix} e^{i\alpha/2} & 0 & 0 \\ 0 & e^{i\beta/2} & 0 \\ 0 & 0 & 1 \end{pmatrix}}^{\text{Majorana CP-violating phases}} \tag{2.3}$$

Equation (2.3) shows the additional phases that are only physical if the neutrino is a Majorana particle (Section 2.2.4).

In a vacuum, the probability of a neutrino oscillating from one flavour to another ($\nu_\alpha \Leftrightarrow \nu_\beta$) can be given by:

$$\begin{aligned} P\left(\nu_\alpha \to \nu_\beta\right) &= \left| \sum_i U^*_{\alpha i} e^{-i m_i^2 \frac{L}{2E}} U_{\beta i} \right|^2 \\ &= \delta_{\alpha\beta} - 4 \sum_{i>j} \Re(U^*_{\alpha i} U_{\beta i} U_{\alpha j} U^*_{\beta j}) \sin^2\left(\Delta m^2_{ij} \frac{L}{4E}\right) \\ &\quad + 2 \sum_{i>j} \Im(U^*_{\alpha i} U_{\beta i} U_{\alpha j} U^*_{\beta j}) \sin\left(\Delta m^2_{ij} \frac{L}{2E}\right) \end{aligned} \tag{2.4}$$

Equation (2.4) demonstrates that when a neutrino of energy E, propagates a distance L it will mix between flavours, as governed by the PMNS matrix and mass splittings ($\Delta m^2_{ij} \equiv m^2_i - m^2_j$).

Simplifying the above to only consider two neutrinos we find:

$$P\left(\nu_\alpha \to \nu_\beta\right) \quad = \quad \sin^2(2\theta_{ij}) \sin^2\left(\Delta m^2_{ij} \frac{1.27L}{E}\right), \tag{2.5}$$

where 1.27 assumes units of eV, km, and GeV for m, L, and E respectively. $\frac{L}{E}$ is included in order to work in natural units, where L and E replace time and momentum respectively. An experiment measuring the probability of oscillations between two neutrino flavours is therefore sensitive to the mixing angle in the PMNS matrix and mass splittings.

2.2.2 Oscillation Parameters

Solar neutrino experiments over the years have constrained the values of θ_{12} and Δm^2_{21}. Atmospheric neutrino results inform the values of θ_{23} and Δm^2_{31}. The current best values for oscillation parameters are shown in Table 2.1. The values shown are global fits from multiple neutrino experiments.

Parameter	Best-fit	3σ
$\sin^2\theta_{12}, \Delta m^2_{31(32)} > 0$	0.305	$0.265 - 0.347$
$\sin^2\theta_{12}, \Delta m^2_{32(31)} < 0$	0.303	$0.264 - 0.345$
$\Delta m^2_{21}[10^{-5}\text{eV}^2]$	7.34	$6.92 - 7.90$
$\sin^2\theta_{23}, \Delta m^2_{31(32)} > 0$	0.545	$0.436 - 0.595$
$\sin^2\theta_{23}, \Delta m^2_{32(31)} < 0$	0.551	$0.439 - 0.596$
$\Delta m^2_{31(23)}[10^{-3}\text{eV}^2]$	2.485 (2.465)	$2.389 - 2.578$ $(2.374 - 2.556)$
$\sin^2\theta_{13}, \Delta m^2_{31(32)} > 0$	0.0222	$0.0201 - 0.0241$
$\sin^2\theta_{13}, \Delta m^2_{32(31)} < 0$	0.0223	$0.0203 - 0.0243$

Table 2.1: Summary of the best fit values and 3σ ranges of the oscillation parameters. Global fit from [23] of all current neutrino oscillation data. Where the last two entries are for the different hierarchies.

Reactor and accelerator experiments have also contributed significantly to the determination of the mixing angles (θ_{13}) and mass splittings to a high precision. They are sensitive to the cross-mixing section of Equation (2.2). Reactor experiments such as Daya Bay and Double Chooz measure the flux of neutrinos from nuclear reactors. Examples of accelator experiments are T2K and NOνA. Both use neutrino beams from accelerators and have near and far detectors, allowing the energy E and propagation distance L to be tuned.

Overall there has been great success in measuring the oscillation parameters. However, some uncertainties still remain. The sign of Δm^2_{31} is undetermined. Little is known about the CP-violating phases, δ, α, and β. It is possible to search for CP violation in oscillation experiments by comparing the different probabilities of observing e^+ and $\overline{\nu}_e$ with e^- and ν_e at the far end of the detector. There is a hint that $\delta \cong 3\pi/2$, but in general the CP symmetry in the lepton sector continues to be uncertain [24].

2.2.3 Neutrino Mass Hierarchy

It is clear from Equation (2.5) that oscillation experiments are only to sensitive Δm^2. Determining the sign of the splitting therefore requires further information. As discussed above, the sign of Δm^2_{32} is unknown, and this results in two possible situations. If $\Delta m^2_{32} > 0$ then $m_3 > m_2 > m_1$ which is known as 'normal hierarchy'. However, in the case of an 'inverted hierarchy', $\Delta m^2_{32} < 0$ and $m_2 > m_1 > m_3$. Both scenarios are shown in Figure 2.3.

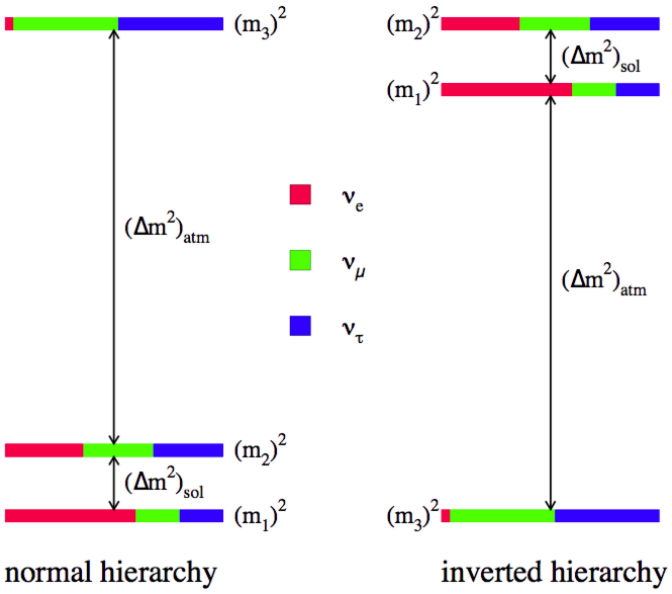

Figure 2.3: Diagram showing the'normal' and 'inverted' hierarchies for the absolute neutrino masses [25]

Solar experiments have determined the value of Δm^2_{21}. Combining this with the study of how different flavour neutrinos oscillate through a dense medium, it was possible to determine the sign of Δm^2_{21} as positive.

2.2.4 Neutrino Mass

Oscillations have provided clear evidence that neutrinos have a non-zero mass. When the SM was formulated neutrinos were considered massless. Incorporating massive neutrinos requires an extension to the SM. This involves adding mass

terms to the SM Lagrangian. The various methods of doing so are discussed in the following sections.

Dirac Mass

Quarks and charged leptons get their mass through the coupling of the left-handed (LH) and right-handed (RH) fields with the Higgs field. The SM Lagrangian only includes neutrinos with LH chirality (ν_L). Therefore, a minimal extension is to introduce RH neutrinos (ν_R), implementing a so called Dirac mass term. These RH neutrinos do not participate in weak interactions and are only influenced by gravity, so they are known as 'sterile'. The Dirac Lagrangian is shown in Equation (2.6).

$$\mathcal{L}_D = -m_D \left(\overline{\nu}_L \nu_R + \overline{\nu}_R \nu_L\right) \tag{2.6}$$

where m_D is a constant mass term, representing the Yukawa coupling to the Higgs field. As shown in Figure 2.4 the first term in Equation (2.6) transforms an incoming RH neutrino into a LH one. The second term, $-m_D \overline{\nu}_R \nu_L$ performs the reverse. In both cases the lepton number is conserved as there is one incoming and outgoing neutrino. Whilst the simplicity of this extension is appealing it presents several problems. The RH sterile neutrinos by nature are extremely difficult to detect. Furthermore, to justify the observed small neutrino masses, a very small coupling (compared with the other Yukawa couplings) to the Higgs field is required. This is considered to be unnatural in the Dirac formalism.

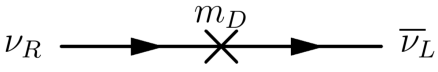

Figure 2.4: Feynman diagram showing the propagator $-m_D \overline{\nu_L} \nu_R$ for the Dirac mass term [26]

Majorana Mass

Ettore Majorana proposed an alternative to the Dirac mass in 1937 [27], that involved only two active neutrinos. Majorana sought to describe massive neutrinos

using only LH fields, thus avoiding introducing 'steriles'. This is only possible for neutrinos as they carry no electric charge. The Majorana mass term that can be included in the SM Langrangian is shown in Equation (2.7).

$$\mathcal{L}_M = -\frac{1}{2} m_L \left(\overline{\nu}_L^C \nu_L + \overline{\nu}_L \nu_L^C \right) \tag{2.7}$$

where m_L is a constant mass term. It is worth noting that Equation (2.7) can also be written entirely in terms of RH fields. The first coupling in the equation destroys an incoming neutrino and creates an anti-neutrino (Figure 2.5).

Figure 2.5: Feynman diagram showing the propagator $-m_L \overline{\nu}_L^C \nu_L$ for the Majorana mass term [26]

A Dirac neutrino has lepton number $L = +1$, and the anti-neutrino $L = -1$, therefore the above diagram would result in $\Delta L = \pm 2$ violating lepton number conservation. In Equation (2.7), ν_L^C is the charge conjugate of ν_L and satisfies

$$\nu_L^C = C \overline{\nu}_L^T \tag{2.8}$$

where T is the transpose matrix, and C is the charge conjugation matrix. It can also be seen that ν_L^C is RH in Equation (2.9).

$$\nu_L^C = P_R \nu^C \tag{2.9}$$

Here P_R is the RH chiral projection operator. It is therefore possible to write the Majorana field purely in terms of LH fields. Using the property shown in Equation (2.8) we can write the following:

$$\nu = \nu_L + \nu_R = \nu_L + C \overline{\nu}_L^T = \nu_L + \nu_L^C \tag{2.10}$$

Taking the charge conjugation of Equation (2.10) we find:

$$\nu^C = (\nu_L + \nu_L^C)^C = \nu_L^C + \nu_L = \nu \tag{2.11}$$

The charge conjugation of the neutrino field is itself, or equally the Majorana neutrino is its own anti-particle. As the charge conjugation flips the sign of the electric charge, the above must only be possible for electrically neutral particles, i.e. neutrinos [28]. Whist this method has some appeal by not relying on sterile neutrinos, Equation (2.7) is not a proper mass term as $m_L \overline{\nu}_L^C \nu_L$ is not gauge invariant. It becomes necessary to introduce a Higgs triplet with isospin $I = -1$ and hypercharge $Y = -2$, which does not exist in the SM. Alternatively, we can look again at incorporating a RH neutrino in a different mass mechanism, the so-called See-Saw mechanism [29].

See-Saw Mechanism

In this mechanism the Dirac and Majorana mass terms mentioned in the previous sections are brought together in a single Lagrangian.

$$\begin{aligned}\mathcal{L}_{M+D} &= \mathcal{L}_D + \mathcal{L}_{M_R} \\ &= -\frac{1}{2}\left[m_D \overline{\nu}_L \nu_R + m_D \overline{\nu}_R \nu_L + m_R \overline{\nu}_R^C \nu_R\right] + \text{h.c.} \\ &= -\frac{1}{2}\left(\overline{\nu}_L \overline{\nu}_R^c\right) \mathcal{M} \begin{pmatrix} \nu_L^c \\ \nu_R \end{pmatrix} + \text{h.c.}\end{aligned} \tag{2.12}$$

where $\mathcal{M}$ is the neutrino mass matrix given by

$$\mathcal{M} = \begin{pmatrix} 0 & m_D \\ m_D & m_R \end{pmatrix} \tag{2.13}$$

Here m_R is the RH Majorana neutrino mass. The physical masses of the neutrinos are determined by diagonalising Equation (2.13) and finding the eigenvalues.

$$m_{1,2} = \frac{m_R \pm \sqrt{m_R^2 + 4m_D^2}}{2} \tag{2.14}$$

It is possible to reduce the above to two masses, by considering m_D to be the same order of magnitude as the other fermions in the SM, and m_R much heavier

$(m_R \gg m_D)$.

$$m_1 \approx m_R \tag{2.15}$$

$$m_2 \approx \frac{m_D^2}{m_R} \tag{2.16}$$

The See-Saw mechanism predicts a light neutrino state that is observed in experiments. and a heavy RH sterile Majorana neutrino. Examining Equation (2.16) it can be seen that the theory offers an explanation for the extremely small masses of the observed neutrinos. If m_R is sufficiently large, i.e. on the Grand Unified Theory (GUT) scale $\sim 10^{15}$ GeV, this allows for light neutrinos with a mass $\sim$ meV [29]. The Majorana mass features in both eigenvalues, Equation (2.15) and Equation (2.16). Therefore, the neutrino is taken to be a Majorana particle with the consequence of lepton number violation discussed previously. It is also possible that the matter/anti-matter asymmetry we observe in the Universe, could have descended from the heavy RH neutrino decaying in a way that violates CP conservation.

2.2.5 Constraints on Neutrino Mass

As mentioned in §2.2.2, oscillation experiments have measured two of the mass splittings to a high precision, but are not sensitive to the absolute mass scale. Constraints on the neutrino mass come from tritium beta decay, cosmological measurements, and neutrinoless double-beta decay. All of these methods provide upper limits on the absolute neutrino mass. Oscillation experiments provide a lower bound on the heaviest mass state.

Tritium Beta Decay

When a nucleus β^- decays it creates an electron and an anti-electron neutrino. The available energy is shared between the two products. As the neutrino has a finite mass it will have an effect on the electron energy spectrum. To best observe this it is useful to study nuclei that have a small Q-value, that is, a small mass difference between the parent and daughter atoms. If this is the case then a small neutrino mass will have a relatively large change in the electron energy spectrum.

Tritium (^{3}H) is an isotope of Hydrogen which β-decays as shown below.

$$^3\mathrm{H} \rightarrow {}^3\mathrm{He}^+ + \mathrm{e}^- + \overline{\nu}_e \tag{2.17}$$

A low Q-value of 18.6 keV, accompanied by a reasonable half-life of 12.3 years, has led to the best neutrino mass limits on effective neutrino mass [30]. Figure 2.6 shows how a massive neutrino of 1 eV distorts the electron energy spectrum, compared to the massless ν_e case.

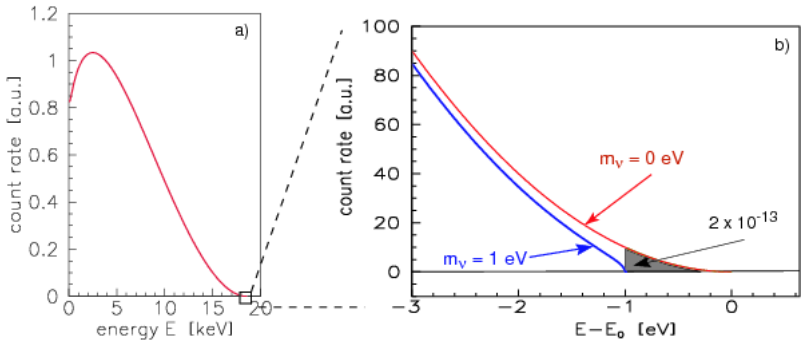

Figure 2.6: Electron energy spectrum in the β-decay of tritium. The complete spectrum is shown in a) and a narrow region around the endpoint in b) [31]

Extracting the neutrino mass from β-decay experiments is possible as they are sensitive to the effective mass squared. If the mass splittings are small compared to the mass scale, such that $m_1 \approx m_2 \approx m_3$, then the effective mass squared of the anti-electron neutrino can be written as below [32]

$$\langle m_\beta^2 \rangle = \sum_{i=1}^{3} |U_{ei}|^2 m_i^2 \tag{2.18}$$

where U_{ei} is part of the PMNS matrix relating the ν_e flavour state to the mass states, i. The shift seen in Figure 2.6 arises from a small non-zero $\langle m_\beta^2 \rangle$.

Previous experiments Mainz [33] and Troitsk [34] have set a limit on the effective mass, $\langle m_\beta \rangle < 2$ eV (95% confidence level). Improvements in the measurement of the effective mass squared are shown in Figure 2.7.

It can be seen from Figure 2.7 that the Mainz and Troitsk experiments dramatically increased the sensitivity and precision of the tritium decay measurements. This was the result of a new type of spectrometer, known as the MAC-E-Filter.

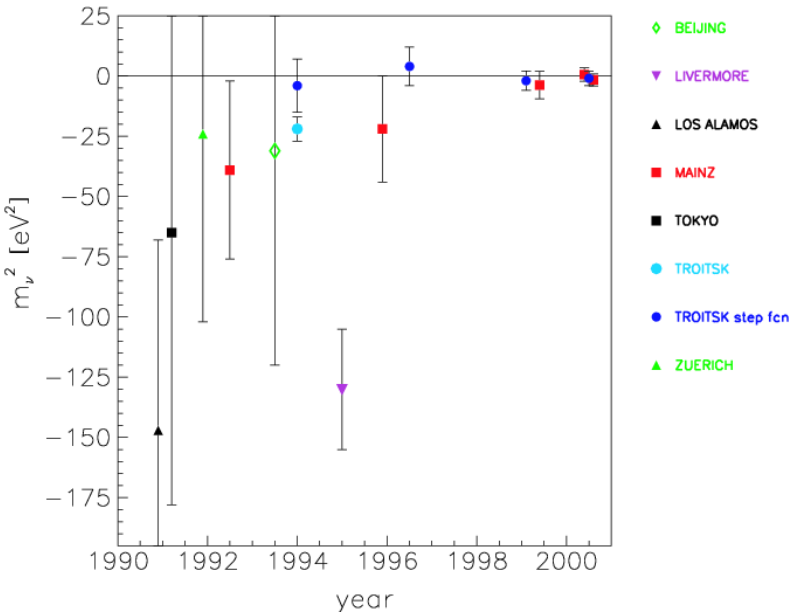

Figure 2.7: Measurements of the effective neutrino mass squared from tritium beta decay experiments over a decade [31].

Figure 2.8 shows the setup and principle of this spectrometer. The overall purpose of the tuneable spectrometer is to act as a high-energy pass filter. Beta decay electrons are emitted from the tritium source on the left hand side. As charged particles, entering a magnetic field, they exhibit cyclotron motion, and are guided by the magnetic field (B_{max}) into the main body of the spectrometer. The B-field (B_{min}) then drops, transforming the electrons into a broad beam, with longitudinal motion. Cylindrical electrodes set up an electrostatic potential ($q\overrightarrow{E}$)that opposes the motion of the electrons. Electrons with an energy greater than a set threshold overcome the electrostatic barrier, and are accelerated and collimated on to the detector on the right hand side. By varying the energy threshold and counting the electrons arriving at the detector, the β-spectrum can be measured in integrating mode [31].

The Karlsruhe Tritium Neutrino experiment, KATRIN, has been designed to be sensitive to an effective neutrino mass of 0.2 eV (90% confidence level). It is based on the same principles shown in Figure 2.8 and builds on experienced gained from earlier MAC-E-Filter experiments. KATRIN now holds the best limit on the effective neutrino mass. After the first four-week science run they have found a

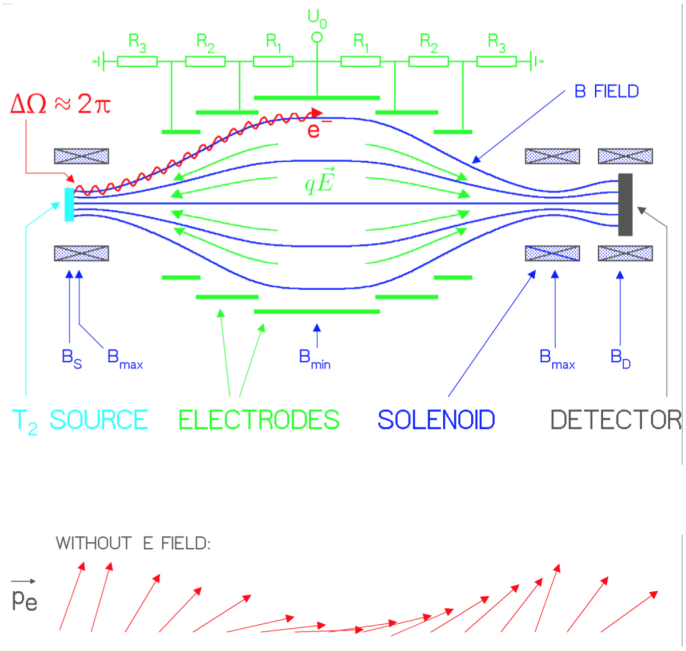

Figure 2.8: Principle of the MAC-E-Filter, with the setup shown on top, and below the momentum transformation [31].

limit of $\langle m_\beta \rangle < 1.1$ eV (90% confidence level) [35]. The second phase of running improved on this with a result of $\langle m_\beta \rangle < 0.9$ eV (90% confidence level), giving a combined result for the first and second campaigns of $\langle m_\beta \rangle < 0.8$ eV (90% confidence level) [36].

Cosmology

Cosmological observations provide an upper limit on the sum of the neutrino masses $\sum m_i$. Massive neutrinos affect large scale structure formation in the Universe. Their contribution to the critical density seen today can be summarised in Equation (2.19), where 94.22 is used to convert the critical density into units of g/cm^3 using the Hubble and gravitational constants.

$$\Omega_\nu = \frac{\sum m_\nu}{94.22h^2} \tag{2.19}$$

Figure 2.9 shows baryon density simulations for $\Omega_\nu = 0$ and $\Omega_\nu = 0.04$. It demonstrates that massive neutrinos suppress the growth of density perturba-

tions through free streaming (relativistic movement from regions of high density to low). Figure 2.9a appears to be more evolved with deep gravitational potential wells, whereas in Figure 2.9b the structure has been washed out [37].

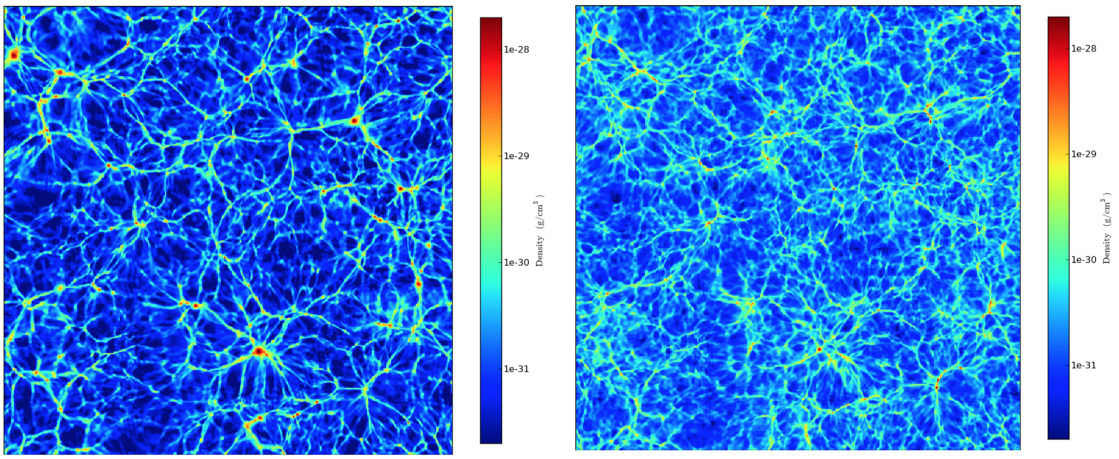

(a) Simulation with $\sum m_\nu = 0$ neutrinos **(b)** Simulation with $\sum m_\nu = 1.9$ eV

Figure 2.9: Slices of baryon density distribution, $200h^{-1}$ Mpc wide. (a) with $\sum m_\nu = 0$ and (b) with $\Omega_\nu = 0.04$, $\sum m_\nu = 1.9$ eV [37].

Simulations like this can help predict the effects of neutrino mass on observables such as the Cosmic Microwave Background (CMB) power spectrum. The Lyman-α power spectrum provides information on the formation of structures, and is also used in calculations of neutrino mass.

The tightest limits can be found by combining results from many different observables, and hence numerous assumptions. An upper limit of $\sum m_i < 0.11$ eV (95% confidence level) has been found using results from Baryon Oscillation Spectroscopic Survey (BOSS) Lyman-α and Planck CMB data [38]. Results are heavily dependent on the cosmological model. The base model for the above is a flat ΛCDM cosmology with massive neutrinos.

Neutrinoless Double-beta Decay

If the nature of the neutrino is Majorana, then a process called neutrinoless double-beta decay can occur ($0\nu\beta\beta$). Chapter 3 will discuss this exotic nuclear process in detail. If the decay is mediated by light Majorana neutrino exchange (other

models are discussed in Chapter 3), the rate of decay is proportional to the square of the effective Majorana neutrino mass

$$\langle m_{\beta\beta} \rangle \equiv \left| \sum_i U_{ei}^2 m_i \right| \tag{2.20}$$

The current best limits on the effective neutrino mass come from KamLAND-Zen and GERDA phase II with $\langle m_{\beta\beta} \rangle < (0.036 - 0.156)$ eV [39] and $\langle m_{\beta\beta} \rangle < (0.093 - 0.222)$ eV [40] respectively, both with 90% confidence level. The range of values here is due to the uncertainties in the calculations of the Nuclear Mass Element (NME). KamLAND-Zen and GERDA use different $\beta\beta$ decaying isotopes, these are ^{136}Xe and ^{76}Ge respectively.

Figure 2.10 shows the effective Majorana neutrino mass as a function of the lightest neutrino mass. The current best limit from KamLAND-Zen is indicated in

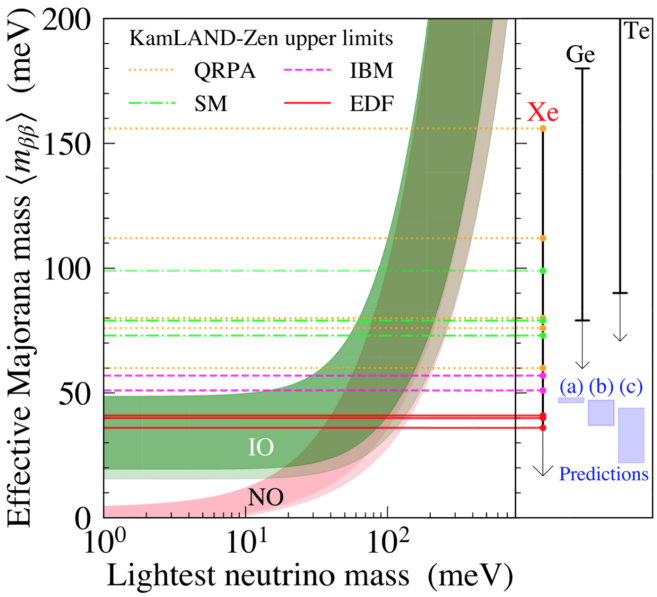

Figure 2.10: Effective Majorana neutrino mass as a function of the lightest neutrino mass. The red and green bands illustrate the possible parameter space for Normal Hierarchy (NH) (NO) and Inverted Hierarchy (IH) (IO) respectively. Regions below the horizontal lines are allowed at a 90% C.L. using results from ^{136}Xe at KamLAND-Zen. In the right panel the limits are shown for different $\beta\beta$ isotopes [39].

the red horizontal line. Previous results effectively eliminated the area of the parameter space where the IH and NH overlap, known as the 'quasi degenerate' re-

gion. The degenerate region is defined as the area where masses » mass splittings. This result is the first in the IH region. Future experiments hope to increase their sensitivity to $\langle m_{\beta\beta} \rangle$ such that the IH region is either ruled out completely, or a discovery is made.

Chapter 3

Double-Beta Decay

"Life need not be easy, provided only that it is not empty."

- Lise Meitner

3.1 Beta Decay

Beta (β) decay is a common radioactive process mediated by the weak force. A quark inside the nucleus interacts with a $W^{\pm}$ boson, changing flavour, and resulting in the transformation of neutron $\Leftrightarrow$ proton. The decay occurs in one or more of the following three modes: β^- where an electron and electron antineutrino are emitted, β^+ with the emission of a positron and electron neutrino, and Electron Capture (EC) with an outgoing electron neutrino but no charged lepton. The generalised forms of these decay modes are shown below, where A is the atomic mass number and Z is the atomic number.

$$ {}^{A}_{Z}\mathrm{X} \rightarrow {}^{A}_{Z+1}\mathrm{Y} + e^- + \bar{\nu}_e \quad (\beta^-) \tag{3.1} $$

$$ {}^{A}_{Z}\mathrm{X} \rightarrow {}^{A}_{Z-1}\mathrm{Y} + e^+ + \nu_e \quad (\beta^+) \tag{3.2} $$

$$ {}^{A}_{Z}\mathrm{X} + e^- \rightarrow {}^{A}_{Z-1}\mathrm{Y} + \nu_e \quad (\mathrm{EC}) \tag{3.3} $$

In several isotopes EC or β^+ modes can be observered. EC can occur when an electron is captured from the inner orbital of the atom, causing a proton to con-

vert to a neutron. The Q-value for the $\beta\beta$ decay must be higher for β^+ due to the production of two e^+ compared with the EC case.

For β-decay to be possible, there must be enough energy to produce the outgoing particles. Therefore the mass of the parent atom must be greater than the combined mass of the daughter atom, and the emitted particles. The masses of nuclei are well approximated by the Bethe−Weizsäcker formula, also known as the Semi-Empirical Mass Formula (SEMF) [41]:

$$M(A,Z) = Zm_p + (A-Z)m_n - E_B, \tag{3.4}$$

where m_p is the mass of the proton, m_n is the mass of the neutron, and E_B is the binding energy of the nucleus. It should be noted that for the atomic mass, as shown on the Figure 3.1 y-axis, a term $Z \times m_e$ is added. The binding energy can be written as:

$$E_B = a_V A - a_S A^{2/3} - a_C \frac{Z^2}{A^{1/3}} - a_A \frac{(A-2Z)^2}{A} - \delta(A,Z), \tag{3.5}$$

where each term represents a correction to the approximation in Equation (3.4). These corrections are terms relating to volume (V), surface (S), Coulomb force (C), asymmetry between numbers of neutrons/protons (A) and pairing (δ(A,Z)). The pairing term accounts for the effect of spin-coupling and is given by [42]:

$$\delta(A,Z) = \begin{cases} \frac{a_p}{A^{1/2}} & \text{Z, N even (A even)} \\ 0 & \text{A odd} \\ \frac{-a_p}{A^{1/2}} & \text{Z, N odd (A even),} \end{cases} \tag{3.6}$$

where a_p is the pairing correction and N is the number of neutrons. Combining equations 3.4 and 3.5, for a fixed mass number (A), parabolic curves are generated as a function of atomic number Z. If A is odd then there is only one curve. As seen from the pairing term in Equation (3.6), if A is even then there are two parabolas, shown in Figure 3.1.

Allowed $\beta^\pm$ decays are indicated by the arrows in Figure 3.1. For an isotope at (a) a β^- decay to isotope (b) is energetically allowed, followed by another β^- de-

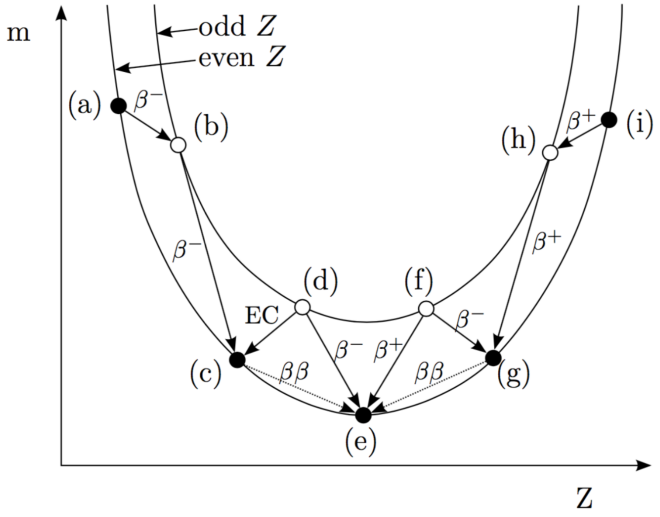

Figure 3.1: Predictions of the masses of even A atomic nuclei from the SEMF. Two parabolas are shown for the case where Z is odd or even. Nuclei with odd Z are shown as white circles, even Z nuclei are filled black circles. Allowed β decays are shown by the arrows [26].

cay to (c). The movement between the two parabolas can be explained by the changing numbers of neutrons/protons resulting from the decay.

3.2 Two Neutrino Double-beta Decay

In this rare process ($2\nu\beta\beta$), two β decays happen simultaneously. The possibility of such a decay was first considered by Goeppert-Mayer in 1935 [43]. In the case of 2 β^- decays, two electrons and two anti-neutrinos are emitted, as shown in Figure 3.2.

Two neutrino double-beta decay is allowed by the SM as both electric charge and lepton number are conserved. For some isotopes, where the single β^- decay is forbidden or highly energetically supressed, $\beta\beta$ can become the main decay mode. Consider the odd Z nuclei at point (d) in Figure 3.1; it can decay to the most stable state (e) either directly by β^- decay or via point (c) through EC. At point (c), a $\beta\beta$ decay to (e) is then possible. The general formula for this decay is:

$$(A, Z) = (A, Z + 2) + 2e^- + 2\bar{\nu}_e, \tag{3.7}$$

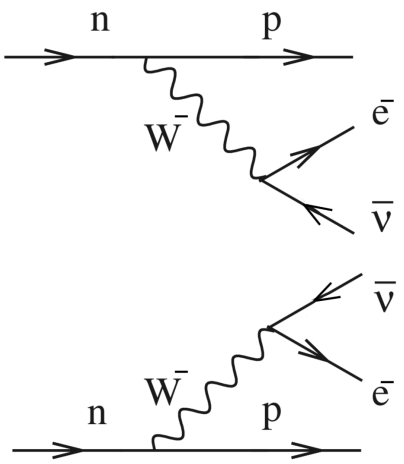

Figure 3.2: Feynman Diagram of the $2\nu\beta\beta$ decay process [44].

Experiments studying $2\nu\beta\beta$ measure the total energy of the outgoing electrons. In the case of SuperNEMO it is also possible to measure the individual energies of the electrons. The two anti-neutrinos emitted in the final state carry away some of the energy, resulting in the total electron energy having a continuous spectrum. The end point of this spectrum is at the Q-value for the $\beta\beta$ decay,

$$Q_{\beta\beta} = M(A, Z) - M(A, Z + 2) - 2m_e. \tag{3.8}$$

As above $M(A, Z)$ is the nuclear mass. There are 35 naturally occurring isotopes that can theoretically undergo $2\nu\beta^-\beta^-$ decay [28]. At the time of writing 11 of these have been observed and their half-life values measured [24]. This number rises to 14 if you consider geochemical channels that have been studied. The half-life for this process can be written as:

$$\left(T^{2\nu}_{1/2}\right)^{-1} = G_{2\nu}(Q_{\beta\beta}, Z)|M_{2\nu}|^2, \tag{3.9}$$

where $G_{2\nu}$ is the four-particle phase space factor and $M_{2\nu}$ is the NME. Whilst the phase space factor can be calculated accurately, the determination of the NME is model dependent and carries a lot of uncertainties. Measuring the half-life values of $2\nu\beta\beta$ across multiple isotopes helps tune the NME calculations.

3.2.1 Neutrinoless Double-beta Decay

A more exotic process is double-beta decay, without neutrino emission ($0\nu\beta\beta$). It was first proposed by Furry in 1939 [45], building on the initial ideas of Goeppert-Mayer. Unlike $2\nu\beta\beta$ there are only two outgoing particles, the two electrons/positrons, as shown in the general formula 3.10.

$$(A, Z) = (A, Z + 2) + 2e^{-} \tag{3.10}$$

Neutrinoless double-beta decay is forbidden in the framework of the SM as it violates lepton number conservation, $\Delta L = 2$. The Feynman diagram for $0\nu\beta\beta$, in Figure 3.3, shows the process mediated by the exchange of a Majorana neutrino.

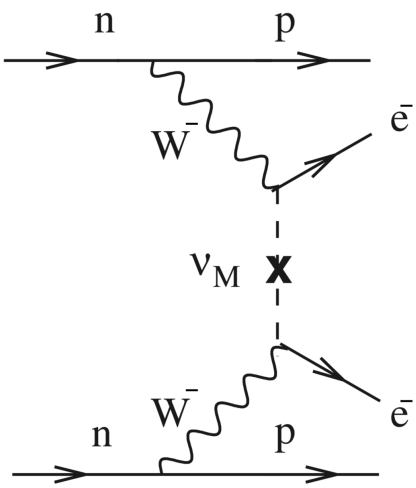

Figure 3.3: Feynman Diagram of the $0\nu\beta\beta$ decay process [44]

In standard double-beta decay, as a result of the two emitted neutrinos, we see a continuous energy spectrum for the emitted electrons all the way up to $Q_{\beta\beta}$. In contrast, for $0\nu\beta\beta$ a discrete peak at the maximum available energy $Q_{\beta\beta}$ would be observed. This can be seen at the end point of the broad $2\nu\beta\beta$ in Figure 3.4. The separation illustrated here requires an excellent energy resolution to reduce the overlap of the $2\nu\beta\beta$ signal with the region of interest.

There are many theoretical mechanisms through which $0\nu\beta\beta$ can occur. These include the neutrino mass mechanism §3.2.1, Majoron emission §3.2.1, and right-handed current §3.2.1. More exotic mechanisms such as extra dimensions, squark mixing, or super-symmetry are not discussed here. In 1980 Schechter and Valle

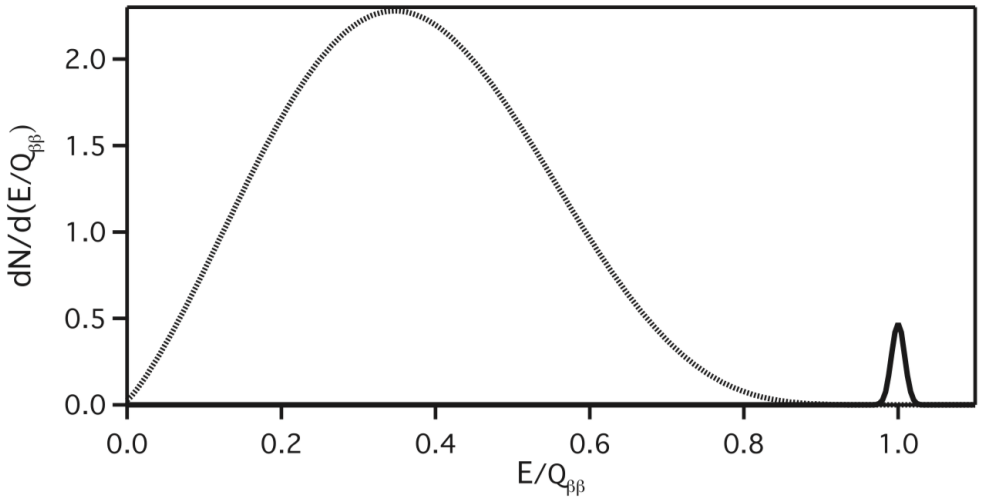

Figure 3.4: Distribution of the sum of the electron energies for $2\nu\beta\beta$ (dotted line) and $0\nu\beta\beta$ (solid line) [44].

demonstrated that regardless of the mechanism involved (exotic or otherwise), any $0\nu\beta\beta$ propagator would result in a non zero Majorana mass Figure 3.5 [22].

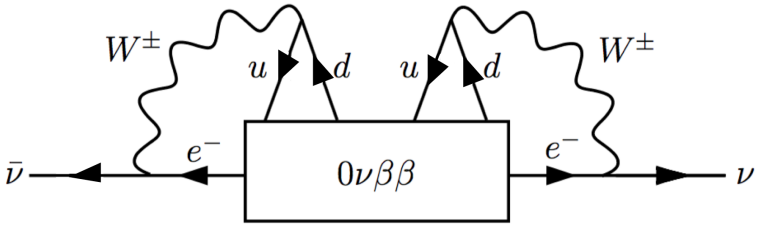

Figure 3.5: Feynman diagram illustrating Schechter-Valle theorem that any $0\nu\beta\beta$ mechanism results in an effective Majorana mass [22].

Neutrino Mass Mechanism

Also known as the light neutrino exchange mechanism, the neutrino mass mechanism is the most common decay model. This is in part due to the fact that it requires the smallest deviation from the SM. This can be seen in Figure 3.6, where each of the vertices conforms to the SM. At the top vertex, a right-handed helicity Majorana neutrino is emitted from a left-handed W-boson. This is then absorbed as a left-handed Majorana neutrino, at the bottom vertex, by another left-handed

W-boson. The spectrum of the summed electron energies is as illustrated in Figure 3.4.

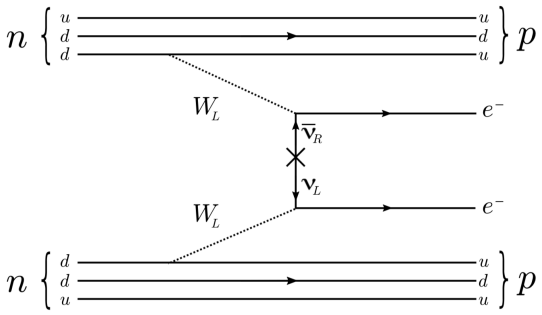

Figure 3.6: Feynman diagram of $0\nu\beta\beta$ mediated by light neutrino exchange

The decay rate for the $0\nu\beta\beta$ process mediated by a light Majorana exchange mechanism is written as,

$$\left(T^{0\nu}_{1/2}\right)^{-1} = G^{0\nu}(Q_{\beta\beta}, Z)|M^{0\nu}|^2\langle m_{\beta\beta}\rangle^2, \tag{3.11}$$

where $G^{0\nu}(Q_{\beta\beta}, Z)$ is the phase space factor for two particles, $|M^{0\nu}|$ is the $0\nu\beta\beta$ NME, and $m_{\beta\beta}$ is the effective Majorana neutrino mass. This can be written as,

$$\begin{aligned}\langle m_{\beta\beta}\rangle &= \left|\sum_i U_{ei}^2 m_i\right| \\ &= \left|\cos^2\theta_{13}(m_1\cos^2\theta_{12} + m_2 e^{i\alpha_1}\sin^2\theta_{12}) + m_3 e^{i(\alpha_2 - 2\delta)}\sin^2\theta_{13}\right|,\end{aligned} \tag{3.12}$$

where θ_{12}, and θ_{13} are the mixing angles from the PMNS matrix (Equation (2.2)). The Dirac CP-violating phase is represented by δ. α_1, α_2 are the Majorana phases (from Equation (2.3)), and m_1, m_2 and m_3 the masses of the corresponding eigenstates. Measurements of the $0\nu\beta\beta$ decay rate are therefore sensitive to the absolute scale of the neutrino mass eigenstates.

Majoron Emission

Lepton number violation in the $0\nu\beta\beta$ decay requires an extension to the SM. Some suggested extensions violate the B-L global symmetry, where B-L is the difference between baryon and lepton numbers. This would lead to the production

of a massless Goldstone boson, or Majoron [46]. The Feynman diagram for such a process can be seen in Figure 3.7.

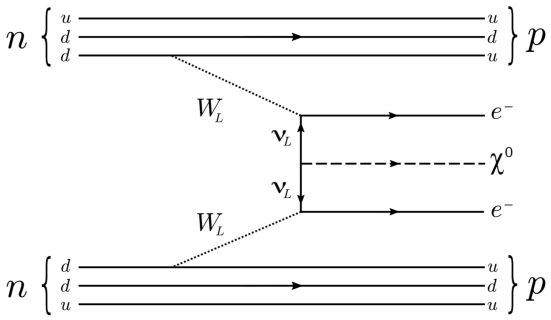

Figure 3.7: Feynman diagram of $0\nu\beta\beta$ mediated by Majoron (χ^0) emission [47].

The production of an additional particle, the Majoron, changes the energy spectrum of the total electron energy. Rather than a monochromatic line, there would be a continuous spectrum for $0\nu\beta\beta$ with varying shape depending on the Majoron model.

Right-handed Current

Another proposed extension to the SM are the Left-Right Symmetric Models (LRSM). The addition of such models could explain the lightness of neutrinos, through the introduction of right-handed neutrinos and the see-saw mechanism. It would also provide a theoretical origin for the maximal parity violation observed in weak interactions [48]. In the SM weak interactions have V-A couplings, and are propagated by a W_L, the left-handed W-boson. LRSM propose a new right-handed gauge boson, or an adaptation to the SM W-boson, becoming an admixture of W_L and W_R. In either case, this allows for V+A vertices in $0\nu\beta\beta$ that do not require a helicity flip [49]. Figure 3.8 shows the $0\nu\beta\beta$ decay mediated by the right-handed current. At the top vertex a W_L boson couples to right-handed anti-neutrino. This is then absorbed at the bottom vertex with no need for a helicity flip.

The summed emitted electron energy creates a spectrum that is identical to the neutrino mass mechanism (Figure 3.4). It is however possible to disentangle this mechanism by looking at quantities such as the angle between electrons and the difference between the electron energies. A comparison of these distributions is

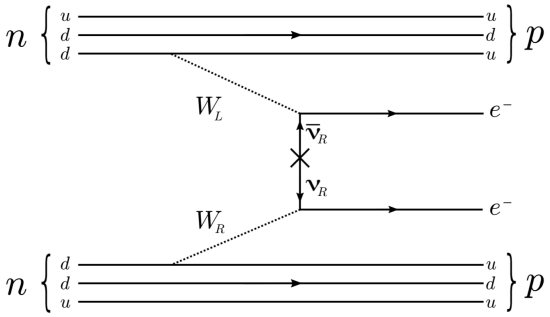

Figure 3.8: Feynman diagram of $0\nu\beta\beta$ mediated by right-handed current

shown in Figure 3.9. The reconstructed distributions are normalised to the theoretical distribution. The differences between reconstructed and theoretical spectra is the result of detector effects, such as multiple scattering in the source foil. This difference is most notable for the right handed current mechanism, where one of the emitted electrons usually has a low energy and so the distribution shape changes.

Due to the above observable differences in distributions, it is advantageous to have the experimental capability to measure the individual energies of the electron. Likewise, being able to reconstruct the angle between the emitted electrons affords the opportunity to distinguish the mechanism if $0\nu\beta\beta$ is observed. The tracker-calorimeter technique of the SuperNEMO experiment allows for both of these distributions to be studied.

Nuclear Mass Element (NME)

As discussed in Section 2.2.5, a large source of uncertainty in the measurement of the decay rate comes from the nuclear model used to calculate the NME. Different theoretical decay structures, produce different outcomes for the NMEs. Figure 3.10 shows the variations and ergo the uncertainties introduced by the approximate solutions of the many-body problem. Calculating accurate uncertainties on each of the theoretical models is also a challenge. In some cases, it is decided by collaborations not to include error bars.

It is informative to also look at the variations in the $0\nu\beta\beta$ half life for different experimental isotopes when using each of the NME methods. The results of this

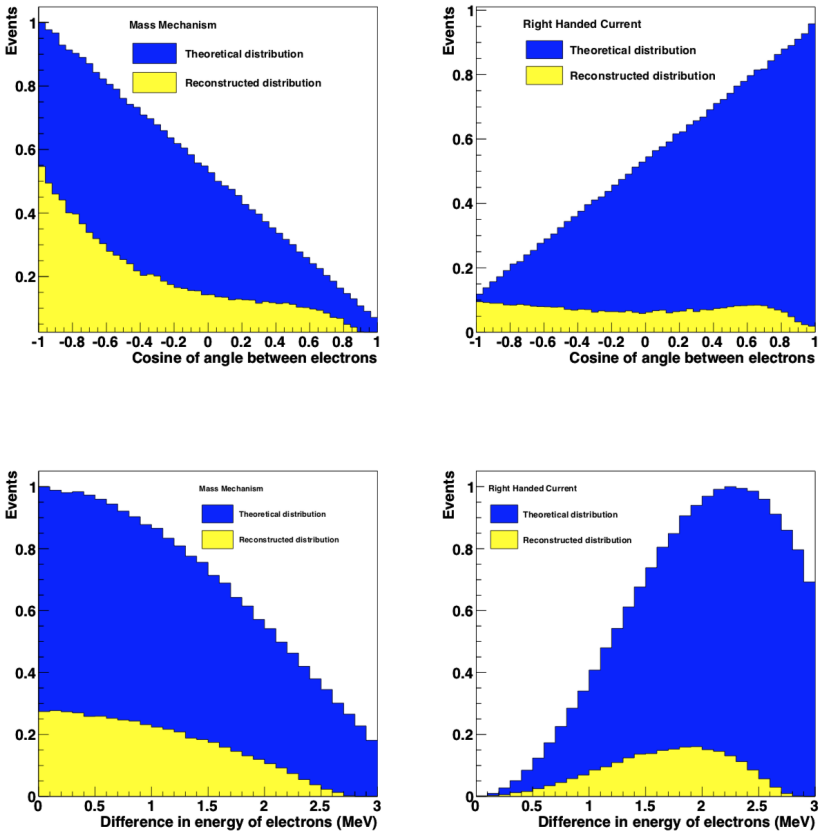

Figure 3.9: A comparison of the electron energy difference and angle between electrons for the right handed current and neutrino mass mechanisms. The yellow distribution indicates the expected response of the SuperNEMO experiment [50].

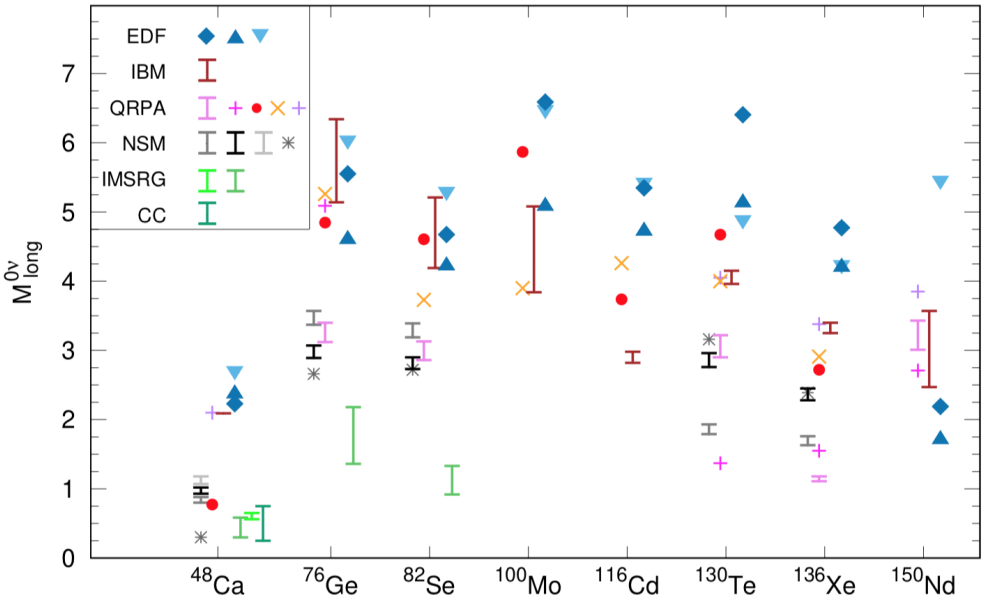

Figure 3.10: Nuclear matrix elements $M^{0\nu}$ for light-neutrino exchange from different many-body methods. The methods shown are the energy-density function (EDF), interacting boson model (IBM), quasiparticle random-phase approximation (QRPA), nuclear shell model (NSM), in-medium similarity renormalization group (IMSRG), and coupled-cluster (CC). The different coloured symbols for each model represent different collaboration's results. The results for the most commonly used isotopes for $0\nu\beta\beta$ searches are plotted. [40].

can be seen in Figure 3.11. Whilst there is a large spread in the nuclear matrix elements for different many body methods (Figure 3.10), this range does not have a significant impact on the spread of half-lives. Figure 3.11 motivates the use of a range of experimental isotopes in the search for $0\nu\beta\beta$-decay, in particular, $T_{1/2} \approx 10^{26}$ for ^{76}Ge, ^{130}Te, ^{100}Mo, ^{82}Se, and ^{136}Xe. In the next chapter, the experimental approach will be discussed. This includes detection principles, further motivation for different source isotopes and an overview of the current experiments using the isotopes listed above.

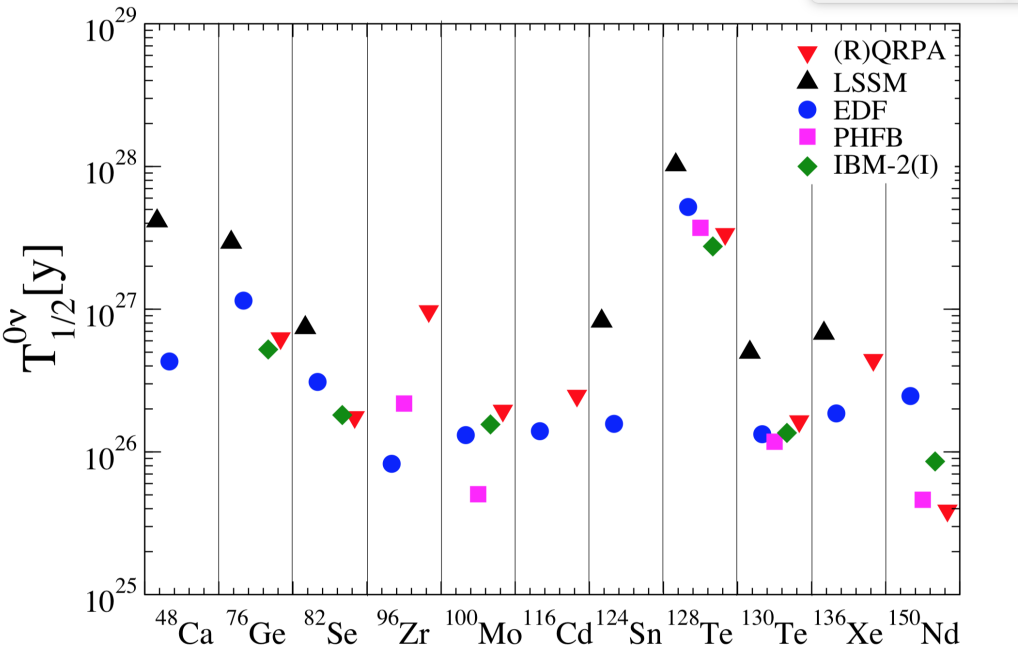

Figure 3.11: $0\nu\beta\beta$ half-lives for different experimental isotopes using various nuclear mass element approaches. Here the methods are QRPA, Large-Scale Shell Model (LSSM), EDF, Projected Hartree-Fock-Bogoliubov (PHFB) and IBM [51].

Chapter 4

Current Status of $\beta\beta$ Decay Experiments

"Let us choose for ourselves our path in life, and let us try to strew that path with flowers"

- Emilie du Chatelet

4.1 Detection Principles

The double beta decay experiments discussed in this chapter all search for a small $0\nu\beta\beta$ signal amongst a natural radioactive background, and a quasi-irreducible $2\nu\beta\beta$ background. In this section a formalism of the half-life in the presence of background is discussed. This is helpful in illustrating the key parameters for consideration when designing a $0\nu\beta\beta$ experiment. It should be noted that in Section 4.2, the discovery sensitivity is also mentioned. This refers to the half-life at which, 50% of the time a 3σ discovery could be made.

To explore key parameters for consideration, the half-life sensitivity, with a background present can be written as:

$$T^{0\nu}_{1/2}(n_\sigma) > \frac{4.16 \times 10^{26}\ \text{yr}}{n_\sigma} \left(\frac{\epsilon a M t}{m_i}\right) \sqrt{\frac{1}{N_B}} \tag{4.1}$$

[44], where N_B is the total number of background events after accounting for detector acceptance of background events

$$N_B = BMt\Delta E \tag{4.2}$$

In the equations above:

- $T^{0\nu}_{1/2}$ is the $0\nu\beta\beta$ half life lower limit in years;
- n_σ represents the number of standard deviations for a given Confidence Level (CL). As an example, a 90 % CL would be $n_\sigma = 1.64$;
- ϵ is the detection efficiency;
- a is the isotopic abundance of the chosen $0\nu\beta\beta$ source;
- m_i is the molecular weight of the source isotope;
- Mt represents the total exposure of the experiment, the mass of the source isotope $\times$ time (kg yr);
- B is the background index, the number of background events /kg keV yr;
- ΔE is the energy resolution of the detector.

From this equation it is clear that several different approaches can be taken to increase a detector's half life sensitivity. Successful experiments focus on having a large isotopic mass, an ultra low background, and an excellent energy resolution. Depending on the detector technology chosen, one or more of these may be optimised. Across all approaches, in the event that a $0\nu\beta\beta$ decay occurs, it is essential that the detection efficiency is high.

4.1.1 Isotope Selection

As shown in Equation (4.1), when selecting an isotope for a $0\nu\beta\beta$ search it is important to consider the isotopic abundance (a) as well as the mass (M) of the source available. Depending on the natural isotopic abundance the possibility of enrichment may also need to be explored. Table 4.1 show the most commonly used isotopes alongside their natural isotopic abundances and $Q_{\beta\beta}$ values. The

natural isotopic abundance is the relative amount of the isotope of the element that occurs in nature. Whilst there are 35 naturally occurring isotopes that can theoretically undergo this decay, only these 9 have a high enough $Q_{\beta\beta}$ value. The natural abundance of ^{130}Te makes it one of the few isotopes that does not require enrichment.

Isotope	Natural abundance (%)	$Q_{\beta\beta}$(MeV)
^{48}Ca	0.187	4.263
^{76}Ge	7.8	2.039
^{82}Se	8.7	2.998
^{96}Zr	2.8	3.348
^{100}Mo	9.8	3.035
^{116}Cd	7.5	2.813
^{130}Te	34.08	2.527
^{136}Xe	8.9	2.459
^{150}Nd	5.6	3.371

Table 4.1: Summary of commonly used $\beta\beta$ decaying isotopes, their natural abundances, and $Q_{\beta\beta}$ values [3].

Unfortunately, it cannot be a simple case of increasing the mass of the material in these experiments. With mass increase comes an increase in backgrounds and the need to be able to make this material ultra pure. In the Region of Interest (ROI), electrons from $2\nu\beta\beta$ decay are indistinguishable from $0\nu\beta\beta$ electrons. The following equation (4.3) can be used to approximate the signal to background ratio in the case where S is $0\nu\beta\beta$ and B is $2\nu\beta\beta$ [3]:

$$\frac{S}{B} \propto \left(\frac{Q_{\beta\beta}}{\Delta E}\right)^6 \frac{T_{1/2}^{2\nu}}{T_{1/2}^{0\nu}}. \tag{4.3}$$

To improve the ratio, isotopes with longer $T_{1/2}^{2\nu}$ can be chosen. If this is not possible then an excellent energy resolution should be prioritised to provide good separation between the peak of the $0\nu\beta\beta$ decay, and tail of $2\nu\beta\beta$ decay.

4.1.2 Low Background

As the sensitivity scales with $\sqrt{1/N_B}$ (see Equation (4.2)), a low background is also key to a successful experiment. Aside from the irreducible $2\nu\beta\beta$ decay discussed above, there are several other internal and external backgrounds to consider.

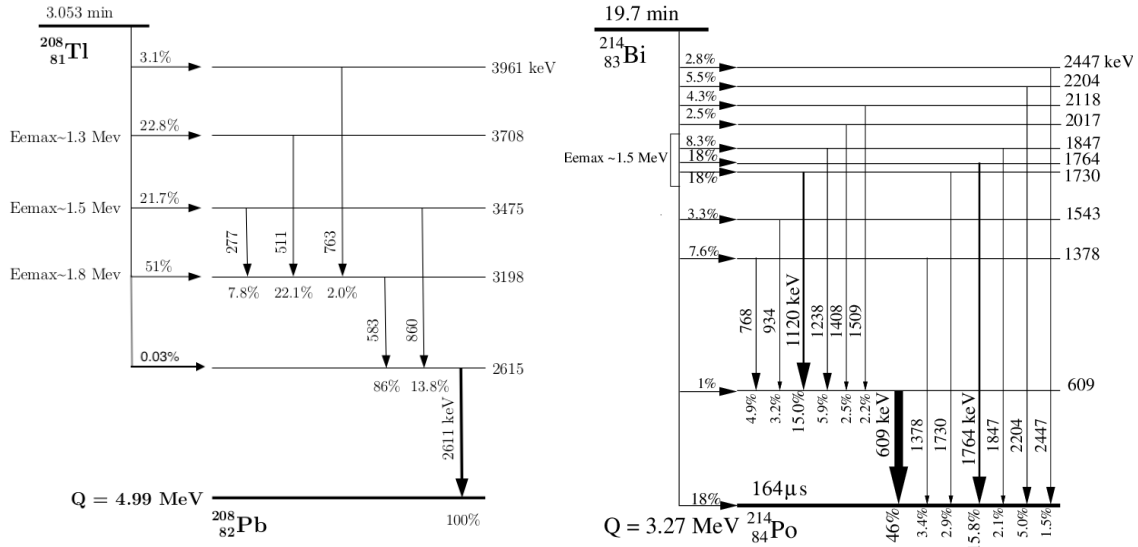

(a) ^{208}Tl decay scheme **(b)** ^{214}Bi decay scheme

Figure 4.1: The decay schemes of ^{208}Tl and ^{214}Bi. The most common decay paths are shown in bold [52].

Radon is a naturally occurring radioactive noble gas that is both odourless and colourless. It is emitted as part of the decay process for the uranium and thorium chains, and is unique in that all of its isotopes are also radioactive.

Two gaseous isotopes of radon that are of particular consequence to $0\nu\beta\beta$ backgrounds are ^{222}Rn and ^{220}Rn (also known as thoron). Once present within the detector it is a significant background to $0\nu\beta\beta$ searches due to the Q_β values of two of its daughter isotopes. ^{208}Tl ($Q_\beta = 4.99$ MeV) and ^{214}Bi ($Q_\beta = 3.27$ MeV) are β-decaying isotopes. They can be found in all materials in small amounts, and are a concern for the majority of $0\nu\beta\beta$ decay searches, as whilst their $Q_\beta > Q_{\beta\beta}$, they can populate events inside the ROI. Figure 4.1 show the most common decay routes for these two isotopes. It is possible to reduce their contribution by selecting a $0\nu\beta\beta$ isotope with a $Q_{\beta\beta} > 2.6$ MeV, as the highest energy γ is 2.615

MeV from ^{208}Tl. In addition to this, radiopure source isotopes and detector materials must be carefully selected to reach the low backgrounds required for $0\nu\beta\beta$ searches. Some experiments use shielding techniques to keep radon out. One example is the use of nitrogen blankets in SNO+ [53].

The background from cosmic muons can be easily suppressed by placing the detector underground. A large overburden of rock acts as a passive shield, whilst some experiments also include an active muon veto system. However, it is then necessary to shield the $0\nu\beta\beta$ detector from the natural radioactivity occurring in the surrounding rock. A combination of passive and active shielding is used to combat gamma radiation from decay chains, and neutrons, for example from the spontaneous fission of uranium. Further background reductions can be achieved by designing experiments that are capable of event reconstruction, and PID to better separate signal and background.

4.2 Overview of Approaches

Currently, there are two main approaches taken in double-beta decay experiments. Both NEMO-3 and SuperNEMO are heterogeneous, where the source and detecting volumes are separate from each other. The details of these experimental setups will be discussed in Chapter 5. The benefit of a heterogeneous detector is the ability to reconstruct event topologies for excellent PID, as well as background rejection. This configuration allows individual electron energies to be measured, as well as the angle between electrons. This can help distinguish the $0\nu\beta\beta$ mediating mechanism.

However, the majority of $0\nu\beta\beta$ experiments are homogeneous, where the source is the same as the detecting volume. Using this method, the source can be totally contained within the surrounding calorimeters, resulting in high detection efficiency. A high energy resolution can also be achieved with experimental setups such as those described below. The calorimeter and source isotope are combined, reducing the probability of the electrons or some of their energy escaping detection. Examples of homogeneous detectors include germanium semiconductors, cryogenic bolometers, liquid scintillators and liquid Xenon TPC. In the case of liquid scintillators, there can be a distinction made from homogeneous experiments,

as the source is added to detector volume. All of these will be discussed in the section below.

4.2.1 Germanium Semiconductor Detectors

In $0\nu\beta\beta$ searches, high purity germanium (HPGe) detectors are a popular choice. ^{76}Ge is an isotope capable of double-beta decay. The advantage of using HPGe is that it is intrinsically pure and has an excellent energy resolution. The enrichment process is also well established [54]. The germanium crystal acts as a semiconductor. When charged particles pass through they creates electron-hole pairs proportional to the energy of the traversing particle. The created pairs drift, under an applied electric field, to the readout electrodes where they produce a measurable pulse. To reduce electronic noise, HPGe detectors must be cooled to cryogenic temperatures.

GERDA

At the time of writing, the best limit from a ^{76}Ge detector comes from the GERDA experiment, set at $T^{0\nu}_{1/2} > 1.8 \times 10^{26}$ yr at 90% C.L, $\langle m_{\beta\beta} \rangle < (79 - 180)$ meV [55]. The GERDA experiment is located at Laboratori Nazionali del Gran Sasso (LNGS) in Italy. It used geranium detectors enriched to ≈ 87 % in ^{76}Ge. Liquid argon (LAr) was used both as a coolant and as an active shield from backgrounds. Traversing e/γ particles scintillate in LAr, with the resulting light detected by Photomultipler Tubes (PMTs) and Silicon Photomultipliers (SiPMs). This was then surrounded by a tank of pure water (Figure 4.2), again functioning as an active shield from muons and neutrons. Phase I of the experiment ran from November 2011 to September 2013 with an exposure of 23.5 kg yr. It achieved an average background of 11×10^{-3} counts/(keV kg yr) at $Q_{\beta\beta}$. Major improvements were undertaken for Phase II of the experiment with the goal of reducing the background further. This included installing additional germanium detectors with superior performance, as well as a liquid argon veto system. Phase II (starting in December 2015), with an exposure of 103.7 kg yr, achieved a background in the signal region of 5.2×10^{-4} counts/(keV kg yr). Over the lifetime of the experiment this corresponds to a background of < 0.3 counts in the signal region. Combining

the results from both phases sets the best limit on half life sensitivity, as quoted above [55].

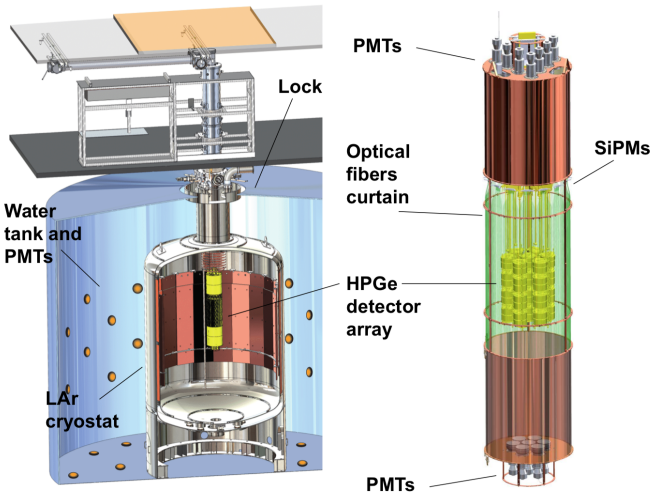

Figure 4.2: Schematic layout of GERDA setup [56].

MAJORANA DEMONSTRATOR

Another ongoing experiment using enriched ^{76}Ge (88%) is the MAJORANA DEMONSTRATOR at the Sanford Underground Research Facility (SURF) in Lead, South Dakota. It has a very similar approach to GERDA but encloses its copper vacuum cryostats in two copper shields, lead and a radon exclusion box. To achieve the low background necessary they have used ultra clean materials. Data acquisition began in July 2015, with the exposure being at 26.0 ± 0.5 kg yr (up to April 2018) [54]. Following on from this, the most recent results have increased the exposure to 64.5 kg yr and set a limit of $T^{0\nu}_{1/2} > 8.3 \times 10^{25}$ yr at 90% C.L. This corresponds to an effective Majorana neutrino mass ranging from 113-269 meV . The demonstrator also showcased an excellent energy resolution of 2.52 keV ($\approx 0.12\%$) FWHM at $Q_{\beta\beta}$ [57].

Large Enriched Germanium Experiment for Neutrinoless $\beta\beta$ Decay (LEGEND)

The LEGEND experiment is an exciting collaboration looking to combine existing resources and technical knowledge to reach a tonne-scale ^{76}Ge detector. It will utilise the background suppression of GERDA and the ultra low materials and energy resolution of the MAJORANA DEMONSTRATOR for a discovery potential of $T^{0\nu}_{1/2} > 10^{28}$ yr [3]. This search will be carried out in a phased approach towards the target tonne scale. The first phase, LEGEND-200 will develop existing GERDA infrastructure to include 200 kg of enriched Ge detectors. The goal for this first phase is to reach a sensitivity of 10^{27} yr within 5 years of running. This will require a background 3 times lower than for the GERDA experiment. At the time of writing LEGEND-200 anticipates commencing data taking in 2022. LEGEND-1000 aims to have 1000 kg of enriched Ge detectors running for 10 years, as a new facility. To reach the $T^{0\nu}_{1/2} > 10^{28}$ yr sensitivity and have background free conditions, it is estimated that the background must be $\approx$ six times lower than LEGEND-200 [58].

4.2.2 Cryogenic Bolometers

Bolometers were first proposed for the search of $0\nu\beta\beta$ decay in 1984 [59]. The general setup of a bolometer is to have an absorber, thermally coupled to a heat sink. Radiation incident on the absorber causes its temperature to increase. This is then read out by a temperature sensor. For $0\nu\beta\beta$ searches, a crystal grown from a $\beta\beta$ decaying isotope is used in the bolometer. When any particle is released in the decay, an increase in temperature is measured, proportional to the energy deposited in the crystal. The specific heat capacity of a crystal is proportional to $(T/\theta_D)^3$, where θ_D is the Debye temperature of said crystal [59]. As a consequence of this, to see a noticeable change in temperature from the energy deposited, the bolometer must be operated in a cryogenic environment. This is typically $\approx$ 10 mK. In general experiments based on this technology have an excellent energy resolution, good detection efficiency and the potential for low background if radiopure crystals are used.

Cryogenic Underground Observatory for Rare Events (CUORE)

CUORE is a ton-scale cryogenic bolometer experiment located at LNGS. It uses 988 cubic TeO_2 crystals, naturally abundant in ^{130}Te (34.167 $\pm$ 0.002 %). These are arranged in 19 towers and contained within a large cryostat, cooled to 10 mK [60]. The cryostat also acts as a thermal and gamma radiation shield. At this temperature an energy deposit of 1 MeV results in a temperature change of $\approx$ 0.1 mK [61]. Neutron-transmutation-doped (NTD) germanium thermistors are used to register this small change, as they are highly sensitive. CUORE has an excellent energy resolution of 7.8 $\pm$ 0.5 keV at $Q_{\beta\beta}$ (2527.518 $\pm$ 0.013 keV). A background of $(1.49 \pm 0.04) \times 10^{-2}$ counts /(keV) in the ROI has also been achieved. This can be improved and moved towards zero background by introducing PID into the detector setup. The CUORE detector found no evidence for $0\nu\beta\beta$ decay and therefore set a limit of $T^{0\nu}_{1/2} > 2.2 \times 10^{25}$ yr (90% CL), with a total 1038.4 kg yr exposure of TeO_2. This is equivalent to an effective Majorana mass upper limit of $90 - 305$ meV [60].

CUORE Upgrade with rapid Particle ID (CUPID)

CUPID is a next generation ton-scale experiment based on experiences from CUORE as well as techniques demonstrated by CUPID-0 and CUPID-Mo. CUPID-0 was the first medium scale demonstrator built, using 24 $Zn^{82}Se$ crystals 95% enriched in ^{82}Se. Selenium was chosen as it has a $Q_{0\nu\beta\beta}$ of (2997.9 $\pm$ 0.3 keV). In this energy region the β/γ background reduces significantly. The first phase of the experiment ran from June 2017 to December 2018 , with an exposure of 5.29 kg yr. It achieved an impressively low background for a bolometer based detector of $(3.5^{+1.0}_{-0.9}) \times 10^{-3}$ counts/(keV kg yr). A limit on the half life of ^{82}Se was set at $T^{0\nu}_{1/2} > 3.5 \times 10^{24}$ yr (90% CL), corresponding to a Majorana mass upper limit of $311 - 638$ meV [62]. After a six month long upgrade, the last phase was run from June 2019 to February 2020. Combined results from both phases have a total exposure of 8.82 kg yr and find an improved limit of $T^{0\nu}_{1/2} > 4.6 \times 10^{24}$ yr (90% CL). This results in a Majorana neutrino mass of $263 - 545$ meV [63].

An additional demonstrator CUPID-Mo was constructed at LSM to test the radiopurity and performance of large, enriched $Li_2{}^{100}MoO_4$ crystals. The ^{100}Mo came

from Neutrino Ettore Majorana Observatory (NEMO)-3 and was previously enriched to (96.5%). Due to it's natural abundance (9.7%), ^{100}Mo is a suitable isotope for large scale enrichment. The experiment features 20 enriched crystals stacked in 5 towers, with an exposure of 2.16 kg yr. During it's running time, no evidence of $0\nu\beta\beta$ was observed and a limit for the half life of ^{100}Mo was set at $T^{0\nu}_{1/2} > 1.5 \times 10^{24}$ yr (90% CL), $\langle m_{\beta\beta}\rangle < (300 - 500)$ meV. At the time of writing, this was the most stringent limit for ^{100}Mo, overtaking NEMO-3 by 30% with an exposure 30 times lower [64].

The set up of the CUORE experiment is such that only the sum total of electron energies are read out from the detector. As a result, its background discrimination capabilities are poor. In the energy region above 2.6 MeV CUORE was dominated by alpha particles from radioactive contamination of detector surfaces [64]. The CUPID collaboration aims to improve this by investigating the potential of active background rejection. Particle identification is possible by using a scintillating bolometer technique. Light emitted by incident α particles can be distinguished from that of γ and β particles. Once constructed, CUPID will contain an array of 1534 $Li_2{}^{100}MoO_4$ crystals. These will be grown from molybdenum enriched in ^{100}Mo $\geq$ 95 %, for a total active mass of $\approx$ 253 kg. CUPID will be situated at LNGS, utilising the existing cryogenic facility established for CUORE. The expected background of the CUPID baseline in the ^{100}Mo ROI is 10^{-4} counts/(keV kg yr). The physics goal is to reach a sensitivity of $T^{0\nu}_{1/2} > 10^{27}$ yr, equivalent to a Majorana mass ($\langle m_{\beta\beta}\rangle$) upper limit of $10 - 17$ meV [65].

4.2.3 Liquid Scintillators

Another approach in the search for $0\nu\beta\beta$ decay is to use liquid scintillators loaded with a suitable $\beta\beta$ decaying isotope. Large volumes of the scintillator are contained in a vessel and surrounded by PMTs. Particles emitted from the decaying isotope excite the scintillator, releasing light. This is captured by the PMTs and used to reconstruct particle energies. The energy resolution of these detectors is poor in comparison to bolometers and semiconductors. PID is also limited, however the ability to easily scale up the isotopic mass on these experiments means high sensitivities can be achieved. KamLAND-Zen and SNO+ both use this technique and are discussed below.

KamLAND-Zen

This experiment uses a liquid scintillator, loaded with ^{136}Xe (Xe-LS) in the existing, ultra low background, KamLAND detector. The ^{136}Xe is enriched to $\approx 91\%$. It is situated in the Kamioka mine in Japan at a depth of 1000 m (2700 meter water equivilant (m.w.e)) [66]. The Xe-LS is stored within a 25 µm thickness nylon inner balloon, that in turn is inside a 13 m diameter outer balloon (Figure 4.3). The outer balloon contains 1000 tons of liquid scintillator, and is surrounded by 1879 PMTs mounted in a 18 m diameter stainless steel spherical tank. This achieves a 34 % photocathode coverage.

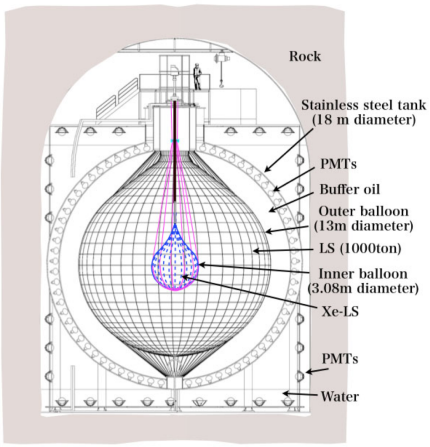

Figure 4.3: Schematic of KamLAND-Zen setup [67].

In large scale experiments such as this, background rejection and use of ultra pure detector materials is essential. Placing the experiment at a depth of 1000 m reduces the cosmic ray muon flux by a factor of 10^5 c.f ground level. The experiment also includes a 3200 ton water Cherenkov detector to shield radiation from the surrounding rock, and identify muons [67].

KamLAND-Zen 400 was the first stage of the experiment, that ran from 2011 to 2015, setting a limit of $T^{0\nu}_{1/2} > 1.07 \times 10^{26}$ yr (90% CL), $\langle m_{\beta\beta} \rangle < (61 - 165)$meV. Surface contaminants on the inner balloon restricted the sensitivity of KamLAND-Zen 400. As such, preparations for the next stage focussed on the manufacture of ultra clean nylon film. KamLAND-Zen 800 features a larger inner balloon with a mass of 745 kg of xenon. Data acquisition for KamLAND-Zen 800 began in 2019 with backgrounds reduced by a factor of 10. This large reduction was achieved in

part by purification of the liquid scintillator and xenon. Alongside this, cleaner manufacturing and improved purification of the inner balloon meant that previously detected ^{110m}Ag, believed to be contamination from Fukushima fallout, was significantly reduced. The following results were obtained from data collected between February 2019 and May 2021, combined with the results from KamLAND-Zen 400. A new world leading limit on the $0\nu\beta\beta$ half life was found of $T^{0\nu}_{1/2} > 2.3 \times 10^{26}$ yr (90% CL) with a total exposure of 970 kg yr . An upper limit of $\langle m_{\beta\beta} \rangle < (36 - 156)$meV was calculated. For the first time, this has tested the IH band using ^{136}Xe [39].

R&D has already begun for KamLAND2-Zen, with a planned start date of 2027 and xenon mass of over a tonne. If the energy resolution of the detector can be improved by a factor of two, then a half life sensitivity of $T^{0\nu}_{1/2} > 2 \times 10^{27}$ yr could be achieved in 5 years of running [3].

SNO+

The SNO+ experiment follows a similar concept to that of KamLAND-Zen. Once construction is complete, it will search for $0\nu\beta\beta$ in ^{130}Te. It is located at the SNO laboratory in Sudbury Canada, 2092 m (5890 m.w.e) underground. Figure 4.4 shows a depiction of the detector, suspended in a 30.5 m high cavern filled with ultrapure water. Natural radioactivity from the surrounding rock is shielded by this water. An acrylic vessel measuring 12 m in diameter will contain the 3.9 tonnes of natural tellurium loaded in 780 tonnes of liquid scintillator. Acrylic was chosen as it has a refractive index close to that of the liquid scintillator, as well as some ultraviolet transparency. Scintillation light will be measured by an array of 9300 PMTs on a geodesic support structure [53].

As of February 2022, SNO+ had completed its second phase. The acrylic vessel had been filled with 780 tonnes liquid scintillator, and SNO+ had begun taking data. This has primarily involved measuring purity of the liquid scintillator and external backgrounds. The next phase (scheduled for late 2022) will be with the loaded scintillator, to begin the $0\nu\beta\beta$ search. A half life sensitivity of $T^{0\nu}_{1/2} > 2.1 \times 10^{26}$ yr ($\langle m_{\beta\beta} \rangle < (37 - 89)$ meV) is expected after a 5 year run time [69]. Studies have shown that by increasing the tellurium concentrations from 0.5 % to 3 % by mass a sensitivity of $> 10^{27}$ could be accessible [70].

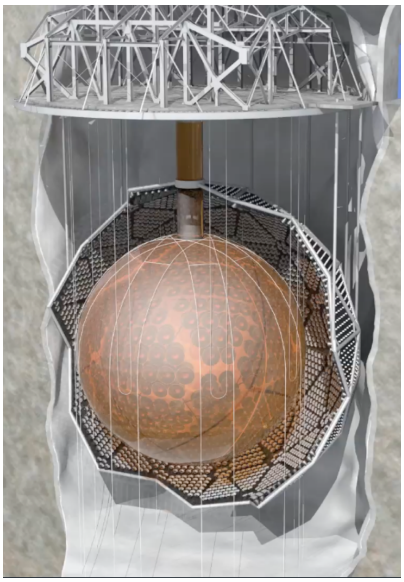

Figure 4.4: An artist's depiction of the SNO+ detector [68].

4.2.4 Xenon TPC

Time Projection Chambers allow for the measurement of β decay electron energies as well as the potential ability to track the electron's path through a detector (depending on the detector medium). This enhances background rejection capabilities, as it is possible to look for electrons from a common vertex. When a charged particle passes through it causes ionisation of the detector medium. These ionisation electrons are then drifted under the influence of an electric field to readout planes. The size and timing of the electrical signals provide information on the location and energy of the traversing particle. As the ionisation created in the chamber is proportional to the energy deposited, it is common for the density of the chosen detector medium to be such that all of the energy from β electrons is contained. Incorporating a scintillating medium improves both the timing and energy resolutions as the light emitted can also be detected. The density and scintillating properties of ^{136}Xe make it a good choice for $0\nu\beta\beta$ experiments.

EXO-200

EXO-200 is a cylindrical TPC filled with liquid xenon, enriched to 80.6 % in ^{136}Xe. As shown in Figure 4.5, a central cathode divides TPC into two drift regions.

Ionised electrons from interactions in the liquid xenon are drifted to the read-out anodes, passing through the X and Y grids. The scintillation light emitted is detected by an array of Avalanche Photodiodes (APDs), located behind the X-Y grids. This is all contained within a radio-pure copper vessel, which is then placed into a cryostat. Passive shielding is provided by the cooling and shielding fluid in the copper cryostat, as well as 25 cm of lead in all directions. The setup also includes an active muon veto system, allowing detection of > 94 % of cosmic ray muons.

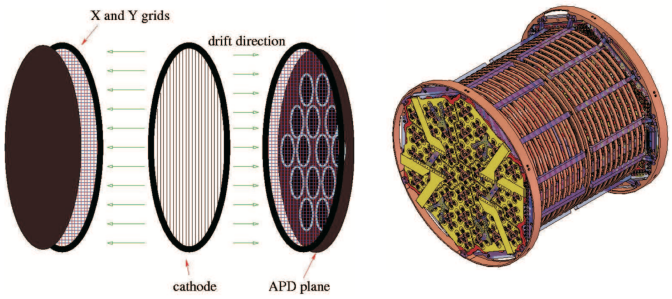

Figure 4.5: TPC diagram and 3D drawing of EXO-200 [71].

The experiment ran from 2011 to 2018 in two phases, at the Waste Isolation Pilot Plant near Carlsbad New Mexico. In the upgrade from Phase I to Phase II, the energy resolution was improved to $\sigma/E = 1.15 \pm 0.02$ % (≈ 2.7 % Full Width Half Maximum (FWHM) at $Q_{\beta\beta}$). Low background rates were achieved for Phase I and Phase II of $(1.7 \pm 0.2) \times 10^{-3}$ counts/(keV kg yr) and $(1.9 \pm 0.2) \times 10^{-3}$ counts/(keV kg yr) respectively [72]. Results from the complete dataset, with a total exposure of 234.1 kg yr, set a limit on the $0\nu\beta\beta$ half life of $T^{0\nu}_{1/2} > 3.5 \times 10^{25}$ yr (90 % CL). This corresponds to a limit on the Majorana neutrino mass of $\langle m_{\beta\beta} \rangle < (93 - 286)$ meV.

nEXO

Following on from the success of EXO-200, nEXO is a next generation liquid xenon TPC that is currently in the R&D phase. It will use five tonnes of liquid xenon, enriched to 90 %. The key difference in its design, from EXO-200, is that it uses a monolithic arrangement, with a single drift volume. This reduces the detector materials required, and takes advantage of the self shielding properties

of liquid xenon. The experiment is planned to be deployed in the SNOLAB cryopit to mitigate the background from cosmic muons. nEXO is predicted to reach a half life sensitivity of $T^{0\nu}_{1/2} \sim 10^{28}$ yr. Figure 4.6 illustrates an exclusion sensitivity of 1.35×10^{28} yr in 10 years of running, and a 3σ discovery potential of 0.74×10^{28} yr [1].

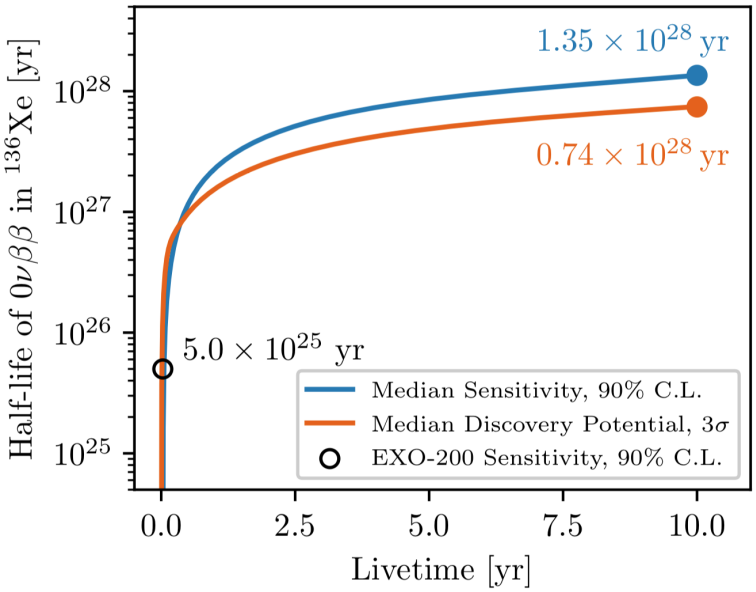

Figure 4.6: Median sensitivity (90% CL) against run time of the nEXO experiment [1].

NEXT

The NEXT collaboration focuses on using xenon gas at high pressure in a TPC configuration. It also utilises the electroluminescence (EL) property of xenon to amplify the ionisation signal , which is then measured by an array of PMTs to reconstruct the energy deposited in the gas. The 60 PMTs are located behind the TPC cathode. An array of $\approx$ 7168 SiPMs near the anode are used for tracking information. After the success of initial proof of principle experiments, the construction of NEXT-100 is under way at the Laboratorio Subterraneo de Canfranc (LSC), with a scheduled start of 2022. This will hold up to 100 kg of xenon gas at a pressure of 15 bar. Figure 4.7 shows the cross section of the detector, including the energy and tracking planes either side of the main detector volume. After an effective run time of three years, the expected half-life sensitivity is reported as 6×10^{25} yr, with a predicted background rate of $\leq 4 \times 10^{-4}$/keV kg yr [73].

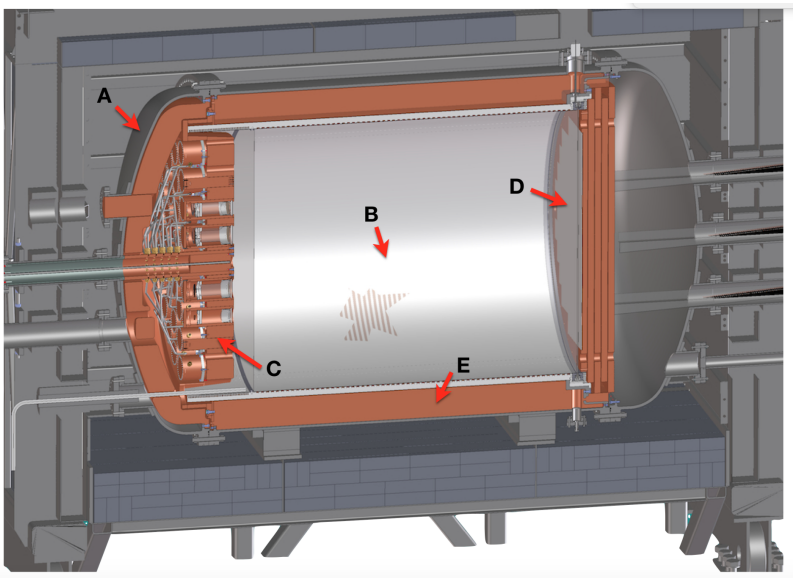

Figure 4.7: Cross section of the NEXT-100 detector. The outer layer consists of lead bricks, (A) is the stainless steel vessel, (B) the electric field cage, (C) the PMT sensor plane, (D) the SiPM sensor plane and (E) is the copper shielding [2]

A scale up of the above has already been planned for one tonne of ^{136}Xe (NEXT-1t). Improvements compared to NEXT-100 include the replacement of all PMTs with SiPMs to reduce backgrounds. The asymmetric TPC design would also be adapted to have a central cathode. Assuming that the detector is housed at LNGS, and is operated for ≤ 5 years, a sensitivity of 1.4×10^{27} yr (90% CL) could be reached [73].

Chapter 5

The SuperNEMO Experiment

"We have peered into a new world and have seen that it is more mysterious and more complex than we had imagined. Still more mysteries of the universe remain hidden. Their discovery awaits the adventurous scientists of the future. I like it this way."

- Vera Rubin

As introduced in the previous chapter, SuperNEMO is a heterogenous detector that uses a tracker-calorimeter technique. This enables three dimensional reconstruction of β-decay electron paths, as well as measurements of the electrons energy. SuperNEMO builds on the success of the NEMO-3 experiment, with improvements to source mass, energy resolution and backgrounds. NEMO-3 with briefly introduced here, discussing the most recent results and motivating the upgrade to SuperNEMO.

5.1 NEMO-3

The predecessor to SuperNEMO was situated at the LSM in the Frejus tunnel, at a depth of 4800 m.w.e. This rock overburden provides a passive shield to cosmic muons. The experiment began data acquisition in February 2003, and ran up until January 2011. The layout of NEMO-3 can be seen in Figure 5.1. The cylindrical detector comprises of 20 sectors, each featuring a double-beta decaying isotope in the form of a thin foil. These source foils were surrounded by a gaseous tracking detector, made up of 6180 drift cells orientated vertical to the source foils. 1940

optical modules (plastic scintillator blocks coupled to PMTs), were used to measure the energy and time of flight of particles. In order to distinguish electrons from positrons, a 25 G magnetic field was created using a solenoidal magnet. External shielding from γ and neutrons consisted of iron, borated water and wood with a total thickness of 19 m [52].

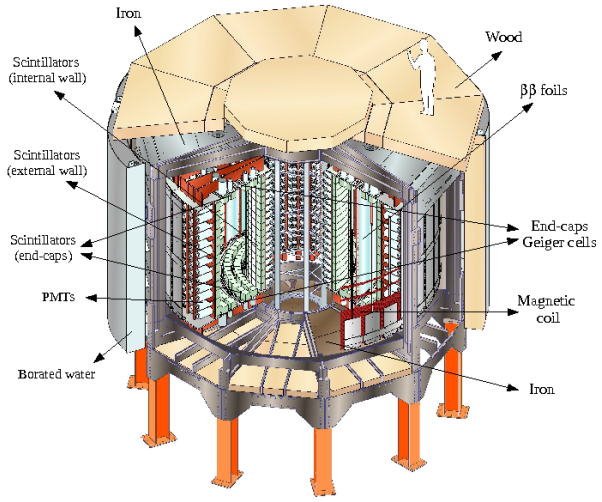

Figure 5.1: Schematic layout of NEMO-3 setup [52].

This approach has several benefits in the $0\nu\beta\beta$ search. Firstly, it allows for the full reconstruction of $\beta\beta$ events. In particular, it is possible to measure the single electron energies (Figure 5.2a). Using time of flight information and energy reconstruction, it is possible to identify if a particle is an electron, positron, gamma or delayed alpha. As a result, excellent background suppression can be achieved, and specific background channels can be studied. Secondly, this is the only detector technology that allows for the measurement the opening angle between electrons (Figure 5.2b). This is one of the key observables for determining the underlying mechanism behind the $0\nu\beta\beta$ decay.

NEMO-3 primarily searched for $0\nu\beta\beta$ in ^{100}Mo, but also obtained precise measurements of several $2\nu\beta\beta$ isotopes. By mass, the two largest isotopes were ^{100}Mo (6.914 kg) and ^{82}Se (0.932 kg). After a live time of 4.96 yr the $2\nu\beta\beta$ half life was measured as $T_{1/2} = (6.81 \pm 0.01) \times 10^{18} for ^{100}$Mo yr [74]. No $0\nu\beta\beta$ events were observed, therefore a limit of $T^{0\nu}_{1/2} > 1.1 \times 10^{24}$ yr (90% CL) was set for ^{100}Mo, with a total exposure of 34.3 kg yr. This is equivalent to an effective Majorana mass upper limit of $0.33 - 0.62$ eV [52].

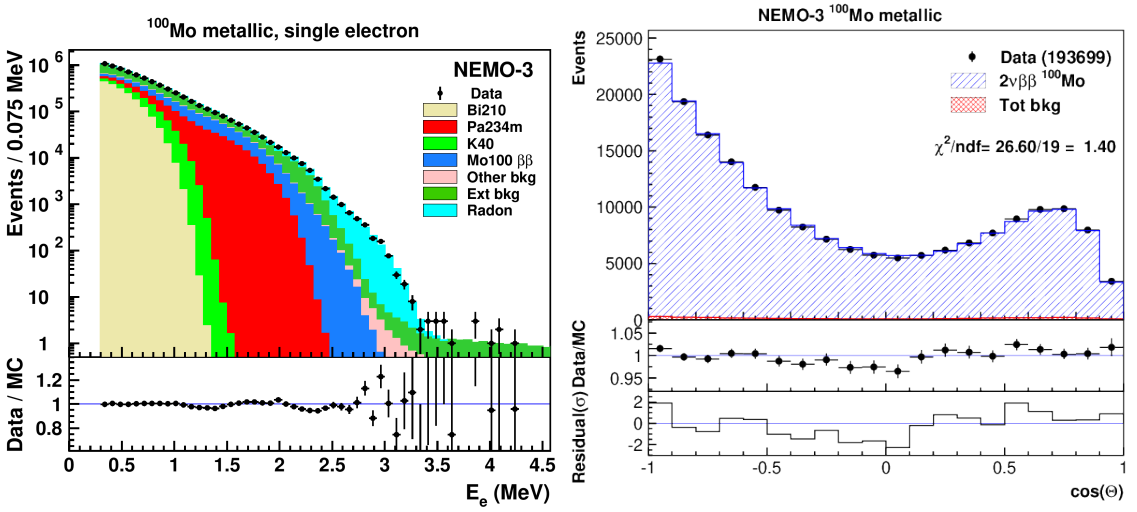

(a) Single electron energy for metallic ^{100}Mo **(b)** Opening angle ($\cos\theta$) between two electrons in ^{100}Mo

Figure 5.2: Distributions of the single electron energy for metallic molybdenum, and the opening angle between the two electron tracks [74].

Table 5.1 summarises the key differences between NEMO-3 and SuperNEMO. It shows the experimental values achieved and the target levels for SuperNEMO. Selenium was selected over molybdenum due to it's longer $2\nu\beta\beta$ half life of $T_{1/2} = (9.39 \pm 0.17\ (\text{stat}) \pm 0.58\ (\text{syst})) \times 10^{19}$ yr, and high $Q_{\beta\beta}$ value of 2997.9 ± 0.3 keV [75].

In order to probe neutrinoless $\beta\beta$-decay half lives of 10^{26} yr (Majorana mass of $\sim$ 50 meV) SuperNEMO will be scaled up to a source mass of 100 kg. As discussed in the previous chapter, this also requires improvements to the energy resolution as well as reduction of the number of background events. The limits on backgrounds, shown in Table 5.1, are lower than NEMO-3 by a factor of 30 for ^{214}Bi in the foils, 10 for ^{208}Tl in the foils, and 30 for ^{222}Rn in the tracker.

The SuperNEMO Demonstrator is the first module of this experiment, designed to be a proof of concept. It will provide insight into the calorimeter resolution, and background levels achievable. This in turn will test if the detector performance targets set for SuperNEMO are realistic. The demonstrator will hold 7 kg of ^{82}Se, and will run for 2.5 yr. A $0\nu\beta\beta$ half life sensitivity of $T_{1/2} > 6.5 \times 10^{24}$ yr is expected, corresponding to a $0.2 - 0.4$ eV (90% CL) effective Majorana mass [77].

Detector Property	NEMO-3	SuperNEMO
Isotope	^{100}Mo	^{82}Se
Source Mass	7 kg	100 kg
$0\nu\beta\beta$ Efficiency	18%	30%
Energy Resolution	8% @ 3 MeV	4% @ 3 MeV
^{214}Bi in foils	300 µBq/kg	10 µBq/kg
^{208}Tl in foils	20 µBq/kg	2 µBq/kg
^{222}Rn in tracker	5 mBq/m^3	0.15 mBq/m^3
$T^{0\nu}_{1/2}$ Sensitivity	10^{24} yr	10^{26} yr
$\langle m_{\beta\beta} \rangle$ Sensitivity	$0.3 - 0.7$ eV	$40 - 100$ meV

Table 5.1: Summary of the key experimental properties of the NEMO-3 experiment and the planned improvements for SuperNEMO [76].

The sections below are all in relation to the SuperNEMO Demonstrator, as is the work discussed in the remaining chapters.

5.2 SuperNEMO Detector Geometry

SuperNEMO features a planar geometry, moving away from the cylindrical layout used for NEMO-3. The primary reason for this is to allow for easy scale up from the 7 kg demonstrator to the full 100 kg detector. A modular design also means that as new modules are completed they can be added to the overall experiment. One limitation of this planar geometry is the difficulty in establishing a uniform magnetic field, compared with a cylindrical layout.

Figure 5.3a depicts the layers of the SuperNEMO demonstrator module, measuring 6 x 4 x 2 m (length x height x width). The overall SuperNEMO detector will feature 20 identical modules, each housing 5-7 kg of ^{82}Se. At the centre of each module is the source foil, sandwiched between two tracking chambers, followed by the calorimeter walls. Figure 5.3b shows the functionality of the detector in the different layers of the module. A $\beta\beta$ event occurring in the source foil, emits electrons that traverse the tracking chambers, filled with a mixture of of 95% helium, 4% ethanol and 1% argon. The energies and time of flight of each electron

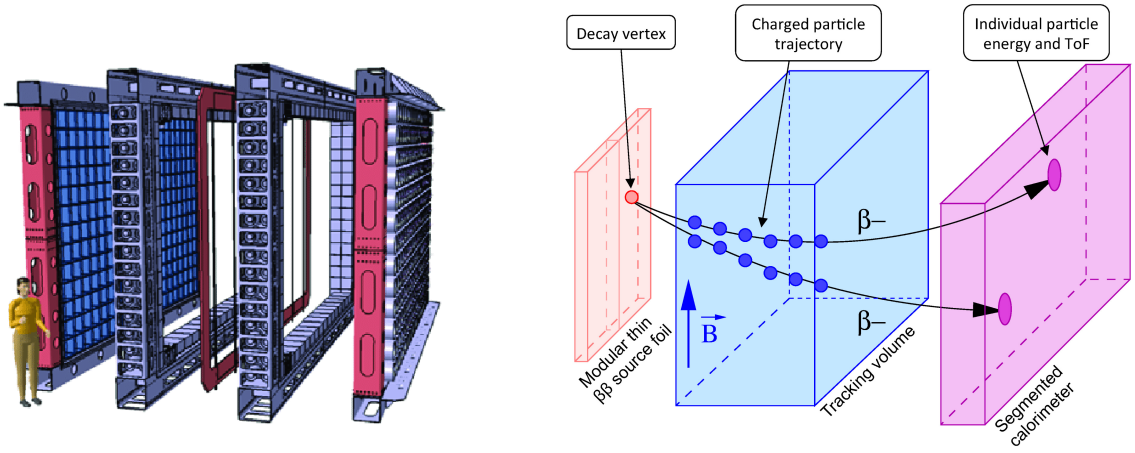

(a) Exploded view of the SuperNEMO demonstrator module

(b) Diagram of the detection principle

Figure 5.3: An exploded view of the SuperNEMO demonstrator, showing the layers of the modular design, and an illustration of the detection principles

are measured by the calorimeters either side. A 25 G magnetic field is established by wrapping a current carrying coil around the module. The detector will most likely be shielded from neutrons by surrounding ultra pure water, and from γ rays by iron. Each component of the detector is discussed in further detail below.

5.3 Source Foil

An advantage of the design of SuperNEMO is the ability to change the $\beta\beta$ source isotope at the centre of the module. It is also possible to study multiple isotopes simultaneously, as was the case for NEMO-3. Motivation for the initial choice of ^{82}Se is as discussed above. In addition to this, ^{82}Se has a reasonable natural abundance and has the potential to be enriched at scale using gas centrifugation. Another key consideration is radiopurity (with targets as shown in Table 5.1), as the source foils are in the centre of the detector.

Production of the majority of the source foils, with a final thickness of 40-60 mg/cm^2, involved the following steps. Firstly, ^{82}Se powder was purified. Several techniques were trailed including chemical precipitation, chromatography, and distillation. The powder was then mixed with Poly-vinyl-alcohol (PVA) and poured into moulds, before cutting into pads and inserting into Mylar protective

sleeves [78]. To ensure the stringent limits on backgrounds from ^{208}Tl and ^{214}Bi were met, the radiopurity of each component was measured using a detector that was purpose-built for SuperNEMO, BiPo-3 (see [79] for a detailed description).

5.4 Tracker

The SuperNEMO tracker for the demonstrator module is made up of two parts that sit either side of the central source foil (Figure 5.3a). Each section of the tracker comprises 113 columns of 9 tracker cells, giving a total of 2034 wire drift cells, all operating in Geiger mode. The configuration of a drift cell can be seen below in Figure 5.4a. Each cell is 2.7 m in length and has a 40 µm high voltage stainless steel anode wire at its centre. This central anode is surrounded by 12, 50 µm grounded field shaping wires, and capped at either end with a ring shaped copper cathode. The operating voltage for the tracker cells is ≈ 1800 V. The drift gas is a mixture of of 95% helium, 4% ethanol and 1% argon. Ethanol is used as a quencher, preventing continuous avalanche along the wire by absorbing photons. Argon has a lower ionisation energy than Helium and was found to enhance the propagation of avalanches [80].

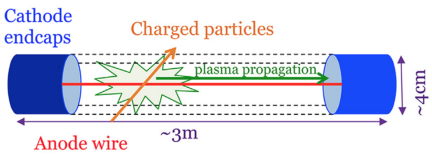

(a) Schematic of a single wire drift cell

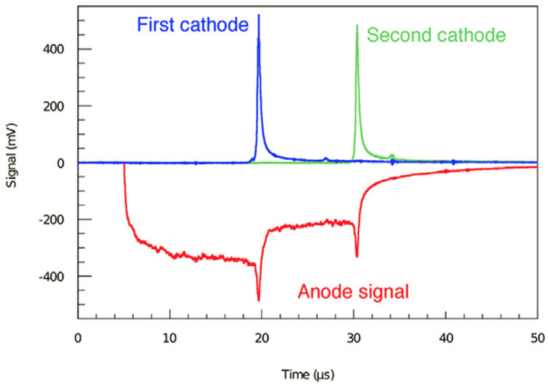

(b) Representation of electronical signal readout from drift cells

Figure 5.4: Diagram of the layout of a tracking cell and an example of the electrical readout when a charged particle traverses the cell.

When a charged particle traverses the tracking cell it ionises electrons in the drift gas, which then accelerate under the electric field towards the central anode. Ad-

ditional ionisation occurs closer to the anode leading to an avalanche and a gas of ionised plasma that propagates to the end caps. Figure 5.4b is an illustrative example of the signal that is read out. The first anode signal indicates the start of an avalanche, then two voltage drops are seen as the plasma reached each cathode. The respective positive cathode signals are shown in blue and green and coincide with the voltage drops in the anode. To calculate the longitudinal position of the traversing particle, the time is used between the initial anode signal and the readouts from either cathode. Radial distance from the anode can be found by combining information on the timing of the initial anode signal, with the faster readout from the calorimeters.

5.5 Calorimeter

The next layer of the demonstrator module are the calorimeter walls, which afford SuperNEMO the ability to measure the energy and Time Of Flight (TOF) of traversing particles. Full geometrical coverage is achieved by including additional calorimeters around the sides, top and bottom of the tracker sections. The main walls contain 520 OMs. Each main wall OM comprises of a polystyrene scintillator directly coupled to 8″ (R5912-MOD Hamamatsu) PMTs. At the top and bottom of the tracker sections are the 64 veto blocks. The sides of the tracking volume, known as the x-walls, have 128 OMs. Both the Veto and x-wall blocks used 5″ OMs recovered from the NEMO-3 experiment. These blocks can be seen in Figure 5.5 and include a light guide.

As shown in Table 5.1, the required energy resolution for SuperNEMO is 4% at 3 MeV (7% at 1 MeV). The improvement from the NEMO-3 resolution of 14-17% at 1 MeV was primarily achieved by direct coupling to the scintillator, optimised geometry of the block cut out, as well as improvements to the quantum efficiency of the PMTs. A dedicated study of the FWHM for the main wall OMs was conducted by the collaboration and found an energy resolution of 7.2 FWHM [81].

Figure 5.5: (left)8″ PMT directly coupled to polystyrene scintillator block and (right) a 5″ PMT coupled via a light guide

5.6 Magnetic Field and Shielding

As with the NEMO-3 experiment, there will be a 25 G magnetic field across the detector volume. This will be created by a copper coil that will wrap around the detector. The coil has been constructed using copper rods from NEMO-3 that have been reshaped to fit the geometry needed for SuperNEMO. The coil has 200 loops with a step between 3-7 mm attached to iron reinforcing plates [82]. An image of the installed copper coil can be seen in Figure 5.6.

Surrounding the magnetic coil will be an anti-radon tent (Figure 5.7), constructed from polycarbonate panels. Due to the location of the experiment, radon is present in the air, having been emitted from the surrounding rock. The tent prevents this air from entering the detector. The volume of air within the tent will also be flushed with radon free air to carry away any radon being emitted from internal components such as the PMTs. In order to provide the tent with radon free air, the experiment will utilise an anti-radon factory. This comprises of two columns filled with charcoal that trap the radon long enough for it to decay.

In addition to the 4800 m.w.e overburden that reduces the cosmic muon flux, passive shielding will most likely be provided by pure iron shielding and water shielding. The $\approx$ 20 cm pure iron will protect from external gammas. External neutrons in the environment can be captured by parts of the detector frame emitting up

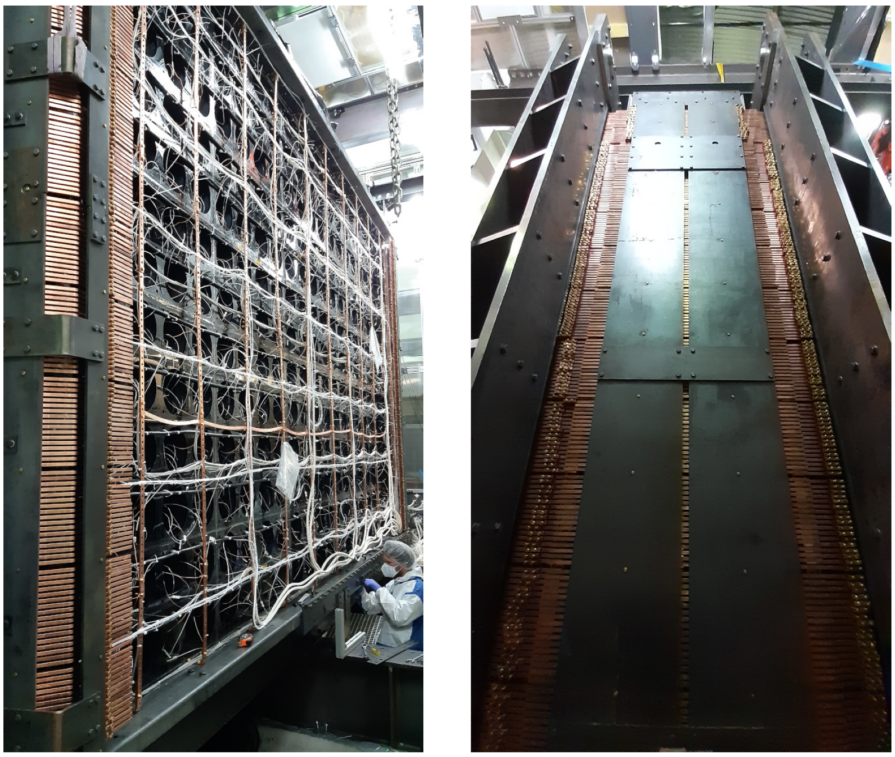

Figure 5.6: Image of the installation of the copper coil to provide a uniform magnetic field in the detector. (Left) The installed copper field wrapping around the calorimeter wall. (Right) The side on view of the detector where the source is central, surrounded by the tracker sections and finally the calorimeter walls [83].

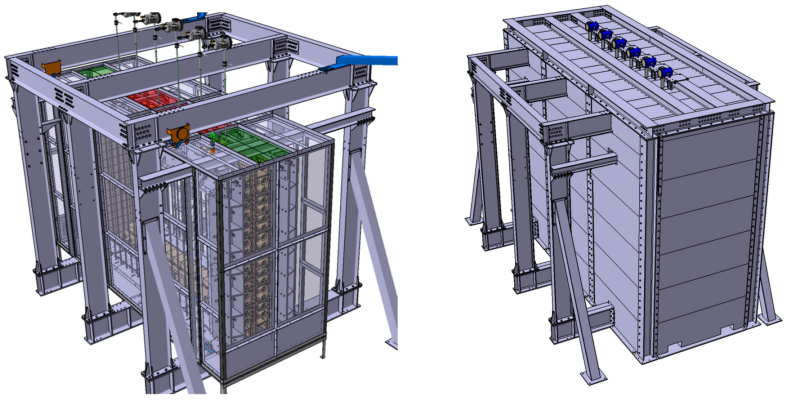

Figure 5.7: (left) Schematic of the SuperNEMO anti-radon tent (right) schematic of the iron shielding proposed as part of the passive shielding [84].

to 10 MeV gammas. These can then interact with the source foil and emit two electrons, mimicking the signal event topology. Water shielding provides a cost effective protection against these neutrons.

5.7 Current Status of the SuperNEMO Demonstrator

At the time of writing, the SuperNEMO Demonstrator source, tracking and calorimetry sections had been fully integrated within the clean tent at LSM. Gas tightness has been achieved with an overpressure of > 10 mbar measured (see §7.5.3 for more detail). In August 2021 the coil that will provide a uniform magnetic field was delivered to the LSM, with successful installation the following month (Figure 5.6). All of this was achieved within the context of the global pandemic that began in 2020. The next stages planned for 2022 are the integration of the anti-radon tent, iron shielding and water/polyethylene shielding. Commissioning and data taking will continue between each step to validate the effectiveness of the layers of shielding. In this section, commissioning of the calorimeter and tracker will be discussed, followed by updates on the next steps described above. Please note that in the following figures there are references to 'Italy', 'France', 'Tunnel' and 'Mountain'. As the experiment runs parallel to the road tunnel from France to Italy, we refer to the detector sides by which country they are closest to. The tunnel and mountain labels reference the sides closest to the road tunnel and mountain respectively.

5.7.1 Calorimeter Commissioning

Commissioning of SuperNEMO's 712 OMs began in earnest in 2020 with timing, resolution and energy calibration tests. A total of 26 runs were completed with ^{60}Co. This isotope was chosen as it β^- decays to ^{60}Ni, resulting in the simultaneous emission of two gammas of energy E_{γ_1} =1.72 MeV and E_{γ_2} =1.33 MeV. A reference OM was selected and the difference found between the time measurements of γ_1 at the reference OM and the other OM that γ_2 was detected at. This was measured several times for each OM in the main, x and Veto walls. This required

the use of three different reference OMs for full coverage. The mean from the Gaussian fit (μ) of the time differences measured, Δt, is indicative of the unique timing offset for each OM, caused, for example, by the signal cable length [85]. Figure 5.8 depicts the combined timing offsets, across all runs, for each calorimeter in the Italy main wall. The times are shown w.r.t OM 122 (M:0.9.5), and white cells represent dead OMs. The colour scale illustrates the offset values, where blue is earlier than the reference OM and yellow through to red indicates that the timing was later than the reference.

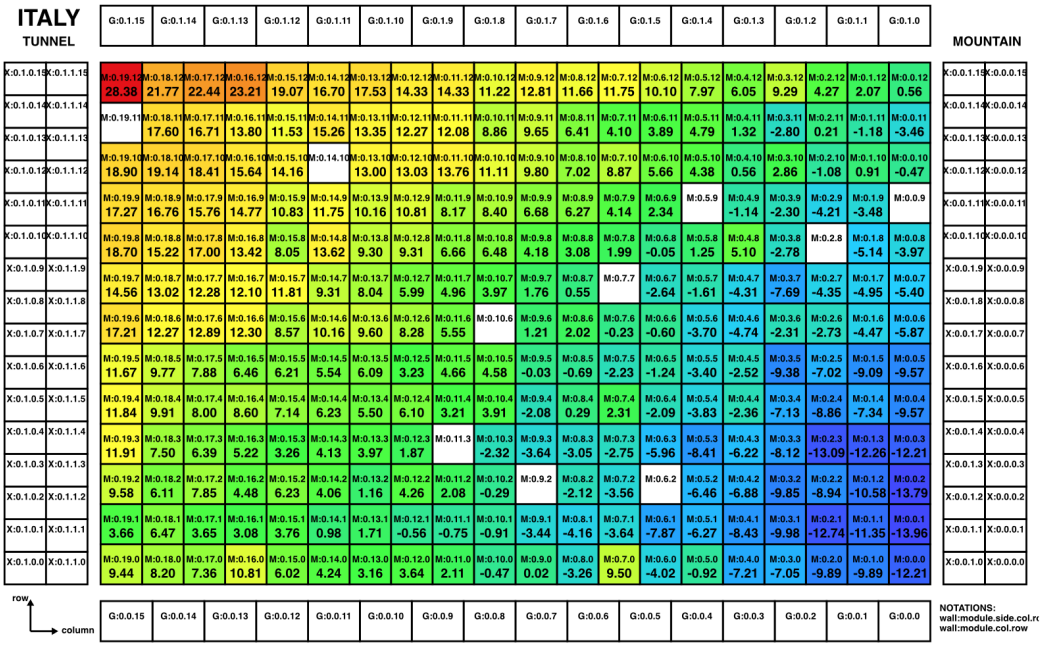

Figure 5.8: Map of the timing offsets measured for each of the calorimeters in the Italian main wall. The colour scale depicts whether the result was earlier or later than the reference calorimeter. Blue - earlier than reference. Orange/red - later than the reference [85].

By studying the colour gradient in Figure 5.8, it is evident that the offsets seen are a result of cable lengths. With the electronic board located closest to the bottom right corner, we have shorter cable lengths and therefore times that are earlier than the reference OM at the centre of the main wall. The resultant offsets were then used to correct for this effect.

Using a similar method, it was also possible to calculate the timing resolutions of each OM and build up a complete picture of the full walls. With the ^{60}Co source, the time resolution was found for gammas at 1 MeV. This was done by plotting

the Δt values as before, applying a Gaussian fit, and taking the sigma. The final results for the Italy main wall can be seen in Figure 5.9. The average timing resolution for this wall was found to be ≈ 0.6 ns. It should be noted that the OMs from NEMO-3 have been reused in the top and bottom row of the main wall. This illustrates the improvement in timing resolution achieved.

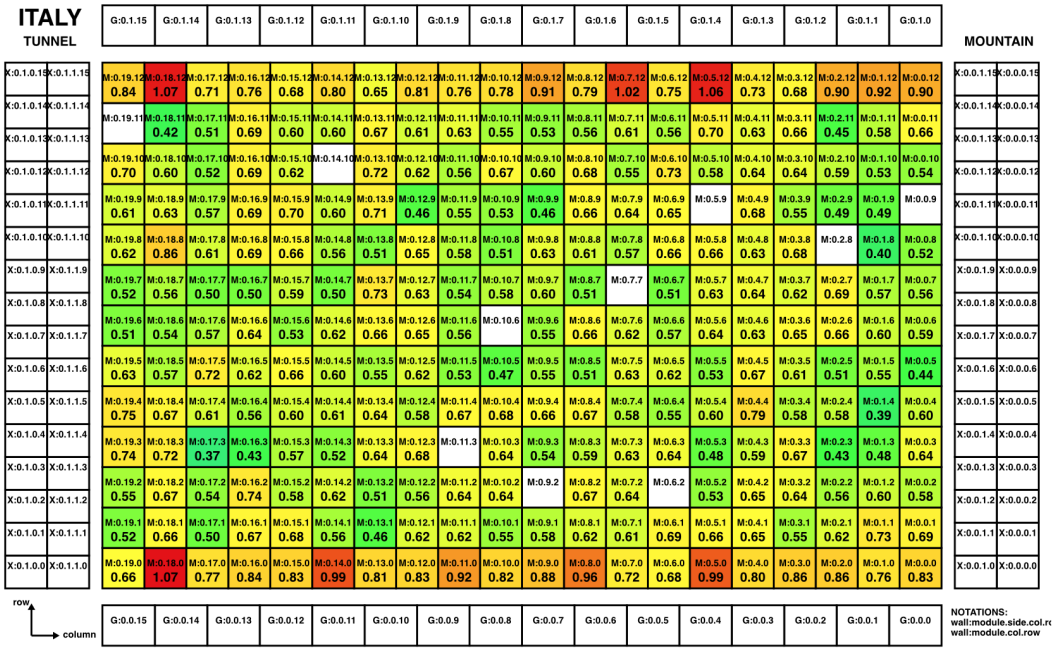

Figure 5.9: Map of the timing resolutions measured for each of the calorimeters in the Italian main wall. The higher the resolution value the closer to red on this colour scales. Dead OMs are shown as white cells [85].

Energy calibrations were also conducted as part of the commissioning process. The first stage of this was to use background radioactivity and find the charge spectrum from the integrated calorimeter wave forms. Figure 5.10 shows this spectrum with three simulated backgrounds fitted. 10^{10} ^{40}K, ^{214}Bi and ^{208}Tl events were simulated around the detector and shown as the blue, yellow and green lines respectively. From this plot it is possible to extract the gamma fluxes for each of the ambient backgrounds. For example, the average counting rate for ^{208}Tl above 2 MeV was found to be 1.73 ± 0.08 Hz compared with the simulated value of 2.1 ± 0.2 Hz [86]. The expected value comes from measurements of the external gamma-ray flux at the LSM. This study also allowed the calculation of calibration constants and equalisation of OMs using high voltage tuning.

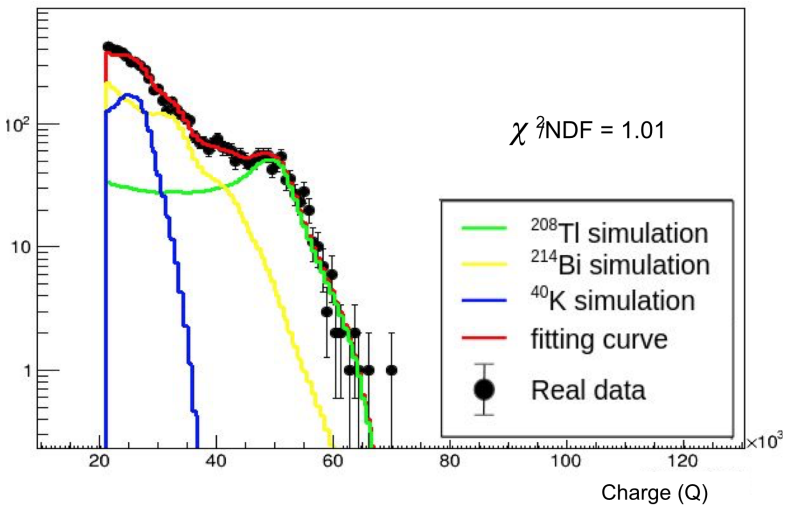

Figure 5.10: Charge spectrum from the integration of the calorimeter waveforms, fitted with ambient background sources, arbitrary units [87].

The next stage was to calibrate using 42 ^{207}Bi beta sources, deployed between the source foils. Figure 5.11 shows an example of one of the ^{207}Bi sources and how these are deployed in the detector.

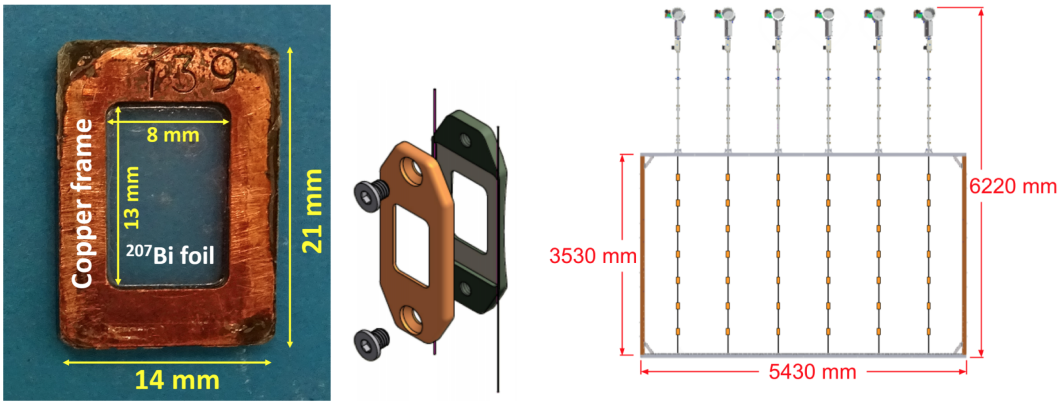

Figure 5.11: From left to right: a photo of one of the ^{207}Bi sources, a technical drawing of the envelope designed to hold the source in place and allow for deployment using the installed system, and a diagram source deployment system. An automatic system has been created above the demonstrator to raise/lower the sources. 7 sources contained in envelopes (orange boxes) are on each of the 6 columns. [88].

The use of ^{207}Bi is dual purpose, as the emitted electrons can be used for energy calibration, whilst the gammas can be used to measure the source activities. Two of the conversion electrons emitted from ^{207}Bi have energies of 482 keV and 976

keV. These electrons have unique energies compared to the continuous spectrum of β electrons. This means they are useful, even though their branching ratios are small. Decays from ^{207}Bi were plotted and then compared with the simulated detector response from OMs. The results can be seen in Figure 5.12, where the green line is the simulated spectrum and the points represent the point energies of the conversion electrons. The slight difference can be accounted for by the resolution of the OMs and energy loses in the foil and gas. The aforementioned decays can be seen as peaks in the spectrum.

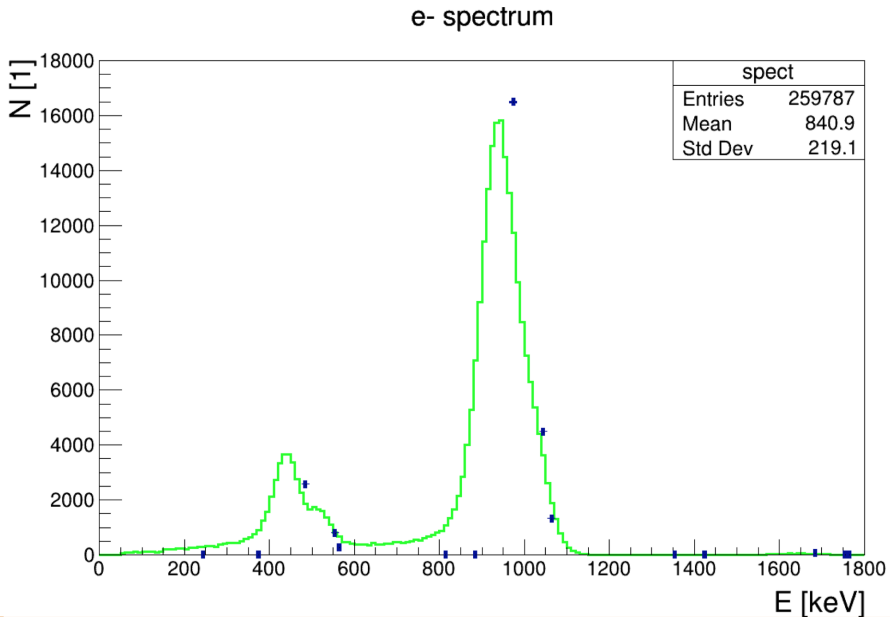

Figure 5.12: Expected electron energies, based on simulation (point markers), compared with simulated detector response energy spectrum from OMs (green line) [89].

In June 2022, the ^{207}Bi sources were successfully deployed between the source foils and detector commissioning began. An initial 7.5 hours of background data were recorded and compared with results from a 5 hour ^{207}Bi run. Figure 5.13 shows the charge spectrums from OM M:0.4.5 for both of these runs. The two main peaks in the ^{207}Bi run correspond to the 482 keV and 976 keV electron energies shown in Figure 5.12. Work is continuing on using results like these to conduct energy calibrations for the full detector.

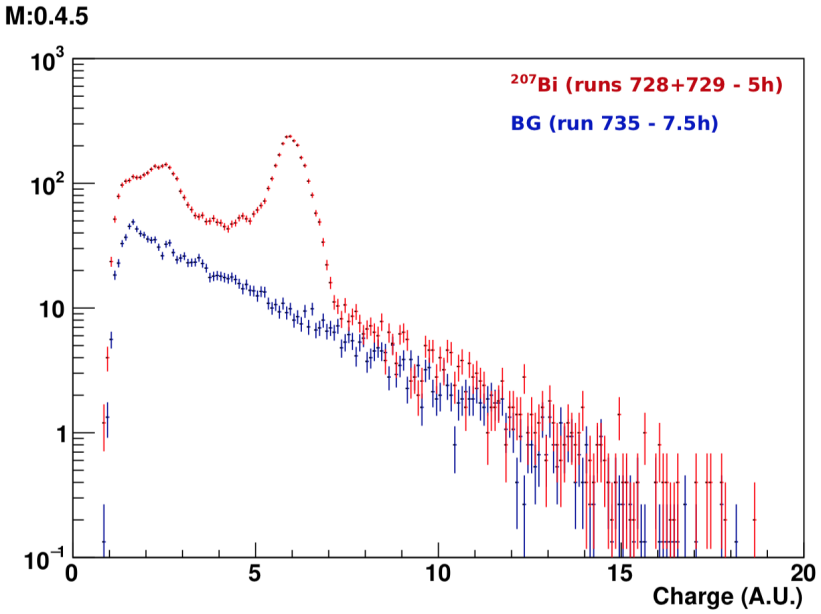

Figure 5.13: Charge spectra of OM M:0.4.5 with and without ^{207}Bi sources deployed. BG - background, ambient conditions [90].

5.7.2 Tracker Commissioning

Gas tightness was achieved in June 2021 (§7.5.3), and the first tracker High Voltage (HV) crate delivered, installed, and tested in August 2021. It was then possible to perform initial commissioning of the tracker. First light of the tracker and calorimeter was seen on the 15th of September, in Geiger mode, at a voltage of $\approx$ [1400-1700] V. One hour of data was taken, with a total of 9928 events [91]. Throughout the autumn of 2021 the commissioning campaign continued, with all areas of the tracker scanned. A total of $\approx$ 12 hours of data were recorded over 58 runs [92]. This section describes highlights of this campaign, followed by initial results from the deployment of ^{207}Bi sources.

The areas tested during the commissioning campaign, can be seen in Figure 5.14. First light was seen in Area 0, using HV crate 0. The signals were readout from the anode and cathodes, through the Data Acquisition (DAQ) software into Raw Trigger Data (RTD) file, and used to find the radial and position of charged particles §5.4. Combined with data from the calorimeter DAQ, this was used to reconstruct the first background events seen in the detector. An example of some of the events can be seen in Figure 5.15. It should be noted that the cells on the right

appear to be missing channels, but were in fact not powered up during the testing of Area 0.

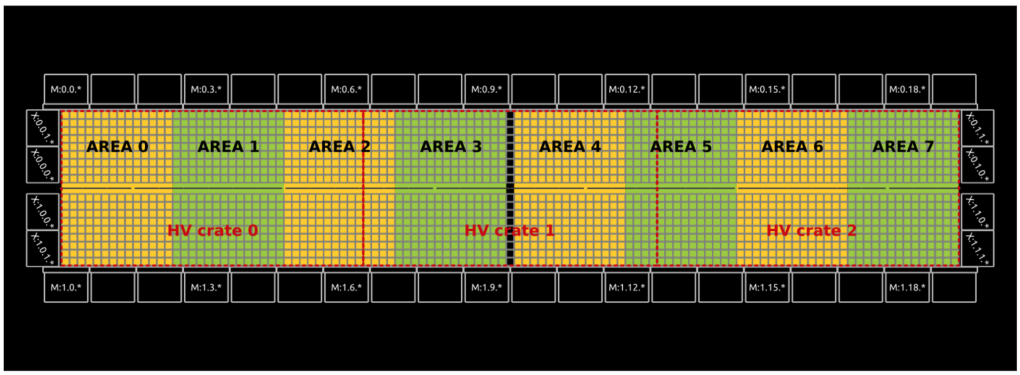

Figure 5.14: Top down diagram of the SuperNEMO tracker and calorimeter showing the assigned areas (yellow and green sections) and associated high voltage crates (red boxes) [93]

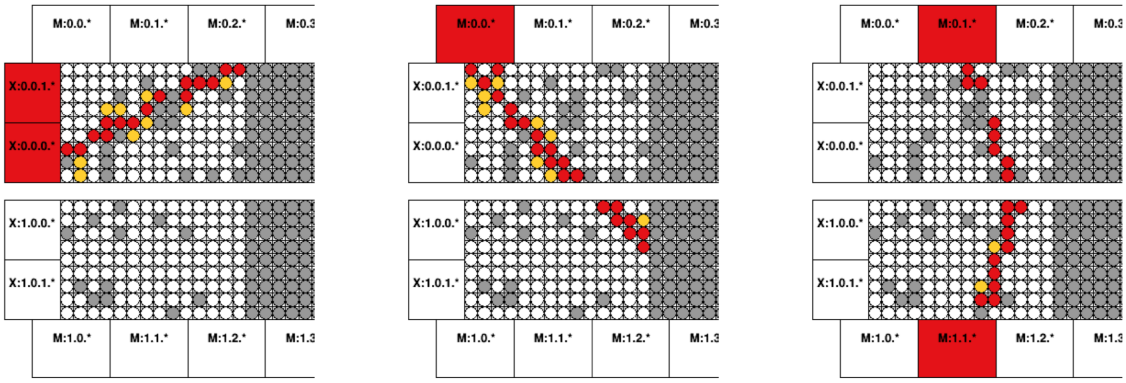

Figure 5.15: Reconstructed background events from the first light commissioning of Area 0 of the detector. Dark grey circles are missing channels, red circles are anode hits, yellow circles are cathode hits. Red boxes indicated calorimeters that were hit during this event [91]

Three further campaigns were conducted, Area 3 and 4 in October 2021, followed by all other areas in November. This provided the first validation of tracker operation at the LSM. Additional goals of this phase were to run the tracker/calorimeter triggers and DAQ in real conditions, as well as to commission the gas system (§7.5.3). Finally, it allowed for the full mapping of anode and cathode statuses.

With the deployment of ^{207}Bi in June 2022 it was possible to perform commissioning with sources present. At the time of writing this work was still underway,

however, some initial results are shown here. Figure 5.16 is a heat map showing the hit rate of cells in the area of the first two columns of ^{207}Bi sources. It can be seen that charged particle events are activating cells surrounding the sources, where red boxes indicate the highest density of hits.

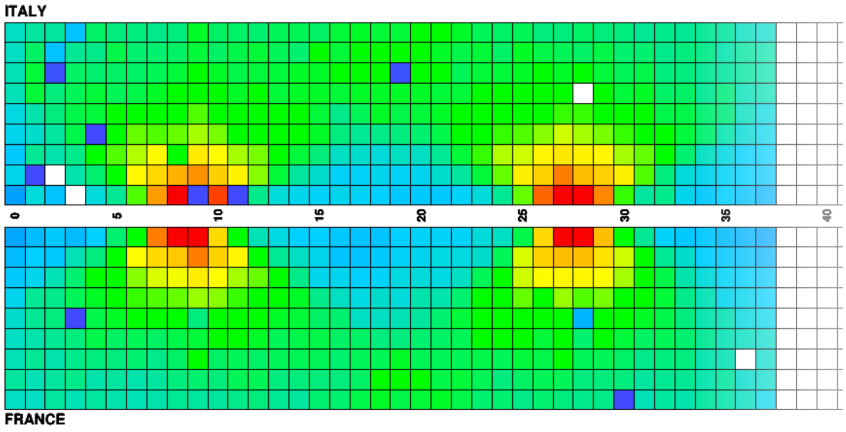

Figure 5.16: Heat map of tracker cell hits in the SuperNEMO detector with ^{207}Bi sources present, where red is a higher number of hits. White boxes show missing cells [94]

Figure 5.17 shows a heat map of the hit densities for the tracker cells when a selection is made on events triggering a particular calorimeter (not shown). Where the number of hits is increasing from blue through to red. The white boxes are missing cells. It is clear from Figure 5.17 that when you make this calorimeter selection you are seeing mainly ^{207}Bi events from the deployed sources. This is a good indication of signal purity in the calibration data.

5.7.3 Next Steps

Alongside the continued commissioning of both tracker and calorimeters using ^{207}Bi sources, several other key installations are planned for 2022. Cleaning and installation of the main stainless steel structure for the anti-radon tent has been completed. The next stage was to mount the High Density Polyethylene (HDPE) panels, which at the time of writing was also completed. Manufacturers for the construction of the iron shielding and supporting structure have been identified and the order placed. A design has been created for the water/polyethylene neutron shielding, along with a suggested process for assembly. The collaboration is

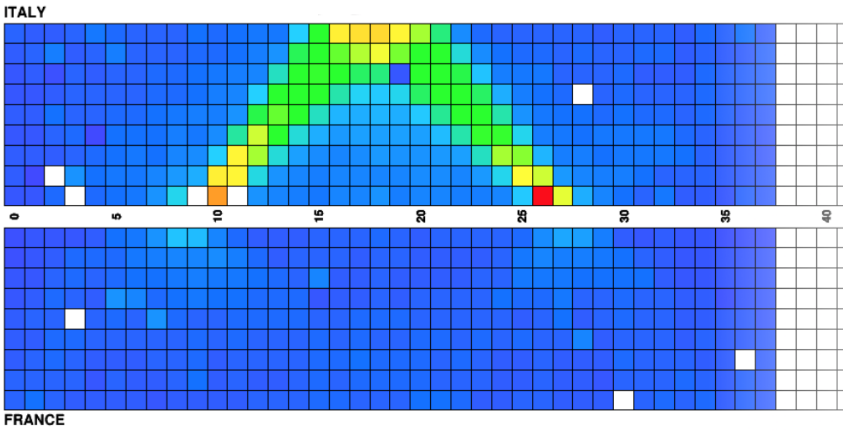

Figure 5.17: Heat map of tracker cell hits, with a selection of the event triggering a chosen OM, with ^{207}Bi sources present. Where red indicates a higher number of hits. White boxes show missing cells [94]

currently identifying a manufacturer for the blocks that will contain either water or a polyethylene solution. Finally, the remaining tracker HV crate is to be shipped to the LSM for installation and integration with the tracker. At the time of writing, two crates were already at the LSM, with the final delivery expected by the end of September 2022.

The SuperNEMO demonstrator is now entering a period of stable operation across the whole detector, without shielding present. The resultant data set will be valuable for the modelling of background contributions. Data taking will continue until installation of the iron shielding in late 2022.

Chapter 6

SuperNEMO Sensitivity to Backgrounds

"Science makes people reach selflessly for truth and objectivity; it teaches people to accept reality, with wonder and admiration, not to mention the deep awe and joy that the natural order of things brings to the true scientist."

- Lise Meitner

6.1 SuperNEMO Backgrounds

As discussed in §4.1, the half life sensitivity for $0\nu\beta\beta$ is inversely proportional to the number of background events. Therefore, successful operation of the detector relies on having an ultra low background. In this chapter I will begin by discussing the different types of background events present, before then describing the analytical techniques used to identify and measure them. This analysis will focus on sensitivity measurements for key internal backgrounds with variable activities and exposure times.

6.1.1 External Backgrounds

Any background event that originates outside of the detector source foils, and is not radon induced, is considered to be external. In general we want to con-

sider any activity that deposits energy close to the $Q_{\beta\beta}$ for $0\nu\beta\beta$. However, backgrounds that are of particular interest are those that can also mimic the two electron topology. As discussed in §5.6 external neutrons and gammas are present due to nuclear decay in the surrounding environment. Neutrons can also be produced via spallation from cosmic muons with energies in the 8 MeV $\rightarrow$ GeV scale. Whilst water shielding can protect against some of these, there is the potential for some to be captured on parts of the detector frame and release 8 MeV gammas. This is because the binding energy per nucleus, for all but the lightest elements, plateaus at around 8 MeV. There are three dominant processes by which the gamma can then interact with the source foil and mimic the signal topology (Figure 6.1).

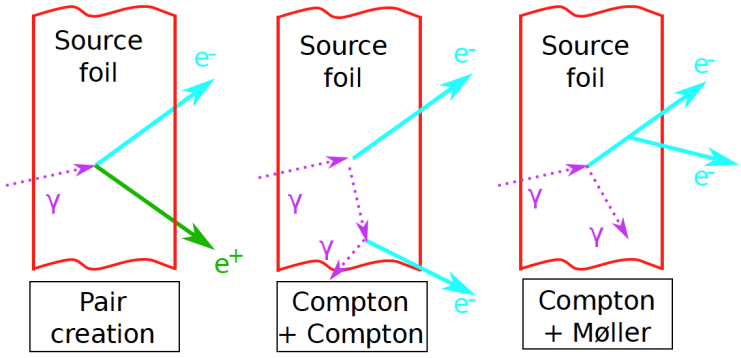

Figure 6.1: Recreation of the two electron event topology via three dominant mechanisms

In the case of pair production, if the positron's charge is poorly reconstructed it could be misidentified as an electron. However, the inclusion of a magnetic field as described in §5.6 mitigates this. If we fail to detect the original γ for the chains of Compton and Møller scattering events, then these can mimic the $0\nu\beta\beta$ topology.

6.1.2 Radon Background

Radon is a naturally occurring radioactive noble gas that is both odourless and colourless. It is emitted as part of the decay process for the uranium and thorium chains (Figure 6.2), and is unique in that all of its isotopes are also radioactive.

Two gaseous isotopes of radon that are of particular consequence to SuperNEMO backgrounds are ^{222}Rn and ^{220}Rn (also known as thoron). Thoron has a very short half-life of 55.6 s, thus very little emanates from the detector before decaying. Nonetheless, a small amount is still present within the detector and should therefore be measured. Whilst radon could be considered an external background, it can be present inside the detector through emanation of detector materials, diffusion through gaps in the seals, as well as contamination of detector surfaces or the drift gas. Once present within the detector it is a significant background to $0\nu\beta\beta$ searches due to the Q_β values of two of its daughter isotopes. ^{214}Bi and ^{208}Tl are beta decaying isotopes that have Q_β values of 3.27 MeV and 4.99 MeV respectively.

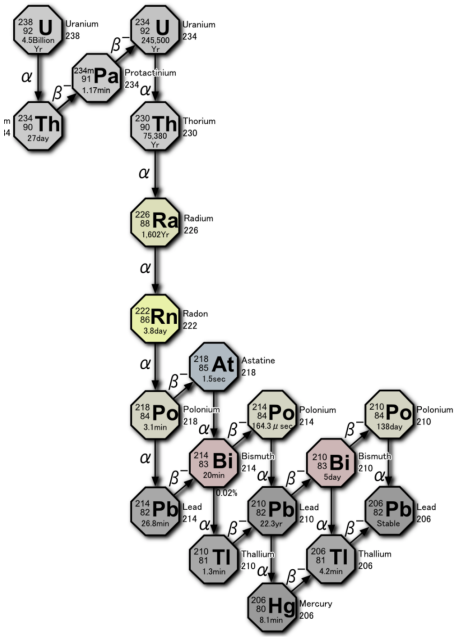

(a) ^{238}U decay chain, referred to as the radium series [95]

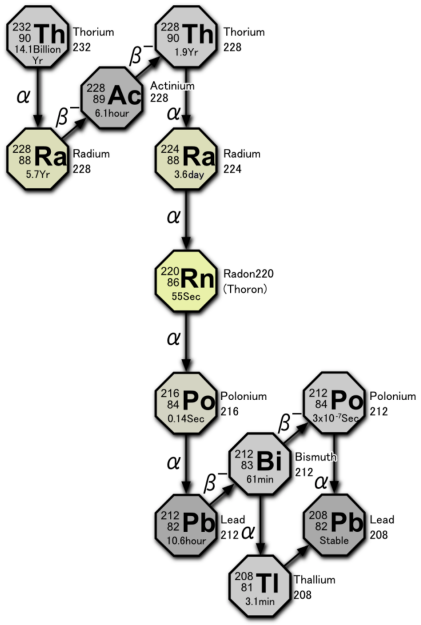

(b) ^{232}Th decay chain, referred to as the thorium series [96]

Figure 6.2: The two naturally occurring decay chains that emit ^{222}Rn and ^{220}Rn respectively.

Figure 4.1 shows schematics of the decay chains for both of these isotopes. In the case of ^{214}Bi (Figure 4.1b), 18% of decays are directly to the ground state ^{214}Po, emitting a 3.27 MeV electron. The remaining 82% beta decay to an excited state of polonium with the most common decay paths resulting in 0.61 MeV (46%), 1.76 MeV (15.8%) or 1.12 MeV (15%) photons emitted. For ^{208}Tl (Figure 4.1a)

there is always a β decay to an excited state with an emission of between 1 and 3 gammas that could then Compton scatter. Nearly every decay from the excited state involves a 2.61 MeV gamma. This is most often accompanied by 2 γ's of energy 0.51 MeV (22.1%) and 0.58 MeV (86%), or one γ of 0.86 MeV (13.8%).

The β and $\beta + \gamma$ decays described above can all result in two electron events that mimic the signal topology. This can occur via three main mechanisms (Figure 6.3) and are relevant when considering internal backgrounds. The Bremsstrahlung gammas are not always emitted or observed.

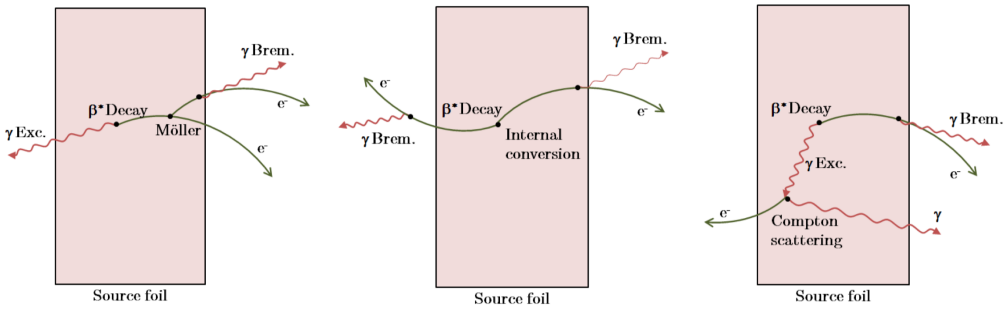

Figure 6.3: Mechanisms by which two electron events can be created from beta decay inside the foils. All begin with a beta decay to an excited state followed by - left to right: Møller scattering, internal conversion, and Compton scattering [75].

6.1.3 Internal Backgrounds

Internal backgrounds are classified as those that originate from within the source foils of the SuperNEMO detector. These backgrounds are predominately a result of contamination of the source foils. As demonstrated in Figure 6.3, the radioactive contaminants of greatest concern, are those that can undergo beta decay. In each case, two electrons are emitted, first by beta decay to an excited state followed by either Møller scattering, internal conversion or Compton scattering.

As previously discussed, the most dangerous isotopes are ^{214}Bi and ^{208}Tl with their decay energy $> Q_{\beta\beta}$ of ^{82}Se. These can both be present in the source foil as a result of the ^{238}U and ^{232}Th decay chains. Careful screening of the source and construction materials was conducted using HPGe and BiPo-3 detectors (as introduced in §5.3).

6.1.4 Background Activities

The target values for background activities can be seen in Table 5.1. For the demonstrator 6.2 kg source these are 62 µBq for ^{214}Bi in the foils, and 12.4 µBq for ^{208}Tl in the foils. Assuming an internal tracker volume of ≈ 15 m^3 gives a target value of 2.25 mBq for ^{222}Rn in the tracker.

When considering the effect of radon decay on internal detector components, the radon ions drift under the electric field towards the tracker field wires. ^{214}Bi ions present in the gap between the source foil and the first set of tracker wires are assumed to be deposited on the surface of the source foil. As a result of this, for the following analysis, the tracker activity is divided using the ratio of volumes between the tracker and the gap. This was calculated to be 92.2% for the tracker (field wires), and 7.8% for the gap (foil surface).

Several background scenarios were studied during this analysis. A summary of the activities used in each scenario is shown below in Table 6.1. For the ^{208}Tl foil bulk result, the most recent activity is from BiPo-3 [97].

Scenario	^{214}Bi Foil Bulk	^{214}Bi Foil Surface	^{214}Bi Tracker	^{208}Tl
1 (target)	62 µBq	0.1755 mBq	2.25 mBq	< 370 µBq
2	4.1 mBq	0.1778 mBq	2.28 mBq	< 370 µBq
3	1.8 mBq	0.1778 mBq	2.28 mBq	< 370 µBq

Table 6.1: Summary of the different scenarios used for the analysis of the sensitivity to internal backgrounds. These include the target activities, worst case upper limits and a central point from measurements using the BiPo-3 detector

Firstly, the target activities were used to calculate the expected run time to reach the required background sensitivity for ^{214}Bi and ^{208}Tl in the foils. Secondly, these activities were updated to reflect the most recent measurements and estimations from BiPo-3 and the Radon Concentration Line (RnCL) at the Mullard Space Science Laboratory (MSSL). The RnCL is a radon trapping system developed at University College London (UCL). Finally, a central value for the foil bulk was taken from BiPo-3 measurements of 290 µBq/kg, corresponding to a total of 1.8 mBq. These scenarios were chosen to assess the sensitivities to backgrounds for the ideal

(target) activities, the current worst-case activities from recent measurements, and finally, a middle ground that could still be achievable.

For the surface activity, the tracker activity was taken and divided by volume between the tracker wires and the foil surface, as described above. This resulted in an activity of 0.178 mBq (7.8% of 2.28 mBq).

The initial tracker activity for case 1 was calculated by taking the approximate total tracker volume of 15 m^3 and multiplying by the target activity of 0.15 mBq/m^3, giving 2.25 mBq. This was then updated for cases 2 and 3 to reflect the more accurate measurements of the tracker volume. Each C-section has a volume of 3.8 m^3, giving a total volume of 15.2 m^3 and activity of 2.28 mBq.

The activity in the tracker was measured for each quarter (C-section) by the RnCL. Without flushing an estimated total of 41.3 ± 4.7 mBq was calculated by finding the average of the first three C-section measurements of 11.37 ± 1.44 mBq, $15.26\ ^{+2.5}_{4.0}$ mBq, and 4.36 ± 1.31 mBq. This is a worst case measurement, assuming that the final C-section is not also of a lower activity as seen for the third section. Furthermore, it does not account for activity deposited on the source foil or for the flushing of the detector that will take place [98]. Table 6.2 shows the suppression factors and expected activities (a) in the SuperNEMO tracker with an anti-radon tent installed, for different input gas flow rates.

Input Flow (m^3/h)	Suppression Factor	a (with tent) (mBq/m^3)
0.5	5.35	0.51 ± 0.06
1.0	9.71	0.28 ± 0.03
2.0	18.42	0.15 ± 0.02

Table 6.2: Table showing the radon suppression factors and achievable activities (a) in the SuperNEMO tracker for different input flow rates [98]

6.1.5 Background Topologies

The tracker-calorimeter configuration of the SuperNEMO experiment allows for full reconstruction of individual particle trajectories and their energies. The ad-

vantage of this, is that it allows for the identification of event topologies, which in turn can be used to study backgrounds. Finding a clean channel to study the background is also advantageous.

Figure 6.2a illustrates the decay of ^{214}Bi to ^{210}Pb. Firstly, ^{214}Bi β-decays to ^{214}Po. This is followed quickly by an α-decay to ^{210}Pb, with a half life shown of 164.3 µs. The resulting emission of one electron, an alpha particle and $N \geq 0$ gammas is a clear channel for identification of ^{214}Bi backgrounds. The so-called 'golden channel' for measuring ^{214}Bi is the case where no gammas are emitted. It is named as such, as no other events contribute to this topology. The time between the ^{214}Bi and ^{214}Po decays is also used to make the selection of 'BiPo' events.

As discussed in §6.1.2, when ^{208}Tl β-decays it does so to an excited state of ^{208}Pb with the emission of between 1 and 3 gammas. Unfortunately, this is not a clean channel for measurement, as ^{214}Bi can β-decay with either 0, 1 or 2 gammas emitted. Whilst theoretically the 1e3γ topology is a clean channel, limitations of the SuperNEMO detector result in poor efficiency and low statistics. Gammas are unlikely to deposit all of their energy into a single calorimeter block. When this is taken into consideration, alongside the total energy being shared between three gammas, they are unlikely to meet the energy trigger threshold. Instead, the 1e1γ and 1e2γ channels can be used to measure ^{208}Tl backgrounds. The 1e2γ channel is preferred due to its higher transition energy and additional gamma emission. Other contributions to this channel include those from radon events, $2\nu\beta\beta$-decay and other radioactive contaminants present. In the following studies, the 1eNγ where $N > 0$ channels are used in order to increase statistics. However, in future, this could be tuned to focus on the 1e2γ channel.

6.2 Simulation and Reconstruction using SuperNEMO Analysis Software

It is essential to have the ability to accurately simulate the SuperNEMO detector as well as expected events. Doing so allows for the exploration of different experimental configurations, such as the magnetic field and different shielding options. It also allows for reconstruction techniques to be tested and optimised. With ad-

vanced simulations in place it is possible to study the reconstruction efficiency of the signal event and therefore to calculate the expected $0\nu\beta\beta$ sensitivity of the demonstrator module. The analysis below focusses on the sensitivity and relative errors of key internal backgrounds.

6.2.1 SuperNEMO Software

The SuperNEMO collaboration developed their own suite of software to simulate, reconstruct, visualise and analyse events in the SuperNEMO demonstrator module. This software system is called Falaise [99], and consists of three core applications/modules: FLSimulate, FLReconstruct and FLVisualize. Falaise stacks on the software development kit, Cadfael [100], which gathers key packages needed such as ROOT [101] and Geant-4 [102]. It also uses the functionality of a commonly used library in experimental nuclear and particle physics, Bayeux [103].

Falaise uses its three modules in a pipeline configuration, such that simulated events are created, passed through to be reconstructed, and finally result in analysed data. The event generator used for $\beta\beta$ and other common radioactive backgrounds is GENBB/DECAY0 [104]. This was developed for SuperNEMO collaboration by Vladimir Tretyak. In FLSimulate the generation and passage of particles through the detector is simulated. The output file contains the detector's response to the particles generated, see Figure 6.4. During the simulation, the full experimental setup is used, including the detector materials, geometry and other physical conditions. Several elements of this can be changed by the user as input variables. These include: activation of the magnetic field, inclusion of external shielding, source material and thickness, as well as specific vertex and event generators.

FLReconstruct takes the output detector response, performs reconstruction on each event and reads and writes this data to another output file. Once again, a pipeline architecture is used in FLReconstruct (see Figure 6.5), with a sequence of selected modules being run that can be customised by the user.

Two of the optional modules used in this analysis were the Gamma Clustering, and Alpha Finder modules. The Gamma Clustering Module, clusters adjacent calorimeter hits if they are close in time and are not associated with a charged

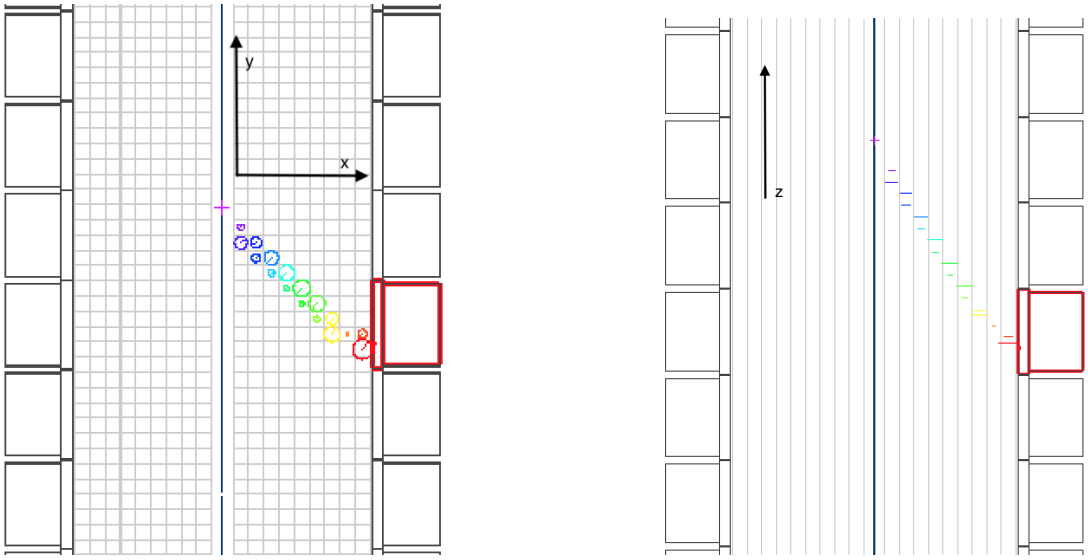

(a) Visualisation of a simulation of a 1e event in the SuperNEMO demonstrator, from the top view

(b) Visualisation of a simulation of a 1e event in the SuperNEMO demonstrator, from the side view

Figure 6.4: Visualisation of a simulation of a 1e event in the SuperNEMO demonstrator. The central source foil is shown in blue, the tracker cells as a light grey grid, the scintillator blocks are in grey. For ease of interpretation the Veto and x-wall blocks and calorimeters are not shown. Cells the electron has crossed are displayed as coloured circles. The colour of the circle depicts timing information. It's centre point is the location of the anode wire, and the radius is the minimum distance between the particle and the anode wire.

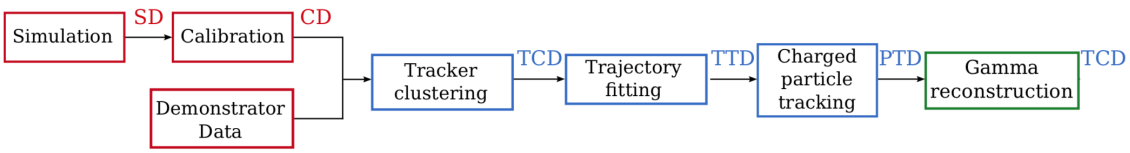

Figure 6.5: Summary of the Falaise simulation (red) and reconstruction (blue) pipeline. This shows where the Simulated Data (SD), Calibrated Data (CD), Tracker Clustering Data (TCD), Tracker Trajectory Data (TTD) and Particle Track Data (PTD) are created. The green modules were developed by S.Calvez during his Ph.D. [105]

particle. For hits on different calorimeter walls, it connects these into a single track for the gamma if the time of flight measurement is compatible with it being a single back scattered gamma. If the time of flight is compatible with hits from an electron, the gamma is connected to the electron vertex. An example of each case can be seen in Figure 6.6. The Alpha finder module will be discussed in more in §6.2.3. The coordinate system for SuperNEMO is as follows:

- x is defined as in the direction of the foil (x = 0) out to the calorimeter walls (x = ± 439.994 mm)
- The y direction is horizontal, parallel to the foil, with the calorimeter x-walls at y = ± 2505.494 mm
- The z direction is parallel to the tracker wires and can be seen in the side view,

where x and y directions are indicated in Figure 6.4a, and z in Figure 6.4b.

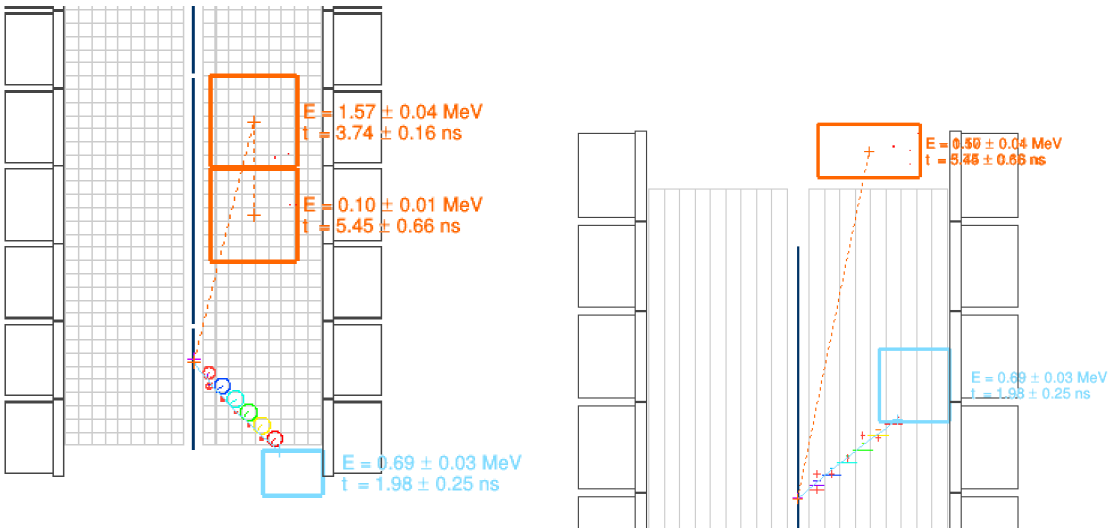

(a) Visualisation of a simulation of a 1e1γ event in the SuperNEMO demonstrator, from the top view

(b) Visualisation of a simulation of a 1e event in the SuperNEMO demonstrator, from the side view

Figure 6.6: Visualisation of a reconstructed of a 1e1γ event in the SuperNEMO demonstrator. The dashed orange line indicates the reconstructed gamma, with the orange block the optical module it was incident on. The light blue depicts the reconstructed electron track.

Electrons and positrons are identified in FLReconstruct by a curved track, associated to a calorimeter hit. The charge on these particles is inferred from the negative or positive curvature induced by the magnetic field.

6.2.2 Sensitivity Module

The Sensitivity Module [106], created by C.Patrick, is a Falaise pipeline module that processes data from the SD, CD, TCD, TTD and PTD banks. This module then outputs a ROOT ntuple file which can be used for further analysis. The tuple structure contains branches with standard cuts, basic counts, reconstructed particles, energies, tracks and vertices, topologies, multi-track topology information, alpha finding, calorimeter positions, and simulation information. Full descriptions of all of the branches can be found in README file at [106]. All of the branches contained in the alpha finding category were added by the author in the analysis work towards the Ph.D. During the course of the analysis described below, the author also added additional branches to simulation variables of the module.

6.2.3 Alpha Finder

Alpha Finder [107] is another optional Falaise pipeline module created by X.Garrido and T.Le Noblet. Unlike electrons, where the track is expected to reach the calorimeter and deposit energy, alphas have a high ionisation power and lose considerably more energy in their traversing of the detector. If we consider the tracker gas composition to be 100% He, the stopping power of an alpha particle is ≈ 0.25 MeV/ cm. For the alpha decay from ^{214}Po to ^{210}Pb, $Q_\alpha = 7.7$ MeV. This corresponds to a maximum alpha track length of 40 cm. As the distance from the source foil to the calorimeter walls is 45 cm we do not expect any alphas from the source to deposit energy in the calorimeter blocks. In addition to it's short track length, we expect a straight line trajectory. This is as a result of the alpha's high mass not being affected by the magnetic field, where the radius of curvature is proportional to the particle's mass. An illustration of this is shown in Figure 6.7. The standard trajectory fitting module does not fit tracks that have only 1-2 Geiger

hits. To ensure this information on delayed single (non-clustered) hits and delayed double (clustered) hits is not lost, the alpha finder algorithm was developed.

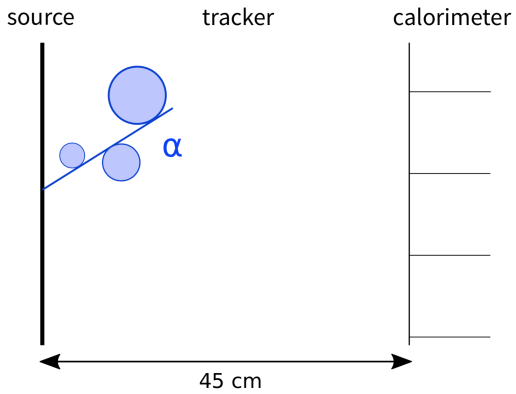

Figure 6.7: Visualisation of a typical alpha track originating in the source foil. Geiger hits are shown as the blue circles with the track fit shown as a straight line [47].

The algorithm used is based on one developed for the same purpose in NEMO-3. The first check is to confirm the presence of a prompt electron track alongside the delayed hits. During data taking in the SuperNEMO demonstrator, when a prompt track reaches the calorimeter it will trigger and open a window for 1 ms. Therefore, it is only in these instances that data will be taken for potential alpha candidates. Following on from this check, the X, Y and Z position and time of the delayed hits is stored if the below criteria are met [47].

1. The time of the delayed Geiger hit must be greater than a minimum threshold set by the user as the variable `minimum_delayed_time` . By default this is set to a value of 10 µs, the same as used in the initial tracker clustering. A threshold of 10 µs is chosen as this corresponds to the maximum drift time for a prompt tracker hit.

2. The distance between the prompt and delayed hits in xy is calculated and must be smaller than the user inputed `minimal_cluster_xy_search_distance`. Here the default is set to 40 cm, informed by the maximum expected track length.

3. Similarly to above, the distance between the prompt and delayed hits in z is calculated and compared with a threshold `minimal_cluster_z_search_distance`. The default is set at 30 cm.

4. The last distance to be checked is the distance between the prompt track vertex and the delayed hits. This must be smaller than the `minimal_vertex_distance`, set by default to 30 cm.

Assuming all of the above thresholds are met, the single and double delayed hits and their properties are stored in the alpha bank. Figure 6.8 shows how the alphas are successfully reconstructed irrespective of the number of delayed Geiger hits and the algorithm used. In this way, no information is lost for those alpha candidates which have fewer than three delayed hits (Figure 6.8a, Figure 6.8b).

As part of the analysis conducted by the author, several variables were added to the Sensitivity Module using information stored by Alpha Finder. The number of hits in a delayed cluster was stored in the variable `reco.delayed_cluster_hit_count`. This was used to inform the method for calculating alpha track lengths. Two lengths were calculated, track length `reco.alpha_track_length`, and projected track length, `reco.proj_track_length_alpha`. When an unclustered delayed hit is recorded, the alpha track length is taken as the distance from the hit to the nearest end of the prompt track. The projected track length is found by locating the projected foil vertex for the electron track, and calculating the distance between this and the delayed hit vertex. This can be seen in Figure 6.9, with the purple dotted line illustrating the projection of the prompt track back to the foil.

When two delayed geiger hits are found (Figure 6.10), these are clustered by the Alpha Finder and a track fitted. The length of the track is the distance from the centre of the furthest delayed hit to the nearest end point of the prompt track. For the projected length, again the prompt track is extrapolated back to the foil and the distance found from this vertex to the delayed hit with the largest magnitude x coordinate.

Finally, for more than two delayed hits (Figure 6.11), these are fitted with a line by the trajectory fitting module and the track length taken from the stored results. If the vertex is not already on the foil, it is extrapolated back and this distance stored as the projected track length.

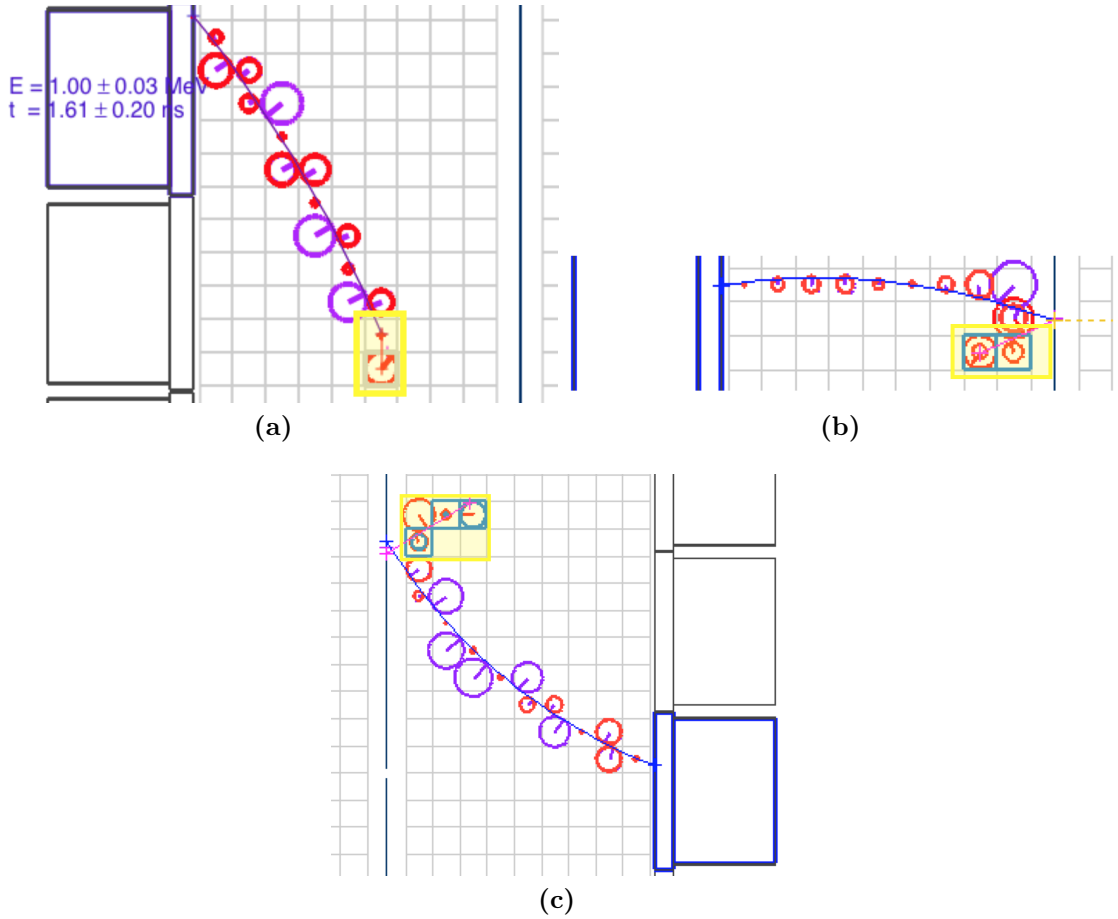

Figure 6.8: Visualisations of a 1e1α event with varying numbers of delayed Geiger hits. (a) Event with one delayed hit. The centre of the delayed hit cell is connected to whichever end of the prompt track is nearest. (b) Event with two delayed Geiger hits. In this case, the centre of the furthest delayed cell is connected back to the closest end of the prompt track. (c) Events with more than two hits are reconstructed by the tracker clustering algorithm. A line of best fit is found for the centre of each of the delayed cells. There is no input from the prompt track, and if the best fit line would intercept the foil, the alpha vertex is reconstructed there. The delayed hits identified as an alpha are highlighted by yellow boxes

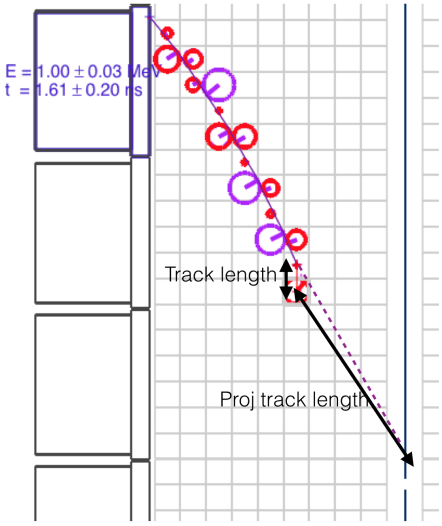

Figure 6.9: Illustration of the distances used to calculate the track length and projected track length for a single delayed hit.

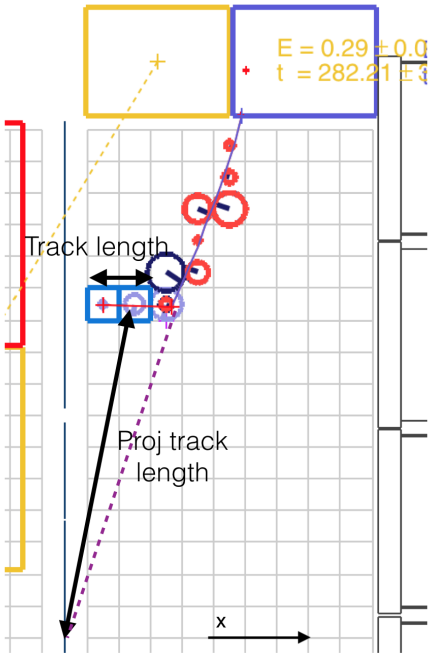

Figure 6.10: Illustration of the distances used to calculate the track length and projected track length for two delayed hits.

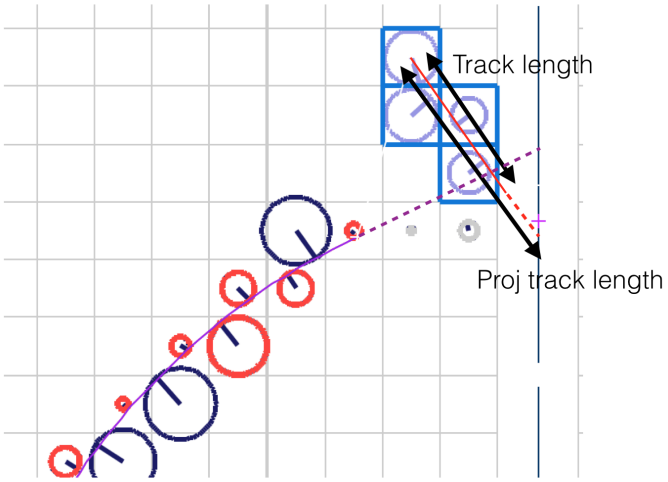

Figure 6.11: Illustration of the distances used to calculate the track length and projected track length for more than two delayed hits.

6.3 Internal Background Sensitivities

The following analysis was based on an initial investigation into the potential sensitivity of the SuperNEMO demonstrator to internal backgrounds, by S.Torre in 2012 [108]. Key changes in this work include use of the new SuperNEMO software suite for event simulation and reconstruction. The Sensitivity Module has been deployed to allow use of new cuts, such as vertex on the foil. The activities used have also been updated to reflect the most recent measurements, not known at the time of the previous study.

6.3.1 Event Generation

In order to study internal backgrounds in the SuperNEMO demonstrator module, the following events were simulated. These were ^{214}Bi in the bulk, on the foil surface, and on the tracker wires. ^{208}Tl events in the bulk of the foil were also generated. All of these simulations were conducted using the FLSimulate module discussed above, and the appropriate vertex generator. A total of 4×10^6 events were simulated, 1×10^6 of each background. Table 6.3 shows the vertex generator used for each sample and supplied in the simulation configuration file.

Sample	Vertex Generator
^{214}Bi Foil Bulk	`source_pads_internal_bulk`
^{214}Bi Foil Surface	`source_pads_internal_surface`
^{214}Bi Tracker Wires	`field_wire_surface`
^{208}Tl Foil Bulk	`source_pads_internal_bulk`

Table 6.3: Summary of the vertex generators used in the FLSimulate configuration file, for the simulation of the different background events.

Continuing with the Falaise pipeline, these events were then reconstructed with FLReconstruct. In the user defined configuration file, the Gamma Clustering module was enabled alongside the Alpha Finder module with delayed hit fitting. For Alpha Finder, the default thresholds were used for the delayed time and distances. Finally, the reconstructed events were passed to the Sensitivity module to create a ROOT file to use in the analysis described below. It is worth noting the following criteria used in the Sensitivity module to identify electrons, gammas and alphas.

An electron or positron is identified by a reconstructed track that has one or more associated calorimeter hits. The user can distinguish between an electron and positron by checking the charge. A gamma candidate is a single or clustered set of calorimeter hits that have not been associated to a track. An alpha candidate must meet the criteria for a delayed hit defined in the Alpha Finder, as well as having no associated calorimeter hit.

6.3.2 Background Efficiency

In Section 6.1.5 the ideal channels for measurement of ^{214}Bi and ^{208}Tl were discussed. These are 1e1α and $N_{gamma} \geq 0$, and 1eNγ where $N_{gamma} > 0$ respectively. Therefore, the first cut to be made on reconstructed events was a topology selection. Energy cuts were also made depending on the sample and number of electrons. For ^{214}Bi in the case of one electron, the electron energy threshold was set at 0.2 MeV. A lower energy was permitted if there was more than one electron, with a check on the higher energy electron being above the 0.2 MeV cut. This threshold was chosen based on the energy available to the electron in a β-decay.

The same logic was applied for ^{208}Tl, but with a higher threshold of 0.5 MeV owing to the higher Q value for this β-decay. Table 6.4, Table 6.5, and Table 6.6 show the efficiencies (ϵ) calculated (based on a 1×10^6 total number of events) for ^{214}Bi Foil Bulk, ^{214}Bi Tracker Wires, and ^{208}Tl Foil Bulk events respectively. The errors were calculated using binomial statistics. Please note these are not sequential cuts unless specifically stated.

Cut Selection	^{214}Bi Bulk ϵ	$\Delta\epsilon$
At least one electron	47.910 %	0.047 %
Only one electron	45.172 %	0.045 %
Only one electron and gammas	22.547 %	0.022 %
1eNγ, and electron energy $\geq$ 0.5 MeV	12.633 %	0.012 %
Only one electron and alphas	1.8690 %	0.0013 %
Only one electron and one alpha	1.8600 %	0.0013 %
1e1α and electron energy $\geq$ 0.2 MeV	1.7234 %	0.0011 %
1e1α, energy cut and vertex on foil	1.6830 %	0.0011 %

Table 6.4: Background efficiencies for topological and energy cuts on 1×10^6 ^{214}Bi Foil Bulk events. Here N $>$ 0.

Cut Selection	^{214}Bi Wire ϵ	$\Delta\epsilon$
At least one electron	43.095 %	0.043 %
Only one electron	39.819 %	0.039 %
Only one electron and gammas	8.3537 %	0.0078 %
1eNγ, and electron energy $\geq$ 0.5 MeV	4.6645 %	0.0041 %
Only one electron and alphas	18.602 %	0.018 %
Only one electron and one alpha	18.021 %	0.018 %
1e1α and electron energy $\geq$ 0.2 MeV	16.352 %	0.016 %
1e1α, energy cut and vertex on foil	7.9419 %	0.0074 %

Table 6.5: Background efficiencies for topological and energy cuts on 1×10^6 ^{214}Bi Tracker Wires events. Here N $>$ 0.

Cut Selection	^{208}Tl Bulk ϵ	$\Delta\epsilon$
At least one electron	49.008 %	0.049 %
Only one electron	45.548 %	0.045 %
Only one electron and gammas	34.522 %	0.034 %
1eNγ, and electron energy $\geq$ 0.5 MeV	21.051 %	0.021 %
Only one electron and alphas	0.06520 %	0.00025 %
Only one electron and one alpha	0.06520 %	0.00025 %
1e1α and electron energy $\geq$ 0.2 MeV	0.06050 %	0.00024 %
1e1α, energy cut and electron vertex on foil	0.05870 %	0.00024 %

Table 6.6: Background efficiencies for topological and energy cuts on 1×10^6 ^{208}Tl Foil Bulk events. Here N $>$ 0.

The tables include a selection cut on the vertex being on the foil. This is in order to distinguish between ^{214}Bi events coming from the foil bulk, versus the tracker wires. In addition to the cuts shown, a cut was applied on the total gamma energy. The final threshold selected was motivated by looking at the plots (Figure 6.12) of the total gamma energy for 1eNγ events in ^{214}Bi and ^{208}Tl.

Figure 6.12 used data from the first SuperNEMO Monte Carlo (MC) production, MCC1.0. In this production, five million events were generated for ^{214}Bi and ^{208}Tl in the bulk of the foil. These plots were included in the validation of the MCC1.0 results. For the 1eNγ channel in Figure 6.12a, the 1eNγ, and electron energy $\geq$ 0.5 MeV cut was used. For the 1eNα channel it was the 1e1α and electron energy $\geq$ 0.2 MeV cut (Table 6.4). Likewise, Figure 6.12b, used the 1eNγ, and electron energy $\geq$ 0.5 MeV cut in Table 6.6. When comparing the two energy distributions and cross checking with Figure 6.13 it can be seen that for ^{208}Tl the tail extends out to $\approx$ 4 MeV, whereas ^{214}Bi stops at $\approx$ 2.2 MeV.

Therefore, to remove the background of 1eNγ ^{214}Bi events from the ^{208}Tl measurement, a range of energy cuts from 2.2 MeV to 2.6 MeV were explored. It should be noted that in this case purity has been prioritised over efficiency. The efficiency results for varying total gamma energy cuts can be seen in Table 6.7. These are applied following on from the 1eNγ and 0.5 MeV energy cut.

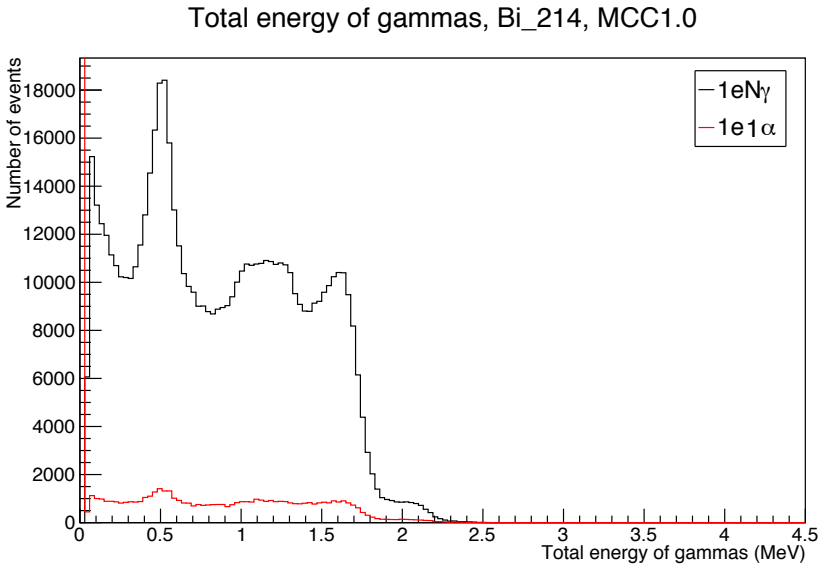

(a) Total gamma energy for ^{214}Bi events from the bulk of the foil. All of the cuts specified (except vertex on the foil) have been applied. The black line shows results for the 1eNγ topology, the red line is for the 1e1α topology, where N $>$ 0.

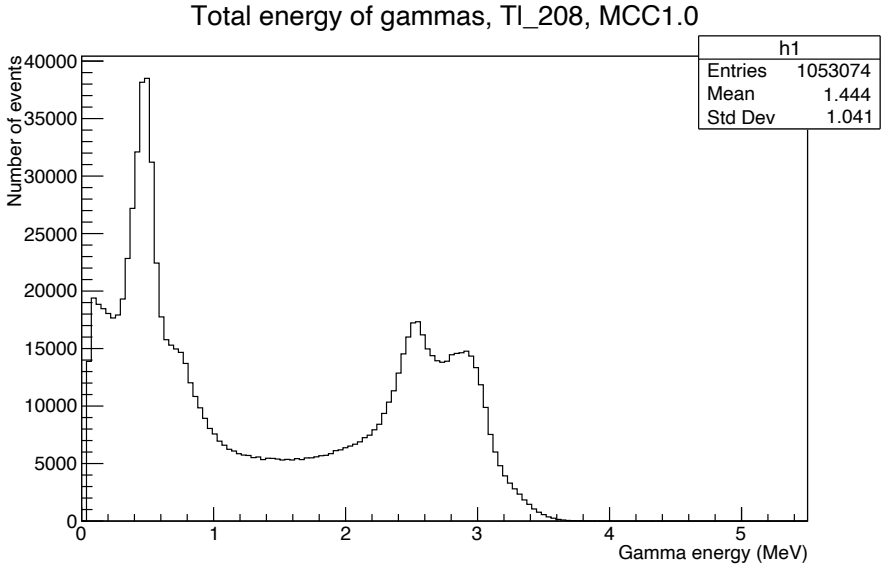

(b) Total gamma energy for ^{208}Tl events from the bulk of the foil. All of the cuts specified (except vertex on the foil) have been applied. The black line shows results for the 1eNγ topology, where N $>$ 0.

Figure 6.12: Total gamma energy spectrum for ^{214}Bi (a) and ^{208}Tl (b) events in the bulk of the foil.

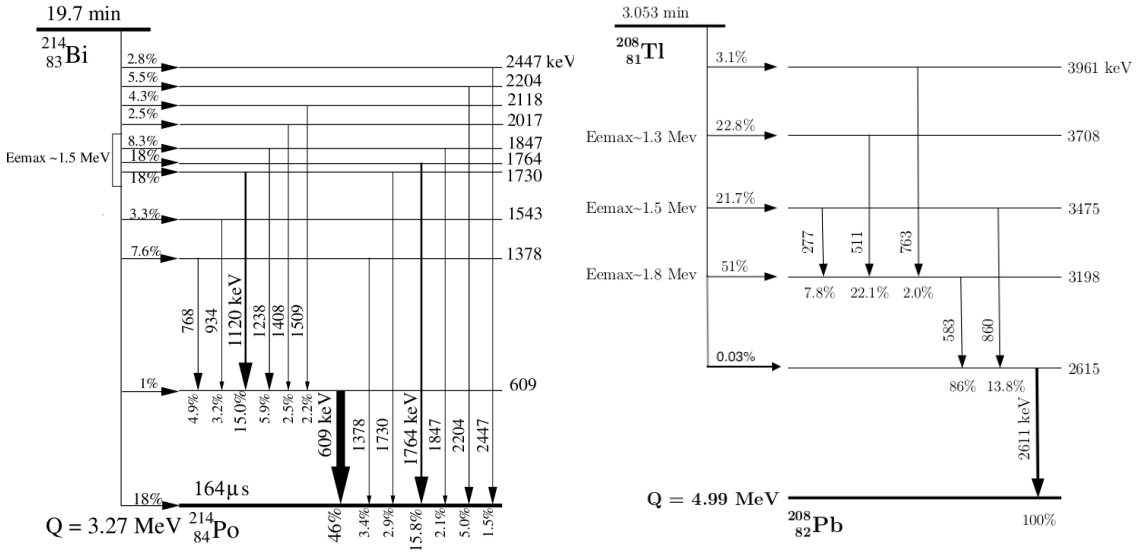

(a) ^{214}Bi decay scheme **(b)** ^{208}Tl decay scheme

Figure 6.13: Reminder of the decay schemes of ^{214}Bi and ^{208}Tl. The most common decay paths are shown in bold [52].

Cut Selection	^{214}Bi Foil Bulk	^{208}Tl Foil Bulk
1eNγ, electron energy $\geq$ 0.5 MeV	12.633 %	21.051%
$\geq$ 2.2 MeV	0.015 %	7.201 %
$\geq$ 2.3 MeV	0.004 %	6.688 %
$\geq$ 2.4 MeV	0.001 %	5.995 %
$\geq$ 2.5 MeV	0 %	5.031 %
$\geq$ 2.6 MeV	0 %	4.365 %

Table 6.7: ^{214}Bi Foil Bulk and ^{208}Tl Foil Bulk efficiencies following a 1eNγ, 0.5 MeV, and varying total gamma energy cuts.

The efficiencies in Table 6.7 were calculated by plotting the total gamma energy and finding the area under the histograms for each threshold. Based on these results, an optimal cut on the total gamma energy of 2.3 MeV was chosen to reduce the ^{214}Bi background by a factor of ten, compared to the 2.2 MeV cut, whilst maintaining a reasonable efficiency for ^{208}Tl.

Using the efficiencies calculated in the tables above, as well as the most recent measurements of the activities (see Table 6.1, scenario 3), the expected time to measure one event was calculated Table 6.8.

Background	Cut Selection	Efficiency	Time for 1 event
^{214}Bi Foil	1e1α, $E_e \geq 0.2$ MeV, from foil	1.68 %	9.2 hr
^{214}Bi Wires	1e1α, $E_e \geq 0.2$ MeV	16.35 %	0.7 hr
^{208}Tl Foil	1eNγ, $E_e \geq 0.5$ MeV, $E_\gamma \geq 2.3$ MeV	6.69 %	10.9 hr

Table 6.8: Table of the calculated efficiencies for ^{214}Bi in the foil and the tracker wires, as well as ^{208}Tl in the foil, with the expected time for one event

This initial study was then developed to investigate the exposure time needed to reach target sensitivity levels for ^{214}Bi and ^{208}Tl in the bulk of the foil. Results of this can be seen in the sections below.

6.3.3 ^{208}Tl in the Foil

It is clear from Table 6.7, that it is possible to measure the ^{208}Tl activity with negligible background from ^{214}Bi foil bulk events, when a cut of ≥ 2.2 MeV on electron energy is applied. This is further improved by introducing the cut on the total gamma energy of ≥ 2.3 MeV (Table 6.7). Therefore, with the assumption of an absence of backgrounds or negligible backgrounds, the activity can be estimated as:

$$A < \frac{2.3}{\epsilon \times m \times t}, \tag{6.1}$$

where A is the activity, ϵ is the efficiency, m is the source foil mass in kilograms, and t is the exposure in seconds. The statistical constant, 2.3, is the upper limit

for the mean of the Poisson distribution for a 90% CL, given 0 observed events. The mass used was 6.25416 kg [109], calculated by summing all of the masses of the produced Selenium pads. The efficiency, $\epsilon = 6.688\%$, used is after the 1eNγ topology, electron energy ≥ 0.5 MeV and total gamma energy ≥ 2.3 MeV cuts. The tracker efficiency is mostly accounted for in the simulation, reconstruction and selection cuts of events. However, additional contributions occur with hardware issues. For example, a number of dead channels have been found in the SuperNEMO demonstrator. This is currently accounted for by an expected tracker efficiency of 90%, however it is subject to change with the repair of dead cells and continued commissioning. Using this initial estimates, gives:

$$\epsilon = 6.688\% \times 0.9 = 6.0192\% \tag{6.2}$$

Figure 6.14 shows the expected sensitivity, calculated using Equation (6.1), as a function of the exposure. It is evident from this, that to reach a sensitivity equivalent to the target ^{208}Tl activity of 2 µBq/kg an exposure time of approximately 5 weeks is needed.

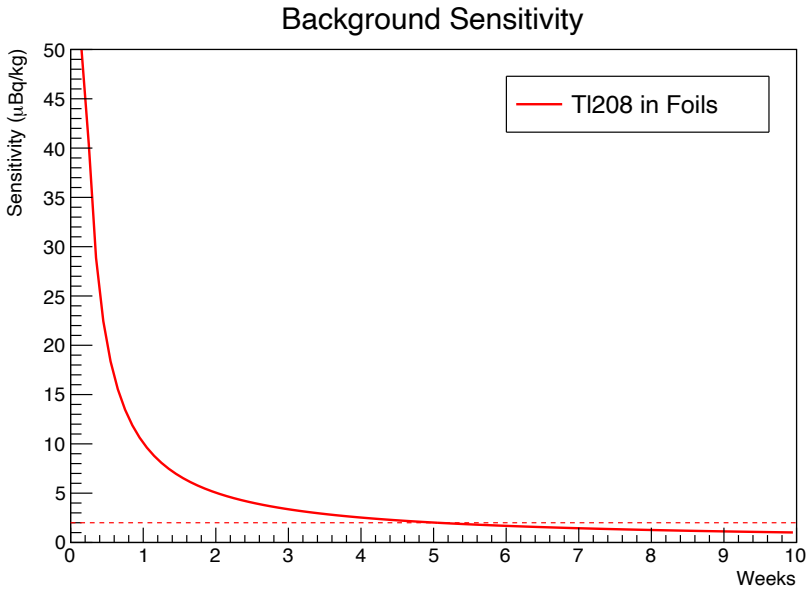

Figure 6.14: Sensitivity to ^{208}Tl background as a function of time. The dashed red line shows the target activity of ^{208}Tl at 2 µBq/kg.

6.3.4 ^{214}Bi in the Foil

When considering ^{214}Bi in the foil, it is necessary to account for the background from radon events in the gas. Therefore, the following formula is used to estimate the activity:

$$A < \frac{\sqrt{A_{gas} \times \epsilon_{gas} \times t} \times 1.64}{\epsilon_{foil} \times m \times t}, \tag{6.3}$$

where A_{gas} is the activity of the gas, ϵ_{gas} is the efficiency of the gas, and ϵ_{foil} is the efficiency of the foil. The statistical constant 1.64, converts from 1σ to a 90% CL for a Gaussian distribution. From Table 6.1, $A_{gas} = 2.28$ mBq. The values used for $\epsilon_{gas} = 7.94\%$ and $\epsilon_{foil} = 1.68\%$ were taken from the results following the 1e1α, electron energy ≥ 0.2 MeV, and vertex on the foil cuts. Both of these efficiencies were then scaled by 0.9 to account for tracker efficiency. Finally, ϵ_{gas} was scaled by an additional 0.5. ^{214}Bi in the tracker gas is deposited on the surface of the wires, therefore, there is a chance that the released alpha decays either into the gas or into the wire itself. In the latter case, the alpha would not be detected and the event would be rejected. The effect of this is estimated by assuming 50% of events are lost. The final efficiencies are:

$$\begin{aligned} \epsilon_{gas} &= 7.94\% \times 0.9 \times 0.5 = 3.573\%, \\ \epsilon_{foil} &= 1.68\% \times 0.9 = 1.512\% \end{aligned} \tag{6.4}$$

Figure 6.15 shows the expected ^{214}Bi sensitivity (blue), calculated using Equation (6.3). Again, this is shown as a function of time and the target activities for the SuperNEMO demonstrator are indicated with dashed lines.The result for ^{208}Tl is also included to show the relative scales of these backgrounds.

In Figure 6.18, it can be seen that to reach the target sensitivity of 20 µBq/kg, the demonstrator would need to run for approximately 100 weeks. It should be noted that this result could be improved on by considering additional cuts for ^{214}Bi. For example, further topological constraints could be explored using the 1eNγ channel. Checking the position of the alpha vertex would help to distinguish between ^{214}Bi foil bulk and tracker wire events. The inclusion of other alpha par-

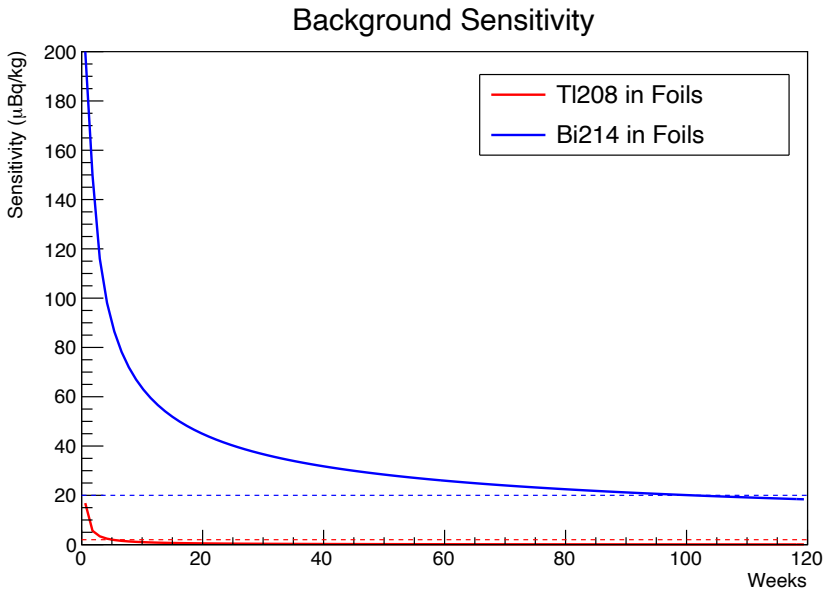

Figure 6.15: Sensitivity to ^{214}Bi (blue line) and ^{208}Tl (red line) backgrounds as a function of time. The dashed red line shows the target activity of ^{208}Tl at 2 µBq/kg. The dashed blue line is the ^{214}Bi target activity of 20 µBq/kg.

ticle properties, such as the hit count and track length, in the sensitivity module, could also help to reduce the background from events in the gas.

During the course of this Ph.D, the author completed initial machine learning studies to investigate the distinguishing power of different variables, including those mentioned above. These studies involved using Boosted Decision Tree (BDT) to identify the accuracy and precision with which signal could be separated from the backgrounds. Whilst this thesis will not go into the full details, an overview is provided here.

Firstly, a BDT was trained to separate $0\nu\beta\beta$ events from a combined background of $2\nu\beta\beta$, ^{214}Bi, ^{208}Tl, and radon. The features used were total calorimeter energy, energy of the highest-energy electron candidate, energy of the second-highest-energy electron candidate, angle between tracks, internal and external probabilities. When the different contributions of backgrounds were taken into consideration, a separation could be seen between signal and background with a Receiver Operating Characteristic (ROC) area under the curve of 0.96 (Figure 6.16). A result of 1.0 would be a perfect classifier, and 0.5 represents random guessing. The

most powerful feature variables for separation were found to be the total calorimeter energy and the energy of the highest-energy electron candidate.

In the following plots, the true positive rate is often referred to as the sensitivity, recall, or hit rate, and is the probability of detection. The false positive rate on the other hand is the probability of a false alarm.

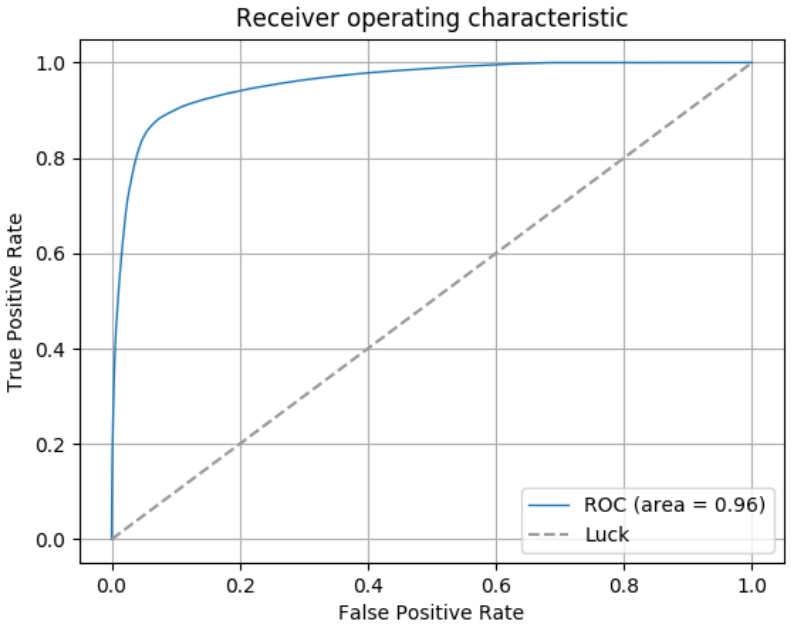

Figure 6.16: ROC curve result for a BDT trained to separate the $0\nu\beta\beta$ signal from the combined internal backgrounds of $2\nu\beta\beta$, ^{214}Bi, ^{208}Tl, and radon. The grey dashed line represents the result for random guessing.

The author also began testing multi-classifiers, for example being able to separate out the individual backgrounds. This involved training another BDT on internal backgrounds of $2\nu\beta\beta$, ^{214}Bi, ^{208}Tl, and radon. The ROC curve can be seen below in Figure 6.17, where the results for $2\nu\beta\beta$ and ^{208}Tl were the most promising.

Whilst the potential for a different approach to analysis is demonstrated here, further work must be done to test the robustness of these methods, in particular on real experimental data.

In the next stage of the analysis, below, the alpha track length was studied in more detail and used to discriminate between the different sources of background.

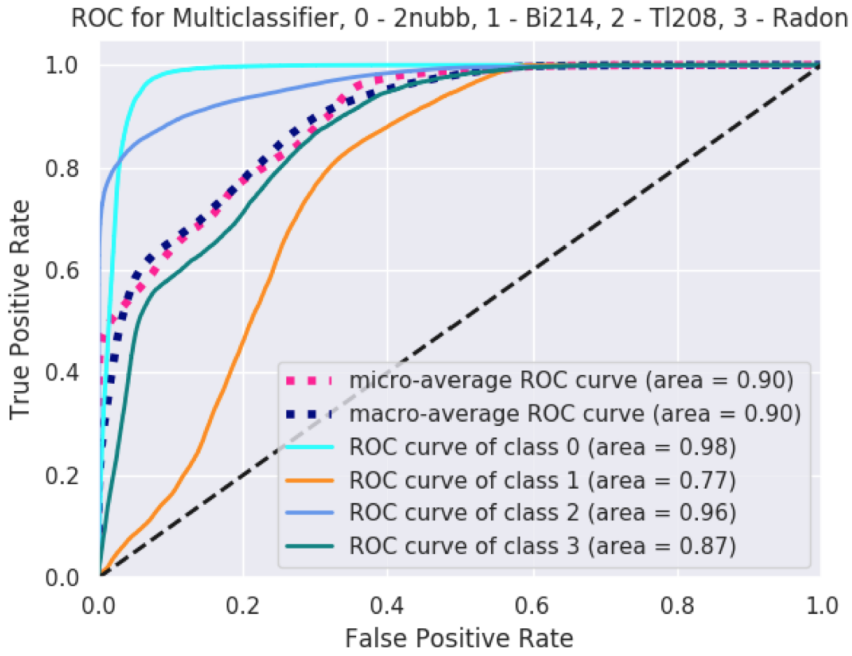

Figure 6.17: ROC curve result for a multi-class BDT trained to separate each of the internal backgrounds of $2\nu\beta\beta$, ^{214}Bi, ^{208}Tl, and radon.

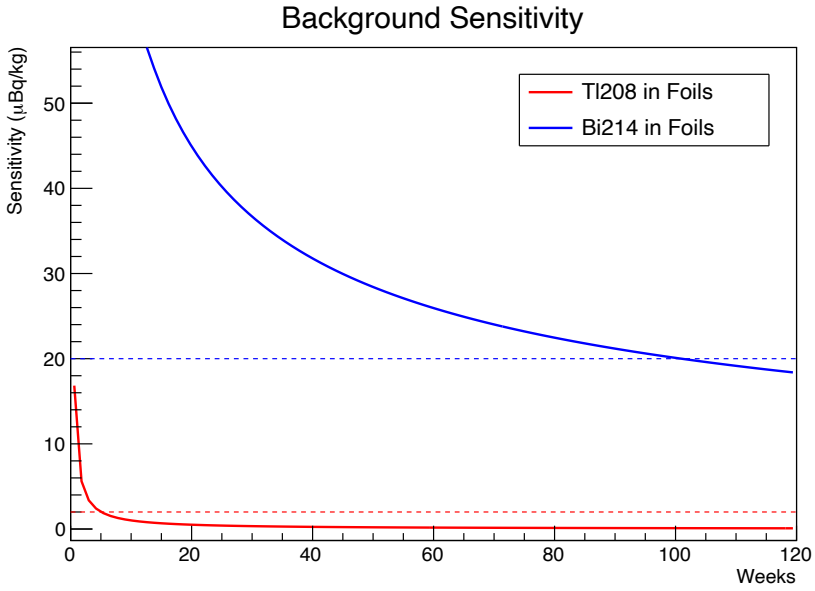

Figure 6.18: Zoomed view of sensitivity to ^{214}Bi (blue line) and ^{208}Tl (red line) backgrounds as a function of time. The dashed red line shows the target activity of ^{208}Tl at 2 µBq/kg. The dashed blue line is the ^{214}Bi target activity of 20 µBq/kg.

6.4 Relative Errors on Background Activities

The study above is informative regarding the required run time, of the SuperNEMO demonstrator, needed to reach sensitivities in the region of the target background activities for ^{214}Bi and ^{208}Tl in the foil. However, it is also useful to know the statistical precision to which these backgrounds, and others, can be measured. In this section, the relative errors are found for ^{214}Bi in the foil bulk, on the surface of the foil, and on the tracker wires. This builds on the work of T.Le Noblet [47], with fixes to the alpha finder algorithm and updated background activities. It was completed alongside F.Xie [110], with original work by the author, including the study of ^{208}Tl, and showing results for several different background activity scenarios.

In the process of calculating the relative errors, on the backgrounds described above, the first stage is to identify a clean channel to measure. As discussed previously, the 1e1α topology provides a a 'golden channel' for measuring ^{214}Bi. However, when disentangling contributions from the foil bulk, foil surface and tracker wires it is necessary to find another discriminating variable.

6.4.1 Search for Discriminating Variable

For this study, all of the simulated events detailed in Table 6.3 were used. The cut sequence and efficiency (ϵ) results for ^{214}Bi in the bulk of the foil, on the surface of the foil, and on the tracker wires are shown in Table 6.9, Table 6.10, and Table 6.11 respectively. Errors shown are calculated using binomial statistics. It should be noted that e^-/e^+ is shown before a charge cut is made, and therefore the reconstructed particle could be an electron or positron. For the 1e1α topology, this allows events with a total of two tracks; one identified as an electron, and one as an alpha. For this analysis, foil events have been selected in the cuts, to reject events from the tracker. This is to allow for studies of the background events when a foil selection cut is made for signal events.

It can be seen from the results summarised in Table 6.9, Table 6.10, and Table 6.11, that the efficiencies for ^{214}Bi foil bulk and foil surface events are similar for a selection requiring one electron from the foil that hits the main wall. How-

Cut Selection	^{214}Bi Bulk ϵ	$\Delta\epsilon$
≥ 1 reconstructed track	47.915 %	0.047 %
1 e^-/e^+	45.148 %	0.045 %
1 e^-/e^+ from foil	40.962 %	0.041 %
1 e^-/e^+ from foil and hits main wall	37.860 %	0.037 %
1 e^- from foil and hits main wall	35.322 %	0.035 %
1 e^- from foil, hits main wall, $\geq 1\alpha$	2.9249 %	0.0024 %
1e1α, e^- from foil, hits main wall	2.3943 %	0.0018 %
1e1α, e^- from foil, hits main wall, and α from foil	1.7339 %	0.0011 %

Table 6.9: Background efficiencies for topological and vertex position cuts on 1×10^6 ^{214}Bi Foil Bulk events.

Cut Selection	^{214}Bi Surf ϵ	$\Delta\epsilon$
≥ 1 reconstructed track	48.754 %	0.048 %
1 e^-/e^+	46.039 %	0.046 %
1 e^-/e^+ from foil	40.812 %	0.040 %
1 e^-/e^+ from foil and hits main wall	37.454 %	0.037 %
1 e^- from foil and hits main wall	35.011 %	0.035 %
1 e^- from foil, hits main wall, $\geq 1\alpha$	10.827 %	0.010 %
1e1α, e^- from foil, hits main wall	8.9946 %	0.0085 %
1e1α, e^- from foil, hits main wall, and α from foil	8.3246 %	0.0078 %

Table 6.10: Background efficiencies for topological and vertex position cuts on 1×10^6 ^{214}Bi Foil Surface events.

Cut Selection	^{214}Bi Wire ϵ	$\Delta\epsilon$
≥ 1 reconstructed track	42.788 %	0.042 %
1 e^-/e^+	39.896 %	0.039 %
1 e^-/e^+ from foil	15.593 %	0.015 %
1 e^-/e^+ from foil and hits main wall	14.402 %	0.014 %
1 e^- from foil and hits main wall	12.915 %	0.012 %
1 e^- from foil, hits main wall, $\geq 1\alpha$	6.3296 %	0.0058 %
1e1α, e^- from foil, hits main wall	1.40490 %	0.00075 %
1e1α, e^- from foil, hits main wall, and α from foil	0.88240 %	0.00032 %

Table 6.11: Background efficiencies for topological and energy cuts on 1×10^6 ^{214}Bi Tracker Wires events.

ever, the requirement for reconstructed alphas to be present reduces the number of foil bulk events. This is to be expected given the high ionisation power of alphas. Alphas emitted from the surface of the foil do not have to traverse the high density source foils, and are therefore more likely to reach the tracking layers of the demonstrator and be detected. The efficiency for the events from the tracker wires is also expected to be small, given the requirement that both the electron and alpha should be from the foil.

After studying the contributions of 1e1α from each region of the detector, an analysis was performed to find a variable related to this topology that has a distinctive shape for each of the origin positions. Given the findings above, and the knowledge of alpha energy losses in the detector, alpha length was the primary focus. Using the saved variables in the Sensitivity Modules, and applying the final cut as in Table 6.9, Table 6.10, and Table 6.11, plots were made of the alpha length for each of the background locations. In all cases the `minimum_delayed_time` was set to the default of 10 µs and the `minimal_cluster_xy_search_distance` was set to the default of 40 cm.

It can be seen from Figure 6.19, that the alpha track length is a variable that has a distinctive shape for each of the background locations. Therefore this was used as the discriminating variable for the following precision studies. As described above, the track lengths of alphas coming from the bulk of the source foil are

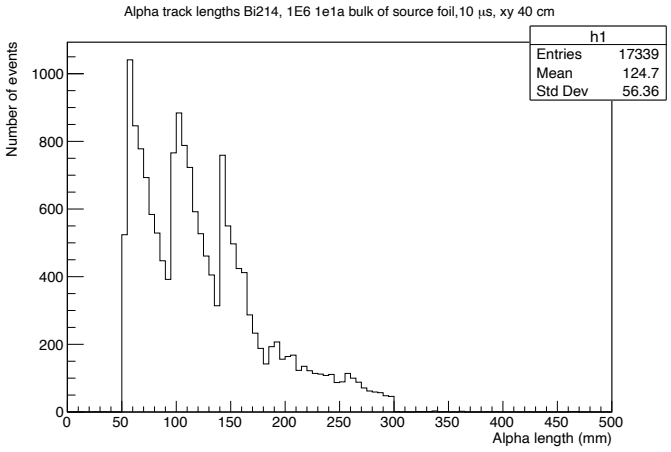

(a)

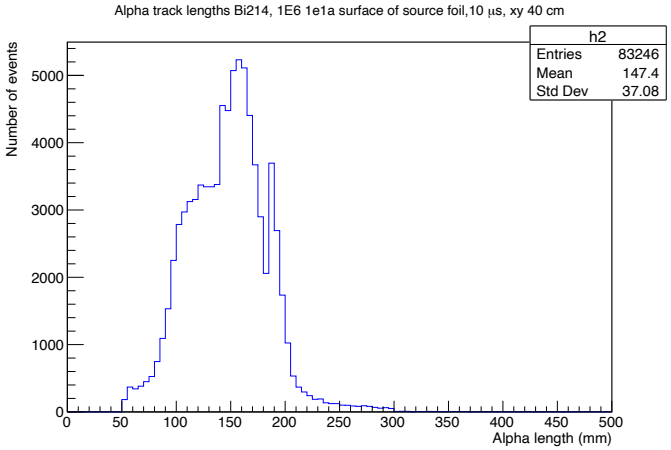

(b)

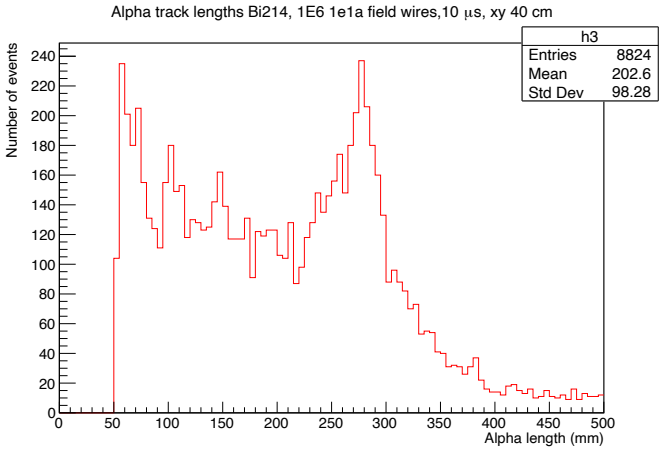

(c)

Figure 6.19: Alpha track lengths for ^{214}Bi events in the foil bulk (a), surface of the foil (b), and tracker wires (c). Cuts have been made on a 1e1α event with the electron and alpha both from the foil, and the electron hits the main wall.

expected to be shorter than those from the surface of the foil and in the tracker wires. This can be seen in Figure 6.19a, along with a multi peak distribution. Due to the configuration of the tracker, peaks are expected for each layer of tracker cells. For example, the first peak coincides with an alpha hitting the first layer of the tracker, the second peak with the second layer etc. The maximum track length of 45-50 cm is consistent with the distance from the foil to the calorimeter walls.

These distributions were then scaled by the activities listed in Table 6.1 and summed to give a reference plot from which pseudo data was created.

6.4.2 Pseudo Data & Fitted Activities

The cases studied in the following sections are as detailed in Table 6.1, beginning with the target activities.

Case 1 - Target Activities

As in Table 6.1, case one uses the target background activities for the SuperNEMO demonstrator. Figure 6.20 shows the individual alpha length spectra for each source of background, scaled to the target activities. Therefore, this plot accounts for the activity splits between the foil surface and tracker wires as well as the selections efficiencies. The black line indicates the summed distribution, from which pseudo data was then generated.

Pseudo experiments involve simulating real data events, in each bin, by generating random numbers of entries (n) according to Poisson's distribution. A random number generator is then used n times to create the data. The mean number of events used as the central point for the distribution was found by summing the expected number of events for each background source (N^i). In turn, the expected number of events were found using the following equation:

$$N^i_{cut} = \epsilon^i_{cut} \times A^i \times T, \tag{6.5}$$

where ϵ is the efficiency, A the activity, T the exposure time, and i the background selected i.e ^{214}Bi in the bulk of the foil. The cut made here is on a 1e1α

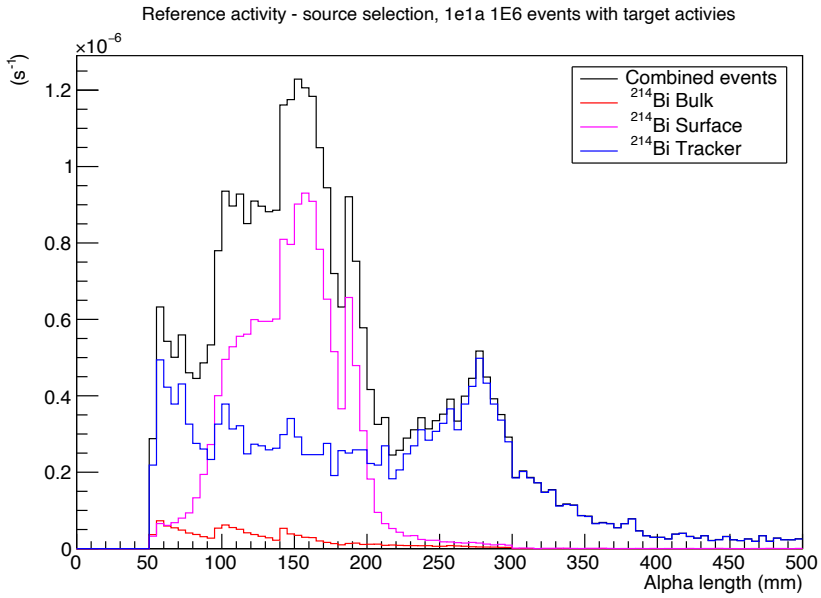

Figure 6.20: Reference activities as a function of alpha length for ^{214}Bi in the bulk (red line), surface (pink line) and tracker (blue line), weighted by the target activities and summed (black line).

topology with electron and alpha both from the foil, and the electron hitting the main wall. The efficiency is calculated by finding the number of events after cuts and dividing by the total events generated. Figure 6.21 shows an example pseudo experiment for a 180 day exposure. Errors displayed here are calculated based on the Poisson distribution.

The next stage of the analysis was to fit the pseudo data with the three ^{214}Bi background distributions. From this, an estimated activity could be found by comparing the original 'known' fractions of ^{214}Bi contributions, with those found during the fitting. Fitting was performed using TFractionFitter [111]. This ROOT based software does a standard likelihood fit using the Poisson distribution. Template MC histograms are supplied by the user and also varied statistically to contribute to the overall likelihood. For this analysis, the MC histograms are the three distributions seen in Figure 6.19, scaled to both activity and exposure. In the instance that a fit is successful, the results of the fit are plotted along with the template fractional histograms and pseudo data. If TFF fails this is indicative of low statistics in some of the template or data histograms. When this happens, statistics can be increased by increasing the exposure time and/or the activity.

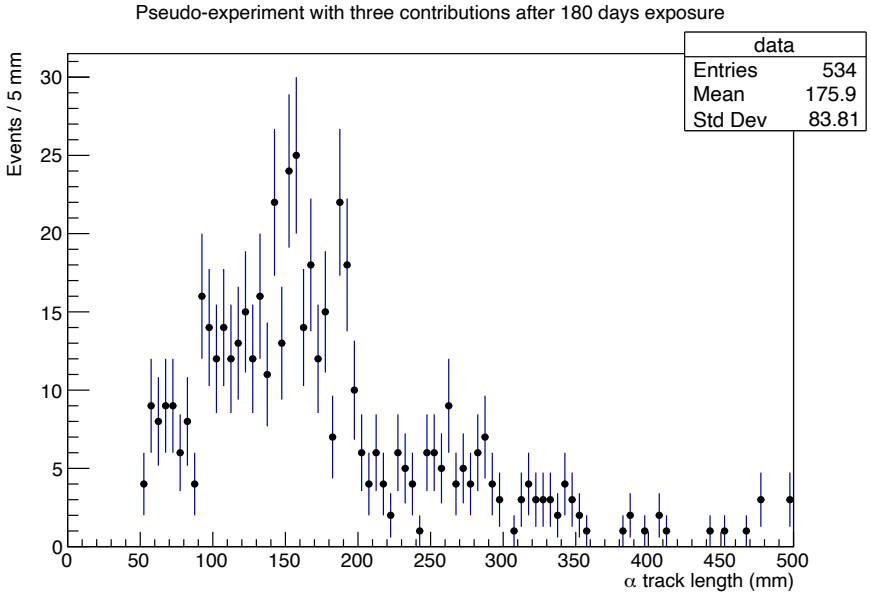

Figure 6.21: Example pseudo experiment data for the SuperNEMO demonstrator ^{214}Bi target activity, after an exposure of 180 days.

Additionally, smoothing the data histogram removes some of the fluctuations, increasing statistics in some bins, making it easier to fit. An example of a before and after smoothing can be seen in Figure 6.22. The smoothing function in Root uses an algorithm involving running medians and quadratic interpolation for flat segments.

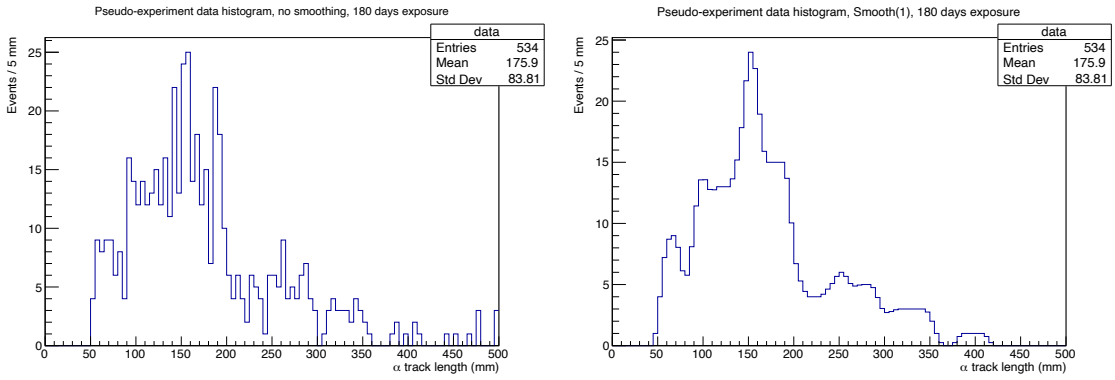

(a) **(b)**

Figure 6.22: Pseudo data histograms of alpha track lengths, before (a) and after (b) smoothing.

When first attempting to fit the pseudo data for a 180 day exposure and target activities of ^{214}Bi in the bulk = 62 µBq, surface = 0.178 mBq and tracker = 2.25 mBq, TFF fails to converge. The exposure was gradually increased and smoothing introduced until a fit was achieved. At an exposure of 410 days with the pseudo data histogram being smoothed once, the fit was successful. Figure 6.23 shows an example of this, where errors are found using Poisson distribution.

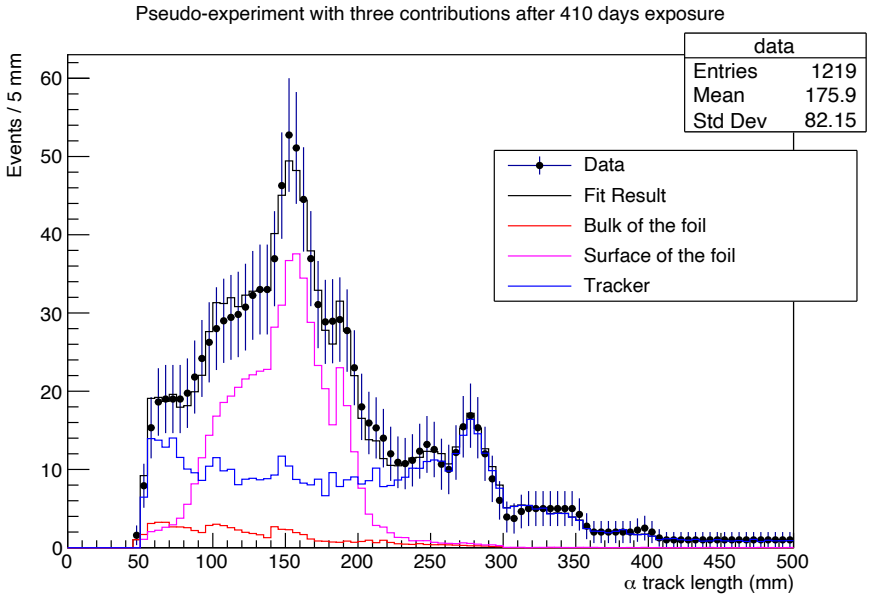

Figure 6.23: Example pseudo experiment data for the SuperNEMO demonstrator ^{214}Bi target activity, after an exposure of 410 days. The fitted fractions for each component of the background are shown, alongside the pseudo data, that has been smoothed once, and the fit result.

The TFF results and their errors for each background contribution, compared with the known original values can be seen in Table 6.12. All of the TFF calculated fractions are in agreement, within errors, with the known fractions. Using the ratio of the known and TFF fractions, new calculated activities were also found (Table 6.13).

With consistent successful fitting, the process would be to continue generating pseudo data, fit using TFF and find the activity of each component. This would be repeated 10^5 times. The resultant plot would then be fitted with a Gaussian

Background Source	Known Fraction	TFF Fraction	Δ TFF
^{214}Bi bulk	0.0311731	0.058	0.053
^{214}Bi surface	0.429861	0.457	0.047
^{214}Bi tracker	0.538966	0.485	0.047

Table 6.12: Table of example TFF results and errors, when fitting pseudo ^{214}Bi data with the bulk, surface and tracker background contributions. These are compared with the known initial fractions.

Background Source	Known Activity	TFF Activity	Δ Activity
^{214}Bi bulk	62 µBq	114 µBq	110 µBq
^{214}Bi surface	0.178 mBq	0.189 mBq	0.019 mBq
^{214}Bi tracker	2.25 mBq	2.0 mBq	0.2 mBq

Table 6.13: Table of example calculated activities for ^{214}Bi bulk, surface, and wires from TFF results, compared with known input activities.

and the mean activity (μ) and standard deviation (σ) found. Finally, the relative error would calculated as the ratio σ/μ. For the exposure above, of 410 days, and the use of smoothing, when running 10^5 times a fit was not consistently achieved. Therefore the exposure was increased to 1000 days to attempt to find relative errors.

The resultant activities for the bulk, surface and wire after 10^5 pseudo data runs can be seen below in Figure 6.24. In each case, a Gaussian has been fitted and the mean and standard deviation recorded.

Table 6.15 shows a summary of the values found and the final relative errors for an exposure of 1000 days.

Whilst the results for the surface and tracker activities were in good agreement with the values inputted, the fit results for the foil bulk were inconsistent. The distribution is not well described by a Gaussian fit, and has a large standard deviation, owing to a large tail (as seen in Figure 6.25). This tail is due to poor fitting

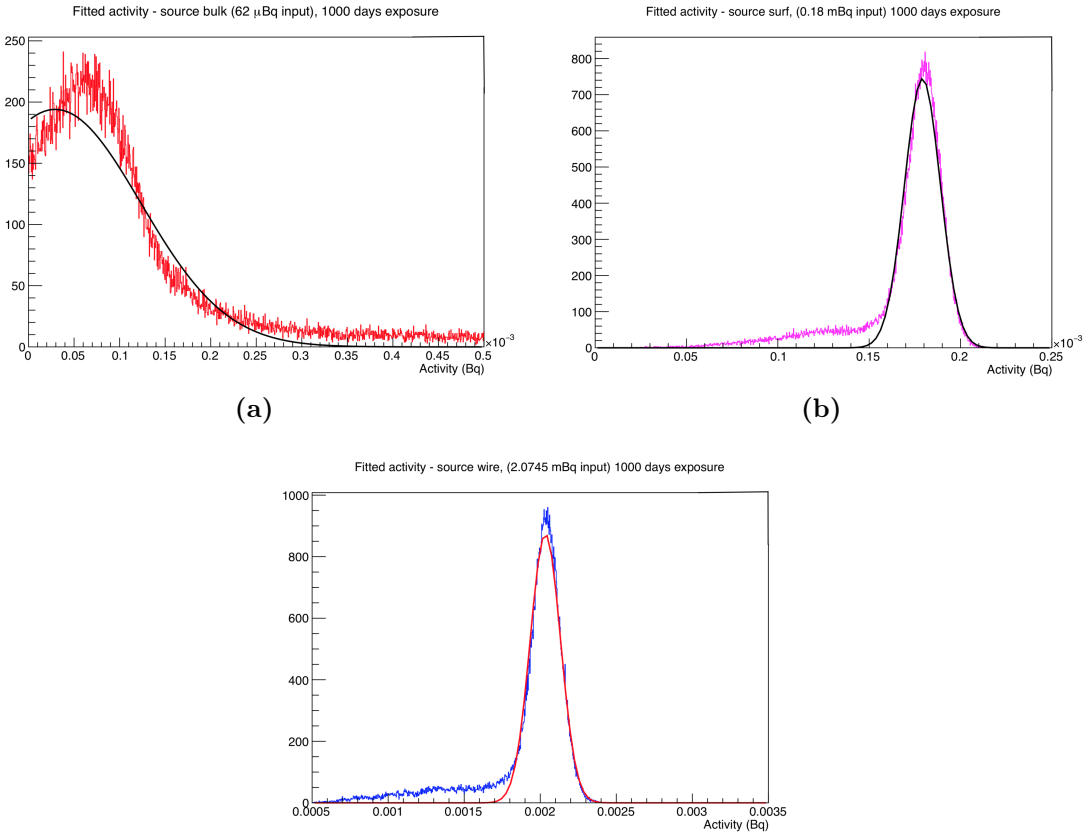

Figure 6.24: Fitted activities after 10^5 pseudo experiments for ^{214}Bi events in the foil bulk (a) where the black line is the Gaussian fit, surface of the foil (b) where the black line is the Gaussian fit, and tracker wires where the red line is the Gaussian fit (c). The exposure is set to 1000 days and a Gaussian has been fitted to extract the mean and standard deviations.

Background Source	Input Activity	Mean (μ)	Std. Dev (σ)	Relative Error
^{214}Bi bulk	62 µBq	29.3 µBq	93.9 µBq	321%
^{214}Bi surface	0.178 mBq	0.179 mBq	0.010 mBq	5.49%
^{214}Bi tracker	2.25 mBq	2.03 mBq	0.100 mBq	4.91%

Table 6.14: Table of the ^{214}Bi activities, alongside the mean, standard deviations, and calculated relative error from the Gaussian fit for an exposure of 1000 days.

results from TFF, most likely due to low statistics for the bulk in the pseudo experiment data.

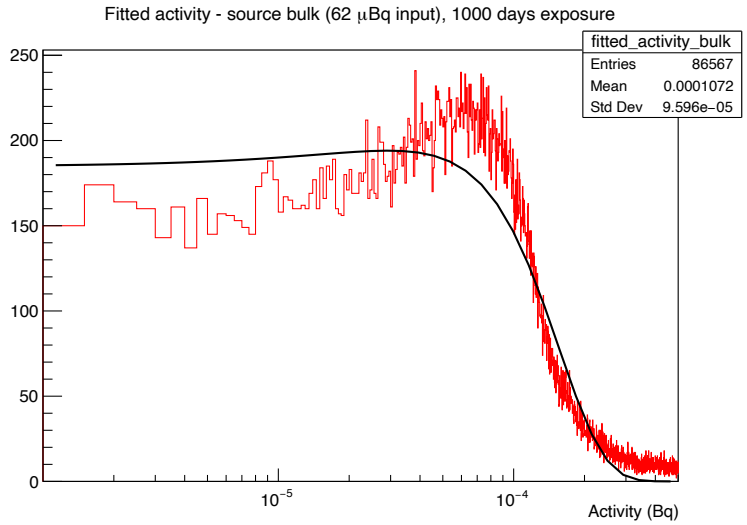

Figure 6.25: Fitted activities after 10^5 pseudo experiments for ^{214}Bi events in the foil bulk where the black line is the Gaussian fit. Exposure is set to 1000 days and a Gaussian has been fitted to extract the mean and standard deviations. A log scale is shown on the x-axis.

It should be noted, that whilst this was a helpful exercise in developing the method for relative error calculation, it is unlikely that SuperNEMO will achieve this target level of 62 µBq in the demonstrator. Therefore, studies detailed in §6.4.2, and §6.4.2 focussed on more realistic background activities from recent measurements using the RnCL and BiPo-3.

TFF Linearity Check

In order to sense check the TFF results, a short test was devised, in which the input activities for the foil bulk, surface and tracker wires were varied by ± 20%. The calculated output activities from TFF results were then plotted against the input to check for linearity. Figure 6.26 shows this linearity check for the ^{214}Bi foil surface activities. In this case, the central activity was taken as 0.18 mBq. Errors were taken from the Gaussian fits made.

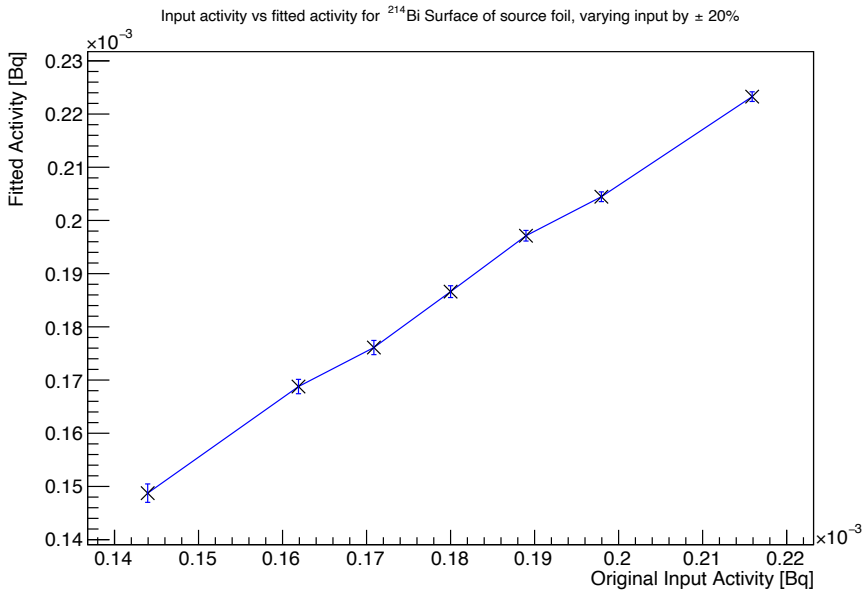

Figure 6.26: TFractionFitter calculated activities plotted against varying input activities for ^{214}Bi on the surface of the foil. Errors are taken from the Gaussian fit of resultant activities

Case 2 - 4.1 mBq Activity for ^{214}Bi Bulk

For this second case, exactly the same process was followed but with the bulk activity set to the new value of 4.1 mBq. This higher activity meant that fitting was possible at lower exposures of 14 days. Figure 6.27 shows the TFF fit to the pseudo data for an exposure of 180 days.

As described above, 10^5 pseudo experiments were run and activities calculated from the ratio of fractions. Activities were plotted and Gaussians fitted (Figure 6.28).

Table 6.15 shows a summary of the values found and the final relative errors for an exposure of 180 days.

Next, the relative errors were found for exposures of 14, 30, 60, 90, 120, 150 and 180 days. Figure 6.29 shows the results for each background component of ^{214}Bi.

It can be seen that for a 10% relative error on the ^{214}Bi bulk activity measurement, the detector would need to be run for $\approx$ 60 days. For the ^{214}Bi tracker ac-

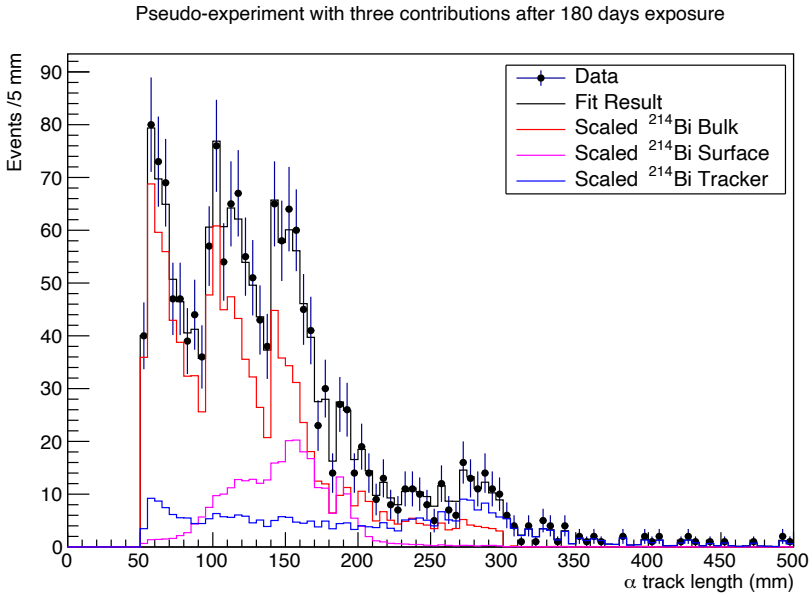

Figure 6.27: Example pseudo experiment data for the SuperNEMO demonstrator ^{214}Bi activity of 4.1 mBq, after an exposure of 180 days. The fitted fractions for each component of the background are shown, alongside the pseudo data and the fit result.

Background Source	Input Activity	Mean (μ)	Std. Dev (σ)	Relative Error
^{214}Bi bulk	4.1 mBq	4.13 mBq	0.23 mBq	5.48%
^{214}Bi surface	0.178 mBq	0.177 mBq	0.039 mBq	22.074%
^{214}Bi tracker	2.1 mBq	2.0 mBq	0.3 mBq	12.6%

Table 6.15: Table of the ^{214}Bi activities, alongside the mean, standard deviations, and calculated relative error from the Gaussian fit for case 2, with an exposure of 180 days.

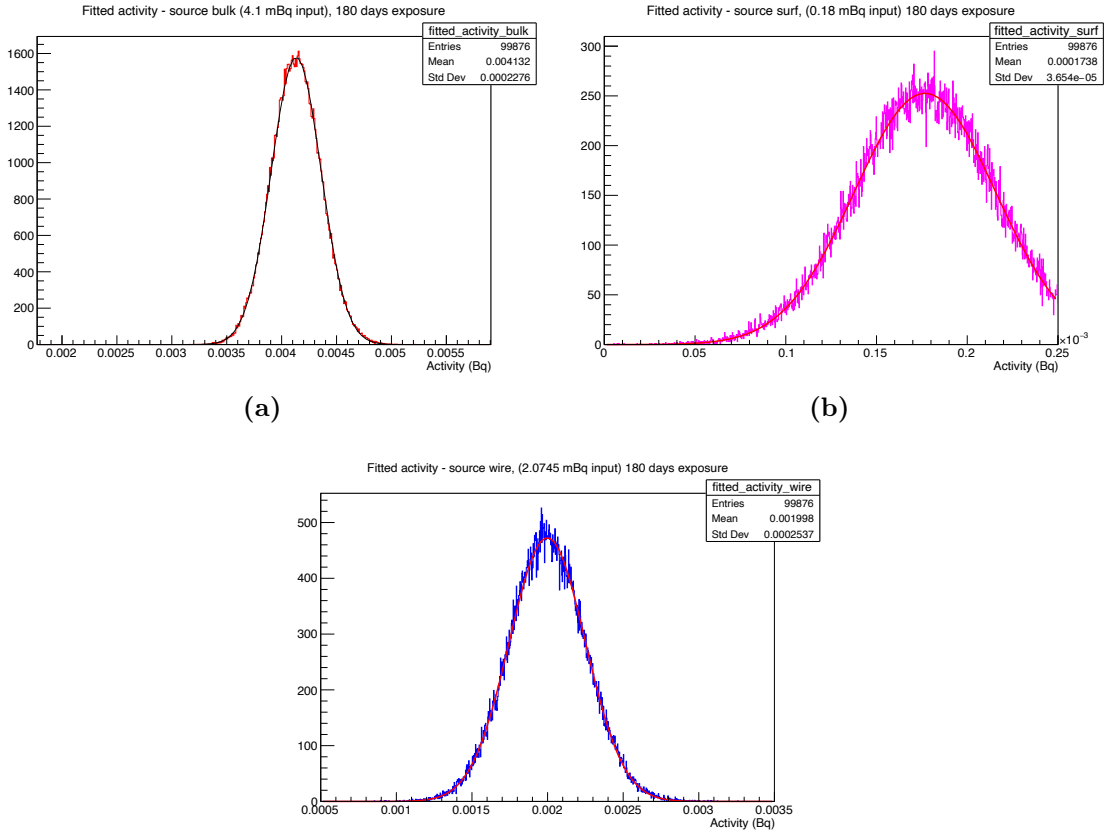

Figure 6.28: Fitted activities after 10^5 pseudo experiments for 4.1 mBq ^{214}Bi events in the foil bulk (a) where the black line is the Gaussian fit, surface of the foil (b) where the red line is the Gaussian fit, and tracker wires where the red line is the Gaussian fit (c). The exposure is set to 180 days and a Gaussian has been fitted to extract the mean and standard deviations.

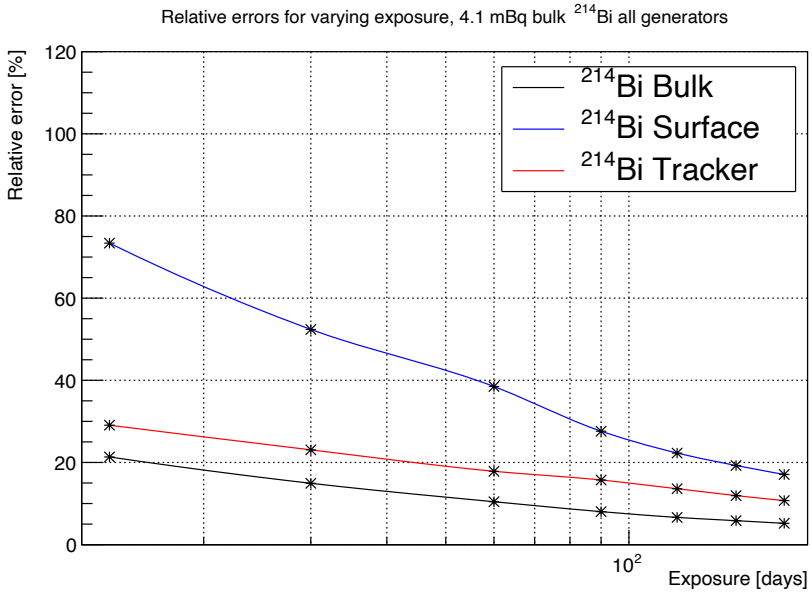

Figure 6.29: Plot of relative errors on ^{214}Bi component activities with varying exposures for a foil bulk activity of 4.1 mBq.

tivity it would be ≈ 180 days. Finally the surface activity measurement could be measured with a relative error of 20% after a run time of ≈ 150 days.

Case 3 - 1.8 mBq Activity for ^{214}Bi Bulk

Finally, the same procedure was followed for a ^{214}Bi bulk activity of 1.8 mBq. Figure 6.30 shows an example fit of one of the pseudo experiments with an exposure of 180 days.

Figure 6.31 plots the relative errors on the different component activities of ^{214}Bi over a range of exposures. A 20% relative error can be reached for the bulk, surface and tracker at ≈ 60 days, 100 days and 40 days respectively.

6.4.3 Relative error on ^{208}Tl activities

In order to find the relative errors for ^{208}Tl in the bulk of the foil, a similar method to the one detailed above was followed. Firstly, the 1eNγ channel was identified as one that has contributions from both ^{208}Tl and ^{214}Bi. The events simulated and

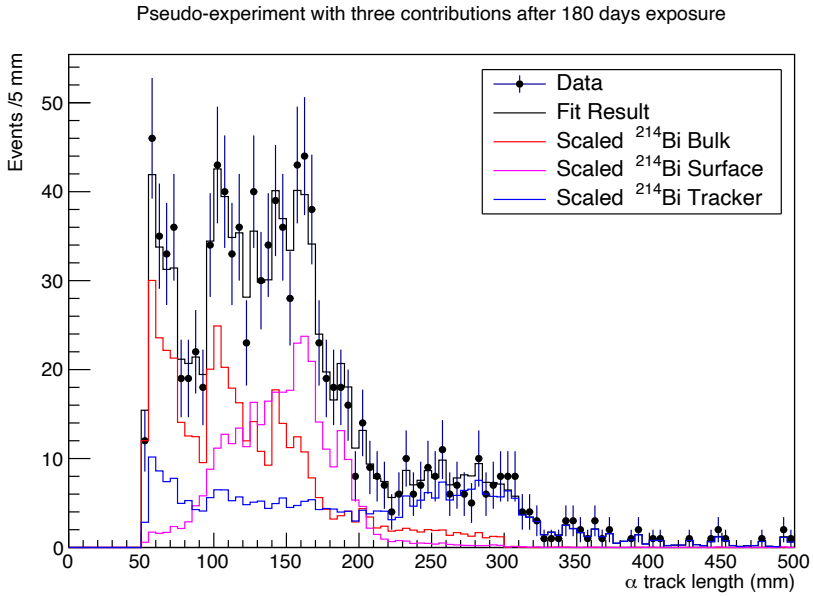

Figure 6.30: Example pseudo experiment data for the SuperNEMO demonstrator ^{214}Bi activity of 1.8 mBq, after an exposure of 180 days. The fitted fractions for each component of the background are shown, alongside the pseudo data and the fit result.

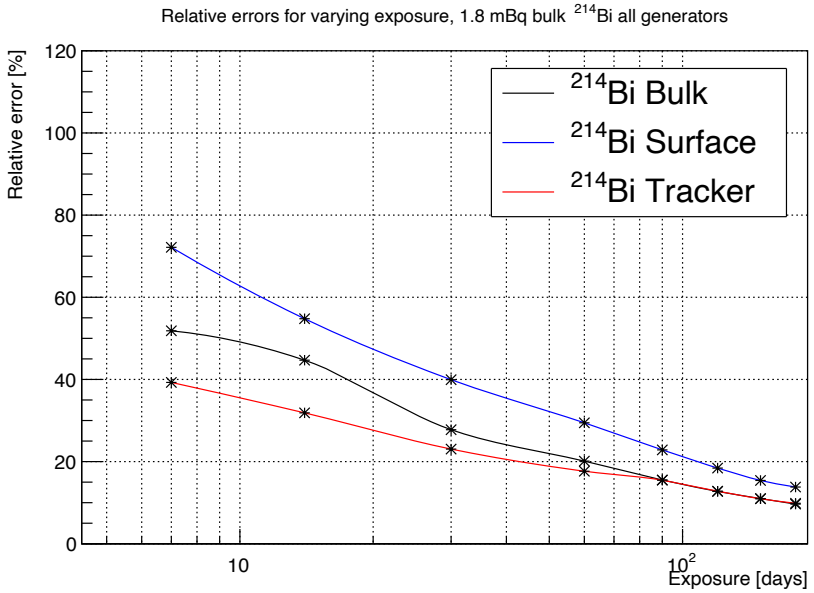

Figure 6.31: Plot of relative errors on ^{214}Bi component activities with varying exposures for a foil bulk activity of 1.8 mBq.

used were as in Table 6.3. Cuts were made as described in §6.3.2 with no alphas allowed, a selection for electrons coming from the foil and the energy threshold of $E_e > 0.5$ MeV. Efficiencies for these cuts on ^{214}Bi bulk, and ^{208}Tl bulk can be seen in Table 6.4 and Table 6.6 respectively. In the search for a variable with distinct shapes for ^{214}Bi and ^{208}Tl, the electron energy and total gamma energy were plotted (Figure 6.32).

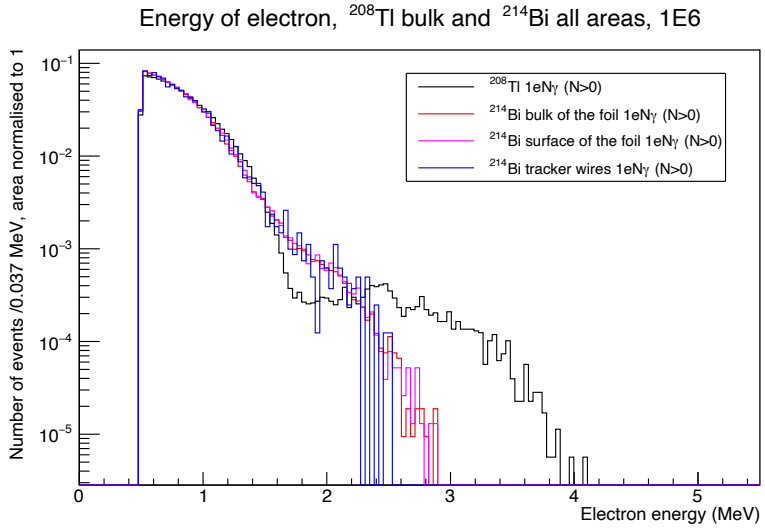

(a)

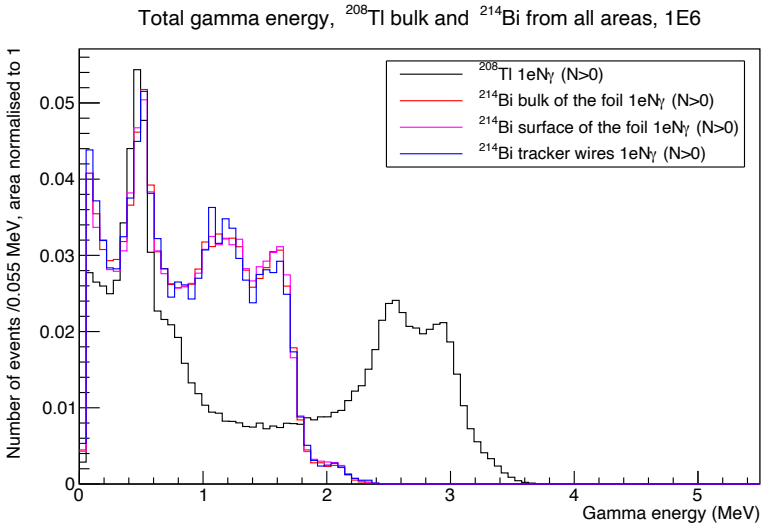

(b)

Figure 6.32: Electron energy (a) and total gamma energy (b) for 1eNγ events from ^{214}Bi components and ^{208}Tl with an electron energy cut of > 0.5MeV.

The total gamma energy was chosen as the distinguishing variable due to the difference in spectra between the ^{214}Bi and ^{208}Tl. Referring back to the decay schemes shown in Figure 4.1, the peaks in the ^{214}Bi spectra of Figure 6.32b can be associated to some of the main decay channels with E_γ = 609 keV, 1120 keV, and 1764 keV. For ^{208}Tl we see two peaks at ≈ 2.5 MeV and 3 MeV. This is consistent with decays resulting in the emission of 583 keV and 2.6 MeV gammas.

Reference activities for 370 µBq of ^{208}Tl in the bulk of the foil and for the combined (6.38 mBq) ^{214}Bi bulk (4.1 mBq), surface (0.178 mBq), and wire (2.1 mBq) were then plotted for the cuts detailed above. Each contribution was normalised by its activity. As described previously, pseudo experiments were then run 10^5 times, with an example of one run shown in Figure 6.33.

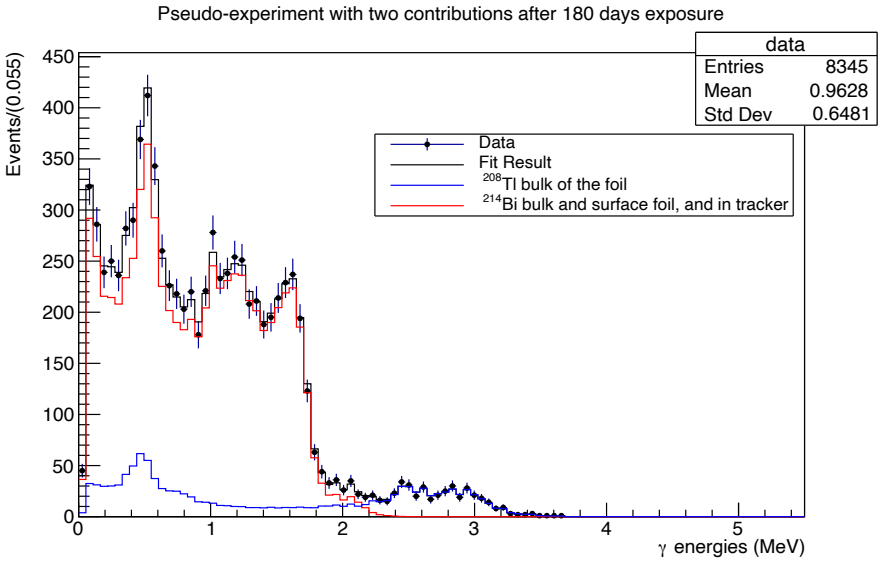

Figure 6.33: Example pseudo experiment data for the SuperNEMO demonstrator for 370 µBq ^{208}Tl in the bulk of the foil, and combined ^{214}Bi activity, after an exposure of 180 days. The fitted fractions for each component of the background are shown, alongside the pseudo data and the fit result.

Once again, the TFF activities were fitted with a Gaussian and the mean and sigma used to calculate relative errors. The relative error plot for 3, 7, 14, 30, 90, 120, 150 and 180 days exposure is shown in Figure 6.34.

From Figure 6.34, it can be seen that a relative error of 10% on the ^{208}Tl activity could be achieved in ≈ 40 days. A relative error of 5% is expected after a run time of ≈ 180 days. For the combined ^{214}Bi activities we can see that a 10% rela-

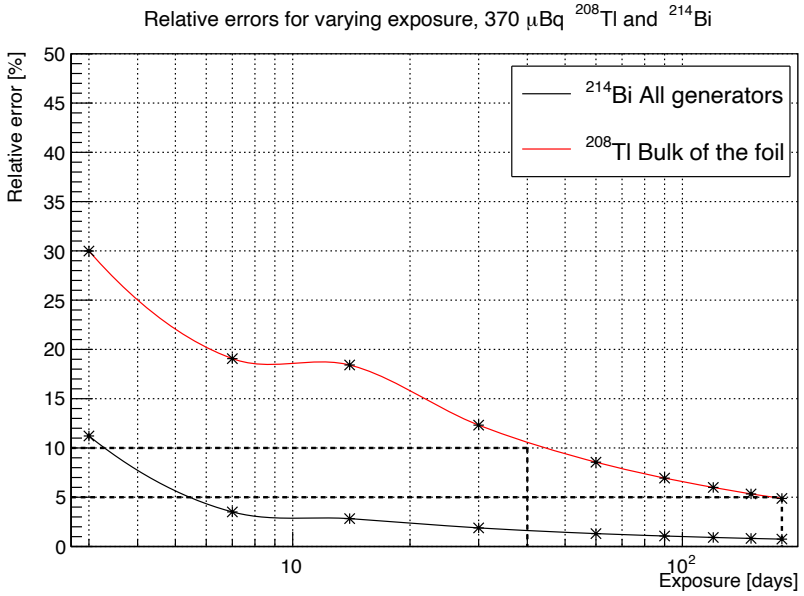

Figure 6.34: Plot of relative errors on 370 μBq of ^{208}Tl in the foil bulk and the combined ^{214}Bi activity in the foil bulk, on the surface of the foil and on the tracker wires. Results were found for exposures ranging from 3 to 180 days.

tive error could be achieved in as little as ≈ 3 days, with a 5% relative error after ≈ 5 days. The apparent bump in the spectrum at an exposure of 14 days, is most likely due to poor fitting of the Gaussian function for the previous 3 and 7 day exposures (Figure 6.35).

Reducing the number of bins in these finely binned plots, results in a change in the fitted gaussian mean, see Figure 6.36. Whilst this has not been explored in this analysis, this could form another source of systematic error on the final relative error results. It should also be noted that the inputted activity of 6.38 mBq only accounts for ^{214}Bi in the areas of the detector described, and assumes successful flushing of the detector to achieve such a suppression on the radon present.

Several assumptions were made for this analysis. Firstly, it does not account for any of the external (outside of the detector) backgrounds to the SuperNEMO experiment. Secondly, it assumes that ^{214}Bi ions present anywhere in the gap between the source and the first layer of tracker wires, will be deposited on the surface of the foil. However, in general, the analysis demonstrates that the tracker-calorimeter technique allows for the use of powerful background control channels.

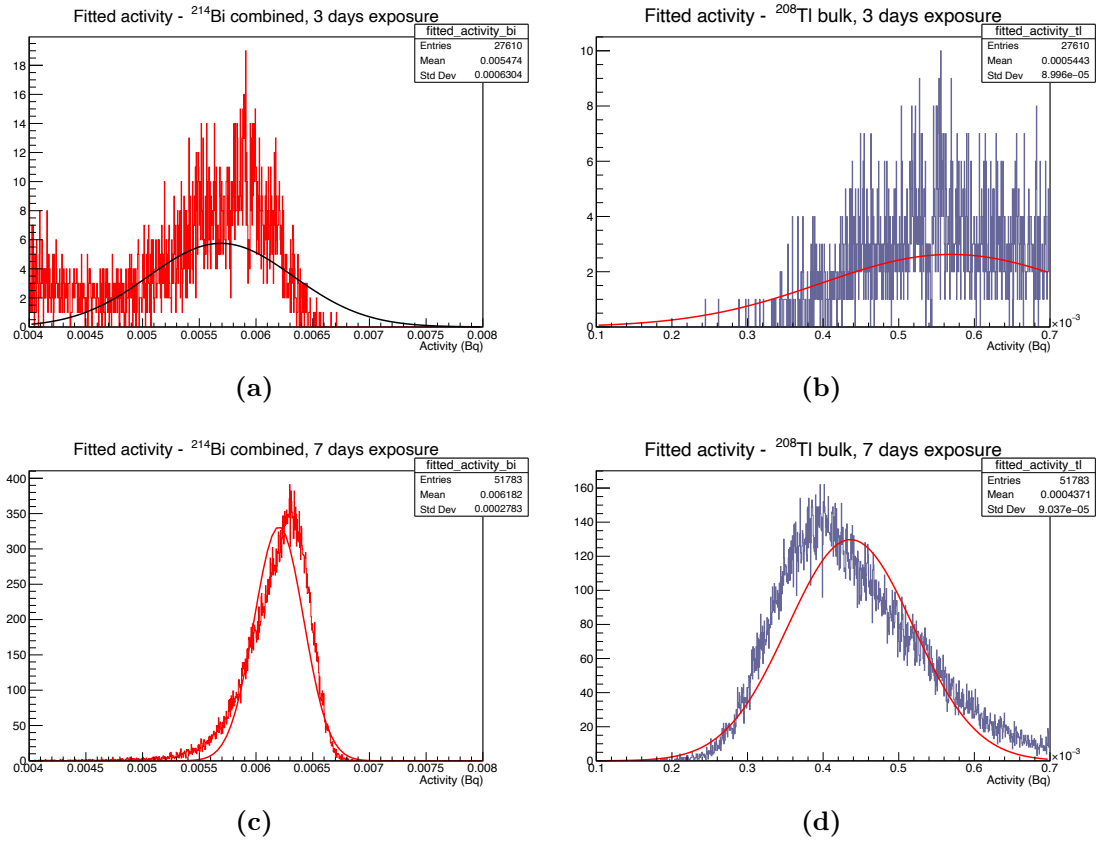

Figure 6.35: Fitted activities after 10^5 pseudo experiments for ^{214}Bi and ^{208}Tl foil bulk events after 3 day exposures (a) and (b) respectively, and 7 day exposures (c) and (d) respectively. Attempted Gaussian fits are shown on each plot.

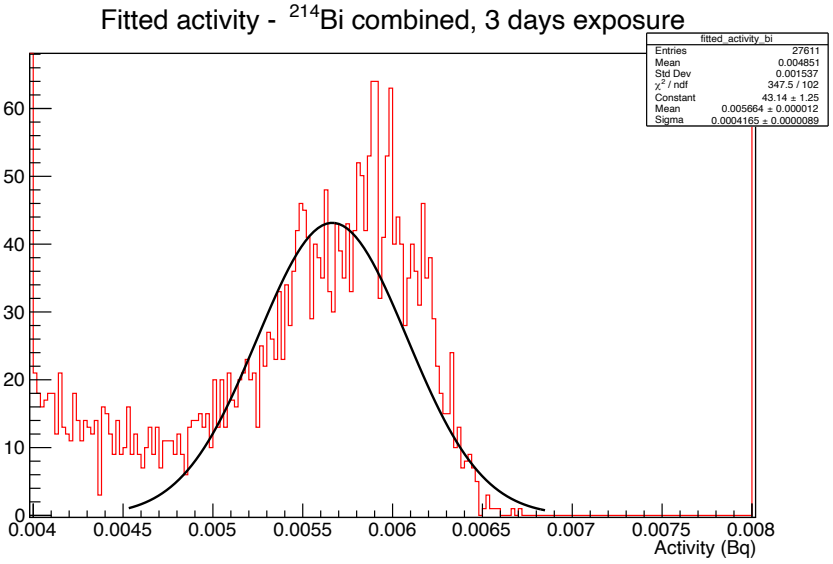

Figure 6.36: Fitted activities after 10^5 pseudo experiments for ^{214}Bi bulk events after 3 day exposures with reduced binning from 1000 to 200. Attempted Gaussian fit is also shown.

The study illustrates that it could be straightforward to measure internal backgrounds even with relatively short exposures.

Chapter 7

The SuperNEMO Gas System

Successful operation of the SuperNEMO tracker requires a precise mixture of gases to be supplied continuously to the detector volume. The drift gas is comprised of 95% helium, 4% ethanol and 1% argon. The purpose of the gas system is to control the fractions of gases, at a given flow rate. It also maintains a constant over-pressure inside the detector. This is important for keeping contaminants out of the tracking volume.

Initial set up and testing of the gas system was performed inside a clean room at the MSSL in Surrey, U.K. The equipment was then shipped in November 2016 to the LSM, France, for use in half detector commissioning.

This chapter covers details of the work undertaken by the author during the course of this Ph.D. This includes:

- updating hardware on the gas system to include new probes and sensors
- designing and building the electronics crate and all sensor readouts
- integrating readouts with the existing SuperNEMO Control & Monitoring System (CMS)
- writing all of the necessary command and readout scripts to enable remote control and monitoring
- designing and creating a Graphical User Interface (GUI) (in French and English) for easy remote and local monitoring of key variables

- testing the method for measuring ethanol levels as well as ambient pressure measurements

7.1 Gas System Operation

Gaseous helium and argon are supplied to the gas system through two main lines. Pressure relief valves early in the setup ensure that any over pressures introduced at the gas cylinders do not cause damage downstream. Each line passes through a filter to remove any particulates that may have been in the cylinders or upstream of the gas system. Figure 7.1 shows a schematic of the gas system, including the Bulleur Primaire (primary bubbler) (BP) and Froidisseur de Gaz (gas cooler) (FG).

The ratio of helium to argon is set using two Mass Flow Controllers (MFCs). The MFCs accurately measure and control the flow rates. As the gas passes through the device it is heated by symmetrical heating elements. Temperatures are measured where the gas is heated, and again at a later point [112]. Depending on the flow rate and composition of the gas a different temperature gradient is measured. Each MFC is calibrated by the manufacturer for a specific gas. This allows the flow rate to be measured. The controllers both contain an electronically operated valve which regulates the flow to the desired set point. These valves are controlled by a MKS PR4000B-F unit [113] that is connected to the MFCs. Normal operation of the system involves using the unit in slave mode. Argon's set point is taken from the helium channel signal ensuring the gas mixing ratio is kept constant.

As shown in Figure 7.1, the maximum flow rates for these MFCs are 1.3 m^3/h and 0.1 m^3/h for helium and argon respectively. NEMO-3 had a volume of $\approx$ 28 m^3 and a volume replacement time of around 4 days, flowing at 0.3 m^3/h. The SuperNEMO demonstrator module has a volume of $\approx$ 15 m^3. Using a gas mixing ratio of 1%, the range of helium flow rates allowed is from 0.2 m^3/h to 1.3 m^3/h. If a flow rate similar to NEMO-3 is assumed then one internal volume can be replaced in just over 2 days. A shorter time provides additional protection against daughters of radon being deposited in the tracker. Specifically, radon emanating from detector materials or diffusing into the tracker will be flushed out, before it

decays. However, if the gases are exchanged too quickly it can be wasteful and expensive to run. At the nominal flow rate of 0.5 m^3/h chosen for the SuperNEMO demonstrator, radon activity in the tracker is reduced by a factor of 5, compared to a static system [26]. A reduction by a factor of 12 can be achieved with a flow rate of 1.3 m^3/h [114]. This can be increased to the required 2.0 m^3/h, by replacing the MFCs. This will be done for the full SuperNEMO experiment.

Fast flow may be used to purge the detector with nitrogen after running. The gas system enables this by including a fast flow line, operating at 30 m^3/h. Flow rates in this section are controlled manually, as the MFCs are bypassed. Although not as accurate the rate can be varied using a flow control needle valve.

There are several failure modes that need to be considered in the gas system. As previously discussed, several pressure relief valves are included in the setup to prevent high pressures causing damage to the pipework. The over-pressure in the internal detector volume will be set using a glass bubbler at the output. Within the gas system, a back-pressure regulator sets the pressure in the main bubbler (Figure 7.1). In the event of this regulator or the MFCs failing, and high pressures building up, the relief valves will open to prevent the large over-pressure reaching the internal detector.

Studies of the pressure fluctuations caused by heavy road vehicles passing through the tunnel adjacent to the laboratory, have found variations larger than 10 mbar over a period of a few minutes [115]. This could cause the tracker to be momentarily above or below the nominal over-pressure, risking damage. To properly understand the fluctuations in ambient pressure at the LSM, a USB barometer has been installed. Results will be discussed later in this chapter (§7.5.2).

Whilst argon passes straight through the system, helium goes through two bubblers containing liquid ethanol. After the addition of ethanol the two gases are mixed. The output from the gas system is then connected to the detector.

7.2 Additional of Ethanol

Ethanol vapour is added to the helium in two stages. The amount of the ethanol added is determined by the pressure and temperature of the vessels. These con-

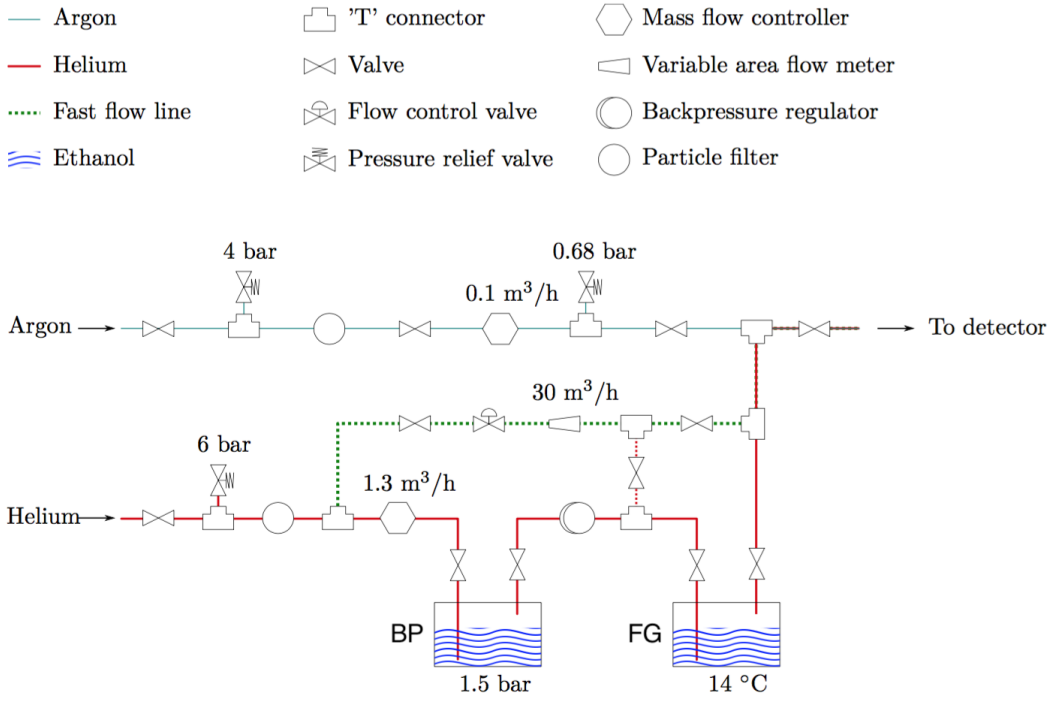

Figure 7.1: A flow diagram of the gas system configuration with flow from left to right. The helium, argon, and fast flow lines are identified by red, blue and green lines respectively. The diagram also shows the pressure release valves with the values above which they trigger. Typical operating values are shown for the pressure and temperature of the two ethanol baths. The numbers above the flow controllers show the maximum flow rate achievable [80].

ditions affect the evaporation rate of the liquid ethanol in to the gas flow. A $\approx$ 43 ℓ BP allows a high evaporation rate with exposure to a large surface area of ethanol. The BP is at a high pressure of $\approx$ 1.5 bar and ambient temperature, giving $\approx$ 4% ethanol. It is only approximate as the BP is not temperature controlled, so it subject to variations in ambient temperature. Ethanol added to the helium gas is also affected by changes in the ambient temperature. To finely tune the ethanol fraction, helium flows through a smaller Froidisseur de Gaz (gas cooler) (FG) at ambient pressure and controlled temperature. Following on from the BP it is necessary to set the FG to 14 °C, acquiring an ethanol fraction of 4%.

The dependence of the fractional volume of ethanol (V_i) on the BP pressure (p_{total}) can be explained by combining Amagat's and Dalton's laws. Amagat's law states that the volume (V_{total}) of a mixture of ideal gases is equal to the sum of the individual component gas volumes (V_i), at a constant temperature and pressure. For Dalton's law, the sum of all the partial pressures of the ideal gas components gives the total pressure (p_{total}), assuming a fixed temperature and volume. Applying the above to the ideal gas law and equating gives:

$$\frac{V_i}{V_{total}} = \frac{p_{vapour}}{p_{total}} \tag{7.1}$$

where i is for the individual components of the ideal gas mix, and p_{vapour} is the vapour pressure of ethanol that is one of the partial pressures in the system. Equation 7.1 shows the dependence of the fractional ethanol volume on the ratio of vapour pressure to the gas mix total pressure.

The ethanol vapour pressure can be calculated for ethanol with the Antoine equation. This describes the relationship between p_i and the temperature (T). It is the vapour pressure at which re-absorption of gas molecules on the surface equals evaporation from the surface. Vapour pressure is dependent on the temperature of the liquid surface, as given by:

$$\log_{10} p_{vapour} = A - \frac{B}{C + T} \tag{7.2}$$

where A, B and C are constants specific to the gas component concerned. For ethanol these values are A = 8.20417, B = 1642.89, C = 230.3 for T in °C and p in mmHg from [116]. Setting the temperature of the FG directly affects the

vapour pressure and thus the fractional ethanol volume. If the ethanol level is too high when it enters the FG, the vapour will condense in the 14 °C bubbler. However, if it is too low, additional ethanol will evaporate in to the gas flow.

Figure 7.2 shows the variation in the ethanol volume, depending on the pressure and temperature. In Figure 7.2b several realistic ambient temperatures are plotted. Dashed lines show the pressure that the BP must be set to, to achieve a nominal 4% ethanol. During tests at MSSL, a set point temperature of 14 °C was required. However, as shown in Figure 7.2a, this must be changed to ≈ 12 °C to account for the underground pressure, at the LSM, of 0.88 bar.

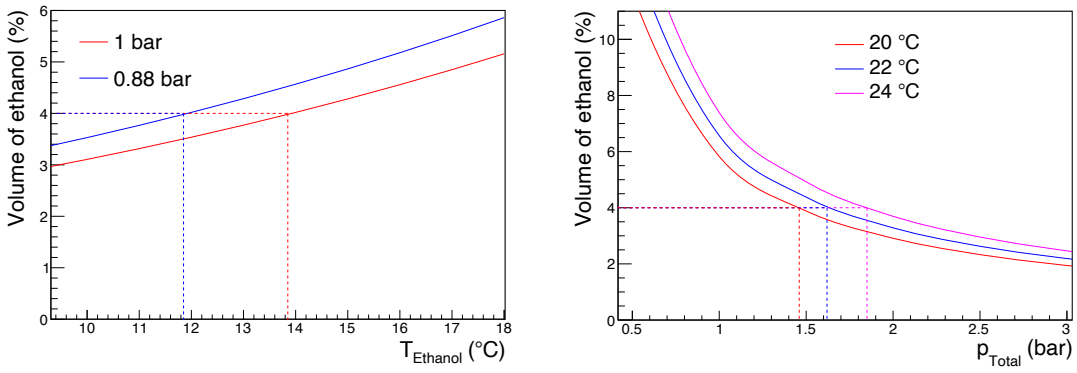

(a) Temperature Dependence **(b)** Pressure Dependence

Figure 7.2: (a) Dependence of ethanol volume on temperature. Dashed lines show the temperatures for a nominal 4% ethanol. The red line shows the pressure at sea level, and blue is the pressure underground at the laboratory. (b) Dependence of the ethanol fractional volume on the total pressure of the gas in the BP. Dashed lines show the desired pressures for a 4% level. Three different ambient temperatures are plotted. Both of the above are plotted by combining Equation (7.2) and Equation (7.1), with parameters from [116].

The temperature of the FG is precisely maintained, inside a water bath, with a Haake DL30 heater [117] and Haake EK90 chiller [118]. Previously, a Haake EK20 was used to chill the water bath. This unit had no temperature sensor and therefore cooled continuously. The DL30 has an inbuilt sensor programmable set point. During normal operation the heater acts to maintain a temperature of 14 °C, by switching on periodically. A low level of water in the bath causes the heater to switch off. In the event of the heater failing, the EK20 continues to cool

the water. This failure mode was tested at MSSL to see if the chiller could freeze all of the water in the bath (§7.5.2).

Monitoring FG temperature and BP pressure is essential for maintaining the correct ethanol concentration. Initially, the pressure was set and monitored on a back pressure regulator installed after the BP. This was adequate for testing but needed to be more precise. The temperature of the FG is monitored by a sensor in the DL30 unit and can be readout through a serial RS232 [119] connection.

7.3 System Requirements

The SuperNEMO gas system includes multiple sensor devices. Temperatures of the BP and FG are measured using PT-100 Resistance Temperature Detectors (RTDs). In the current configuration there are two probes in the FG for ethanol level measurements, as discussed later, and one in the BP. Each probe connects to a West Control Solutions P8010 panel process indicator. Flow rates for helium and argon are controlled by a MKS PR4000B-F unit. A pressure probe was added to the BP and readout with a Keller EV94 digital indicator.

If a fault occurs in the system, it is essential that we know immediately. Therefore each of the above devices must be continuously readout and monitored. Equally, it is not always possible for a technician to be present to observe a fault in the gas system. Remote monitoring is thus vital. To maintain the required 4% ethanol fraction, the pressures and temperatures in the system must be kept at nominal values. Thresholds should be set, such that an alert is issued if the values exceed or drop below this level. A continuous steady flow rate of gas is important, with a minimal switchover time when replacing gas cylinders. If there is no flow to the tracker the over-pressure will fall, reducing the effectiveness of keeping contaminants out. Furthermore, without volume replacements, radon deposition could build up. The system needs send an alert when the gas flow reduces. This gives engineers an early warning that the gas supply needs changing.

Another consumable that needs monitoring is the ethanol level in the BP and FG. The original BP recycled from NEMO-3 had a glass window to directly observe the ethanol level. However, this bubbler was suspected to emanate too much

^{222}Rn into the gas. A new bubbler was constructed with the potentially contaminated glass removed. It was therefore necessary to find a new method to measure the ethanol level. This will be discussed later in this chapter. Similarly, any instruments used to measure the liquid level in the FG must not introduce radon.

7.4 Additional Hardware

All probes in the gas system can be monitored locally by looking at the attached displays. The PR4000B-F unit displays gas flow rate information. To allow for the required remote control and monitoring, all of these instruments needed to be readout by a main control system. Figure 7.3 shows connections from each gas system instrument to the main control.

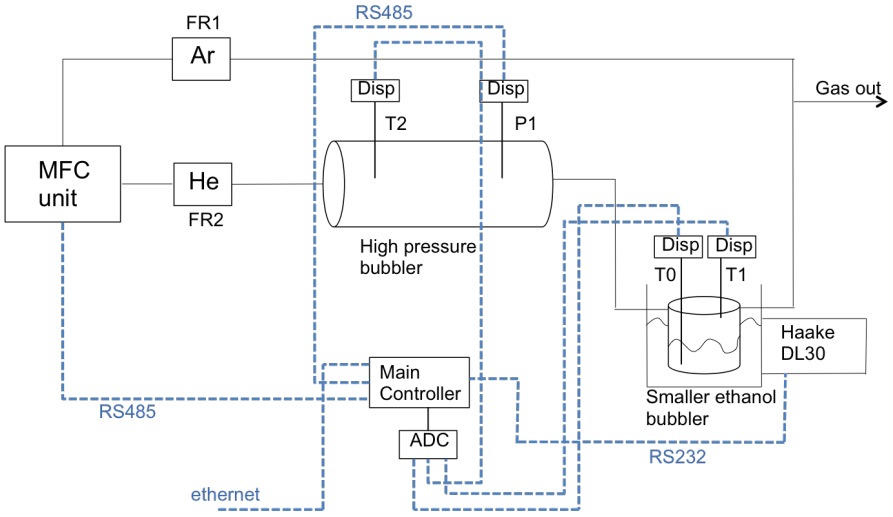

Figure 7.3: Schematic showing the connections between the sensors in the gas system and the readout computer. Dashed lines represent wired connections added to the gas system setup. FR1 and FR2 are the individual MFCs for helium and argon. These are connected to a main PR4000B-F MFC unit. T0, T1 and T2 are all RTDs connected to West P8010 displays. P1 is a pressure probe connected to a EV94 display unit. The PR4000B-F and EV94 are readout using a RS485 serial connection. The Haake DL30 unit is readout with a RS232 connection. All west displays are converted to a digital signal using an Analogue-Digital Converter (ADC).

P1 is the BP pressure probe. T0, T1 and T2 are the temperature probes. FR1 and FR2 are the individual MFCs used to control the flow rates of helium and

argon. Data can be transferred from the MFC unit and pressure display using a RS485 serial connection. A RS232 serial cable is required for readout of the Haake DL30 unit. The temperature probe displays must first be connected to a Analogue-Digital Converter (ADC) before the main controller can interpret the data. Remote access to the main controller is achieved using an ethernet connection to the LSM network. It follows that the main controller must be able to connect to serial devices as well as to an ADC. It also had to be compact, adaptable and detachable for easy movement of the system to the LSM.

A Raspberry-Pi 2 Model B [120] was chosen as the main controller for its low cost, versatility, small size and ease of use. A Raspberry-Pi is a high performance single board computer. It runs a Linux based operating system called Raspbian. The Model B has four USB, one HDMI, an ethernet port, and a I^2C bus (Figure 7.4). This allows multiple devices to be connected and readout. Programming on the Raspberry-Pi can be done quickly using the Python language. A SD card is used as the hard drive on the Raspberry-Pi. Repeat read/writes on the card can lead to corruption and the loss of data. To prevent this measures can be taken to limit the number of read/writes, such as booting the system from a USB hard drive.

Figure 7.4: Photo of the Raspberry-Pi 2 Model B [120].

7.4.1 Testing the Readout Chain

Initial tests of the readout chain from the RTDs to the Raspberry-Pi were performed to check the suitability of the device. Serial connections from the Haake

DL30 and EV94 used standard RS485 and RS232 cables. A bespoke readout chain was made to relay data from the temperature probes to the Raspberry-Pi (Figure 7.5).

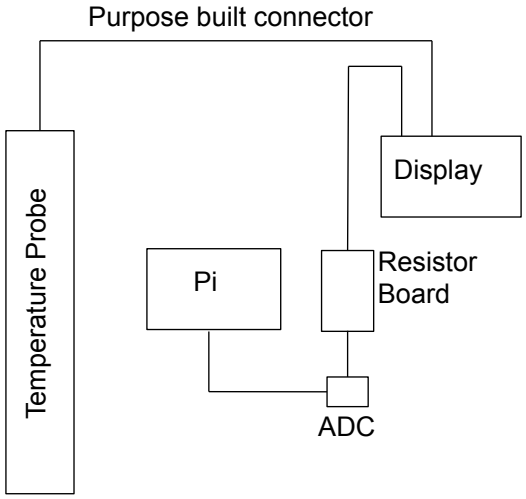

Figure 7.5: Setup of readout chain for data transfer from the RTD to the Raspberry-Pi.

The cable from the temperature probe to the West P8010 display was purpose made. The West P8010 display has an analogue readout pin for electronic readout. Before the analog signal is converted by the ADC, the output from the display first passes through an ≈ 10 kΩ voltage divider circuit. This reduces the voltage from 10 V to 4 V, which is within the safe range for the ADC. Power is supplied to the converter by the I^2C bus. The bus also receives the output signal from the ADC. Linearity checks and initial calibrations of the probe were performed using the above setup. Data was successfully readout by the Raspberry-Pi.

This setup was then used to perform an initial calibration of the temperature probe. The probe was submerged in ice water and the temperature recorded at regular intervals from the display. The ADC output was plotted against the temperature to find the gradient and intercept for calibration (see Figure: 7.6).

Uncertainty in the temperature is from the limited precision on the WEST display. A first order polynomial has been fitted with intercept $= (7.50 \pm 0.01) \times 10^{-1}$ V/°C, and slope $= (5.9 \pm 0.2) \times 10^{-2}$ V/°C. The error bounds here were found by fitting the line to subsets of the data and comparing the results. These calibration constants were then used in the python script to convert the ADC voltage

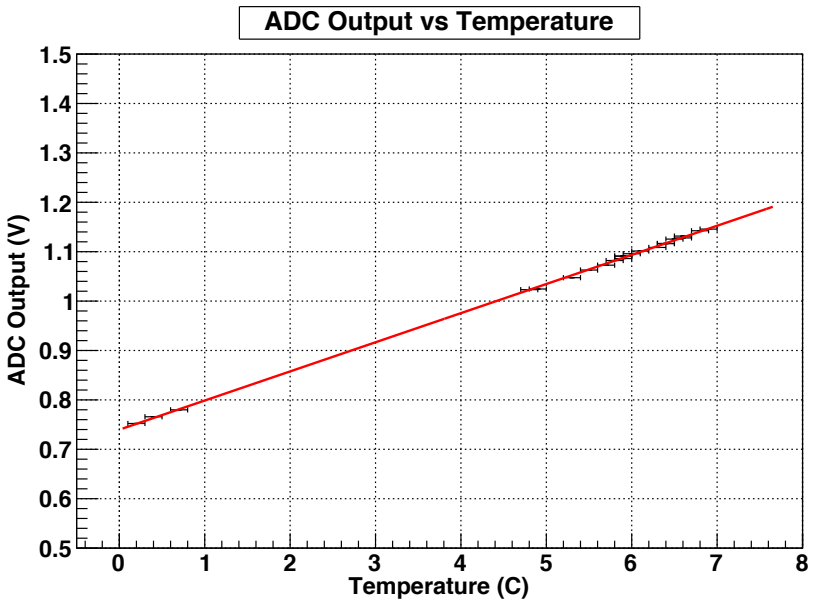

Figure 7.6: ADC output vs temperature during ice water tests.

to a temperature. Earlier calibrations in the range of 25-45 °C found compatible constants.

7.4.2 Electronics Crate

It was necessary to build a crate to house all of the readout electronics. This included three West P8010 displays, a EV94 digital indicator, an ADC, Raspberry-Pi, resistor board and feedthrough ports. Requirements of the container were that it must fit within the existing gas system rig. It must also be detachable and transportable. Figure 7.7 shows the designs for all three panels of the electronics crate.

Figure 7.7a includes a Raspberry-Pi slot for easy access to the SD card. It also has two small holes to observe the lights on the device. Two power switches were added to independently switch off the Raspberry-Pi (for rebooting), or the displays. The right-hand side of the crate (Figure 7.7b) includes all of the feedthrough connections for the probes. USB ports are for serial connections and control of the Raspberry-Pi with a key board and mouse. An HDMI is included so that a display can be added to the system.

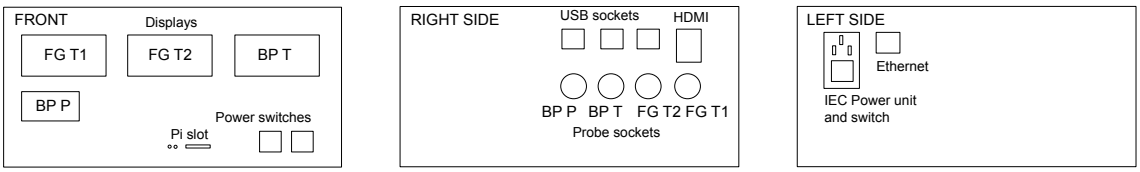

(a) Crate Front Panel **(b)** Crate Right Hand Panel **(c)** Crate Left Hand Panel

Figure 7.7: (a) Design schematic for the front panel of the electronics crate. FG T1/T2 refers to the two temperature probes in the FG. BP P/T are the pressure and temperatures in the BP. (b) Layout for the right hand side of the crate. Including all the necessary feed through ports for connections to probes. (c) Left hand panel of the crate showing the locations of the power and ethernet connections.

Having successfully tested the readout chain and resistor board for one RTD, it was adapted to have three individual resistor circuits. Power supplies from the NEMO-3 experiment were recycled for use with the EV94 and pressure probe. New cables were made for connection from probes to the displays and power. To enclose all of the above, a 19″ ventilated rack mount case was cut to match the design shown in Figure 7.7.

The readout devices were connected to the electronics crate as shown in Figure 7.8. The cables from the West P8010 displays to the ADC are not pictured. See Figure 7.3 for these connections. Serial connections from the DL30 and MFC use a USB adaptor. The serial readout from the EV94 is also by USB, directly in to the Raspberry-Pi. Crate power is distributed to each of the temperature displays and to a mounted socket, used by the Raspberry-Pi. The 'Old NEMO-3 PS' is a power supply that delivers standard voltages, e.g. 12 V to the crate devices. Again this is not shown on the diagram. All of the temperature and pressure probes were plugged in to the crate, along with serial connections to the DL30 and PR4000B-F MFC. The crate was then installed in to the existing gas system rig (Figure 7.9).

The modular set up of the electronics crate allows for easy disconnection of devices ready for transport. To increase the number of sensors that can be added, a USB hub was attached. Additional space inside the crate and on the resistor board can be used to accommodate further readout electronics. Therefore, overall the system is adaptable.

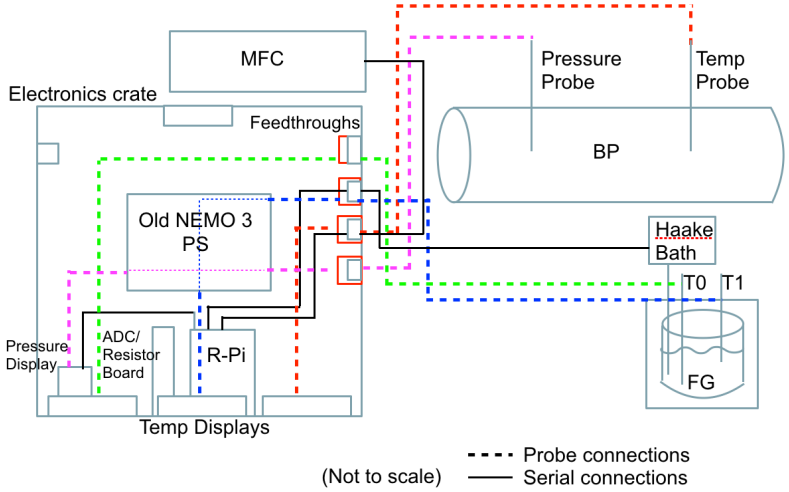

Figure 7.8: Connections from gas system sensors to the electronics crate. Dashed lines represent probe connections, solid lines are serial connections. The crate diagram shows the approximate position of all of the internal electronics and cables. Where PS is Power Supply.

Figure 7.9: Photo of the final crate location, at the top left of the gas system rig, with the PR4000B-F MFC secured on top.

Whilst the development of a readout system using a Raspberry-Pi makes remote monitoring possible, it does not provide data logging to a user on site. An engineer can observe current values on the individual displays but not long term data. To improve the ease of use of the system a monitor was added to the setup. Fluctuations of variables such as the flow rate, temperature and pressure could then be viewed in situ. Providing this information, in a clear and easy to interpret way, should help engineers debug problems in the gas system. A Graphical User Interface (GUI) was developed to display plots of the key variables. The details of this will be discussed in §7.5.1. To control the GUI a keyboard with in built trackpad was installed.

Monitoring data from the PR4000B-F MFC provides information on the gas flow rate. However, it is not possible to remotely verify the gas system configuration. This includes the position of manually operated valves (such as those in Figure 7.1). It is important to implement this, as it allows an offsite expert to check the gas system is in a safe state before changes are made. A second Raspberry-Pi was set up with a camera module attached. The proximity of the camera to the gas rig results a small field of view. Therefore, it needed to be possible to pan and tilt the camera. This was achieved by using a Pimoroni Pan-Tilt Hardware Attached on Top (HAT) module (Figure 7.10).

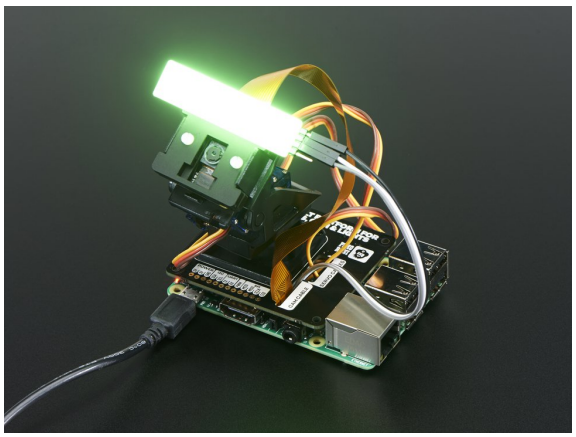

Figure 7.10: Photo of the Pimoroni Pan-Tilt HAT attached to a Raspberry-Pi, with a NeoPixel LED bar [121].

Installation is complete and it is now possible to move the camera to view each valve location to check its status. With further development the process could be

automated to complete scans regularly. This could involve basic image processing to determine the valve position and log it.

7.5 Slow Control & Monitoring

The SuperNEMO CMS is a standalone software required for continuous monitoring of key variables in the experiment. It acts as an interface between the VIRtual Experiment (VIRE) and hardware, where VIRE is an experiment manager that defines users, roles and sessions, which allows resources to be shared simultaneously. The framework for the SuperNEMO software is shown in Figure 7.11, where the Multipurpose Open Platform Communications Unified Architecture (OPCUA) Server (MOS) is an application that manages the hardware using a software interface [122]. The OPCUA is a cross machine communication protocol, which allows access to historical or real time data.

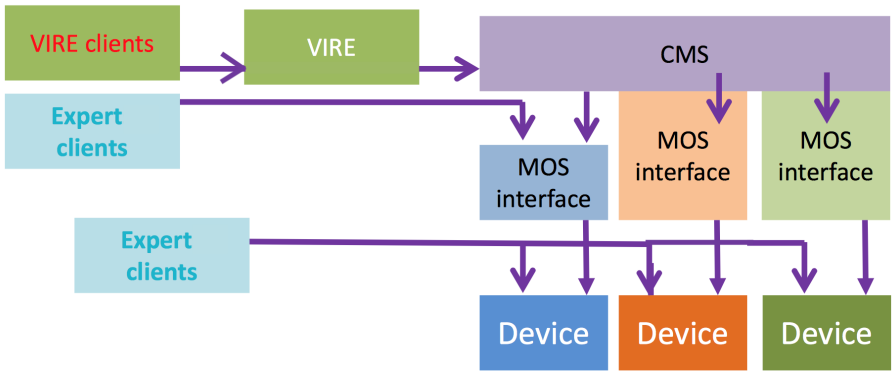

Figure 7.11: Workflow of the CMS showing its connections to the VIRE and hardware devices using a MOS [123].

Expert clients are included in the workflow for control/monitoring of devices during commissioning and debugging. They can have access points directly to the device or through the MOS interface. The VIRE client is now being used by shifters during comissioning of the experiment. To integrate a new device in the CMS, a MOS must be installed. The server was installed on to the gas system Raspberry-Pi, along with an expert client for debugging purposes.

Incorporating the gas system into CMS allows for long term monitoring and control of the setup. It means that a shifter can easily check the status of the equip-

ment, as will be the case for other key systems in the SuperNEMO experiment. All of the gas system variables to integrate with the CMS are listed in Table 7.1. The labels listed are those used by the MOS and displayed in the client.

Physical Quantity	Component	Label	Readout
Set Point Ch. 1/2	Flow Control	SP1/SP2	RS485
Flow Rate Ch. 1/2	Flow Control	FR1/FR2	RS485
Range Ch. 1/2	Flow Control	R1/R2	RS485
Scale Ch. 2	Flow Control	SC2	RS485
Status Ch. 2	Flow Control	ST2	RS485
Temperature 1	FG	T0	ADC Ch. 0
Temperature 2	FG	T1	ADC Ch. 1
Temperature 3	BP	T2	ADC Ch. 2
Pressure	BP	P	RS485
Ambient Pressure	Environment	P1	USB
Sensor Temperature	Haake	T	RS232
Set Point Temperature	Haake	S0	RS232
Operating Status	Haake	Operating Status	RS232
Temperature High/Low Limit	Haake	HL/LL	RS232

Table 7.1: Monitoring variables, associated gas system component, their labels and readout methods

The server takes the device input/output and transforms them in to standardised data points. A MOS is configured using an Extensible Markup Language (XML) file. This file is used to define the devices and datapoints associated to the system. In this use case, a 'Simple Device' is defined as the 'Gas System'. The variables listed in Table 7.1 are each defined as a 'Simple Datapoint'. For each datapoint a method is listed to get/set its value. It is also possible to cache the history of the variable, set a monitoring rate, and define conditions for alarms to be triggered. Instructions for the get/set methods give the paths to the readout scripts. This allows the MOS to retrieve the datapoint values from the gas system hardware. The OPCUA client namespace of methods and variables is populated by XML. Figure 7.12 depicts the structure of the client-server setup and the information flow.

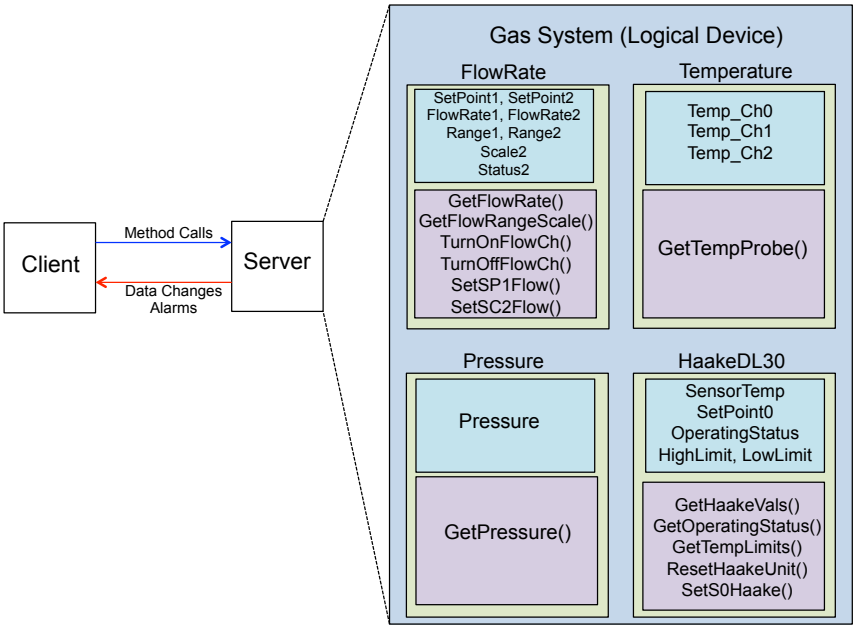

Figure 7.12: Workflow of the client-server setup, showing the data points, variables and methods as defined in the XML. The 'Simple Device' is shown in dark blue, 'Compound Datapoint' in green, 'Simple Datapoint' in light blue and methods in purple.

To communicate with the Raspberry-Pi it is necessary to include a plugin. This takes the data outputted from the device scripts and interprets it for the MOS. A pre-existing shell plugin was used, which is loaded on startup of the server. An example of the information flow from the method call to the gas system hardware is shown in Figure 7.13. The 'Server' as shown in Figure 7.12 is represented by the two example method call boxes shown in Figure 7.13.

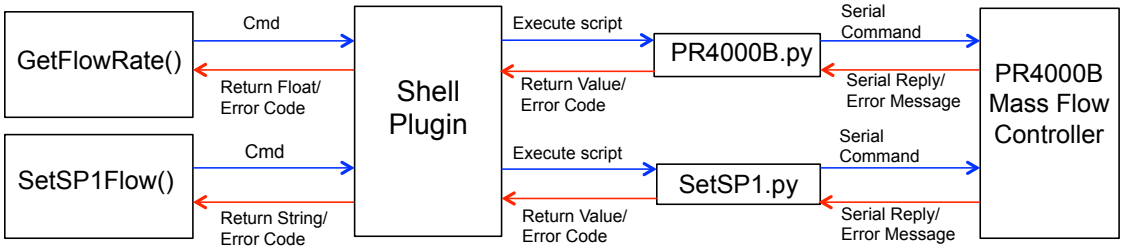

Figure 7.13: Flow of data from two example method calls on the MOS to the PR4000B-F MFC unit. Blue and red arrows show the input/output types each stage of the process.

The plugin takes the command from the MOS and converts it into a shell instruction to run the appropriate Python script. Detail of readout from the hardware

devices using Python will be discussed in §7.5.1. The plugin also does the conversion of the value returned from the script.

7.5.1 Software

As mentioned in §7.5 and illustrated in Figure 7.11 an expert client can be installed to debug the system. For this purpose a ProSys OPCUA client [124] was installed on a local computer. The client provides a GUI for setting/getting values. It also allows the user to monitor values and view historical data in tabular or graphical format. The client was used extensively for testing both the server and gas system setups. This will be detailed in §7.5.2.

Python is the official programming language of the Raspberry-Pi. Version 2.7 was used for all of the readout scripts. As shown in Figure 7.5 all of the RTDs probes are connected to a West P8010 display. An ADC performs the conversion from analogue to digital. Communication with the ADC was achieved using the Adafruit_ADS1x15 Python library, available at [125]. Time stamps were added to the output from the Python scripts. Readout from serial devices involved the use of basic serial commands. These commands are given for the EV94 pressure display, Haake DL30 and PR4000B-F in [126], [117], and [113] respectively. In the event of a failed serial connection, an error message is printed. All of the code created for the gas system is stored on the SuperNEMO Subversion (SVN) at Caen. This allows for software versioning and revision control.

Some modifications to the Python scripts were required to make the outputs compatible with the client and server. The original verbose outputs with a timestamp caused timeouts. This is where the client reaches a time limit whilst receiving or transmitting data. To overcome this, all the scripts were edited to take input arguments. Users can pass ‘d’ (default) for the verbose output, or ‘0’ to return a single value only. This second option is for use with the client. For scripts with multiple variable readout, such as the for the PR4000B-F unit, one variable can be requested (FR1, FR2 etc.) These changes ensure that the time for the client to receive the value is as short as possible. It is also essential that the server runs continuously to preserve the long term history of the data. A simple shell script checks to see if the process is running. If it is not then the server is restarted. The

watchdog script is executed continuously by a Cron job [127] on the Raspberry-Pi. Cron software allows users to time-schedule commands or shell scripts.

Detailed error reporting is provided when 'd' is passed to the script. It is not possible to send all of this information to the client as it causes time-outs. Instead, an error event is triggered which can then be investigated by an expert at script level. Error/alarm event thresholds can be set in the server configuration XML. The Python scripts were then edited to output this error value when serial connections fail or the ADC cannot be readout. An Interface Control Document (ICD) details all of the data points, methods and events involved in the system. It describes the data exchange interface between the gas subsystem and the SuperNEMO CMS. For each Python script, action points are specified if an error occurs.

As mentioned in §7.4.2, a GUI was designed to assist onsite engineers with debugging the system. This was produced using Python, Matplotlib (a 2D plotting library), and TkInter (a graphical package for Python). The basic requirements for the interface were that it should be easy to operate, allow quick checking of the system status, and include live plotting of the key gas system variables. Figure 7.14 shows the main page of the gas system GUI.

On the main page the variables shown are the BP pressure, the temperatures in the BP/FG, flow rates of the gases and the temperature of the thermal bath from the DL30 unit sensor. All of the plots show values from the last two hours and update live. The graphs can be viewed individually by selecting them in the 'Variable' drop-down menu. The 'System status' box uses the output from the overall status script and sets the colour using a traffic light schema. It is possible to pause/resume the live plotting. This is useful for saving off the plots, zooming, or repositioning plots with the TkInter built in toolbar. The drop-down menu includes a tab for 'Ethanol level measurement', discussed in §7.5.2.

A key requirement for the GUI was that it was easy for on site engineers to operate. As the experiment is based in France, it was requested that the interface be displayed in French. This was done by creating a configuration file and look up table to swap between French and English. The finished GUI is shown on a monitor attached to the gas system rig.

For the early stages of testing an overall status script was written. This calls each of the Python scripts in turn and prints the output to the command line. It also

Figure 7.14: GUI for in situ monitoring of key variables in the gas system. In the bottom left corner is the built in TkInter toolbar for saving and editing plots. The bottom left plot shows no flow rate as the gas was not flowing at the time.

displays the most recent results on a light webpage, providing a fast method for checking the system status.

7.5.2 Applications

The software and information flow were tested thoroughly whilst the gas system was located at MSSL. The server-client setup was helpful for commissioning of the tracker sections, and monitoring conditions in the laboratory. Several of the applications are detailed in the following sections.

EK20 Failure Mode

As previously mentioned, in the event of the heater unit failing, the EK20 continues to cool the water bath. It is important to understand the time scales of the failure mode. This gives an indication as to whether the system can be left for several days, or if urgent action is required. Operationally, it is a requirement that the system can be left for three days without the need for any manual intervention. In the first test the DL30 heater was disabled and the EK20 allowed to cool the water down to 0.8 °C. The water in the bath was continuously monitored watching for the formation of ice around the cooling element. Cooling from 14 °C to 0.8 °C took ≈ 4.5 h, with ice beginning to form around the cooling element at ≈ 2 °C (Figure 7.15).

During this test, the server was running on the Raspberry-Pi, recording the temperature readouts from the DL30 sensor and the RTD probe in the FG. The results were saved and Figure 7.17 shows the plot displayed on the ProSys OPCUA client. A reminder of the setup of the water bath, DL30 heater, Haake EK20 chiller and temperature probes is shown below in Figure 7.16.

The client allows historical data to be viewed for one or more variables. In this case, the temperature recorded by the DL30 sensor in the water bath (red line), and the temperature from the RTD probe inside the FG (blue line). There is an ≈ 0.25 °C offset between the two sensors. This is a result of the different calibrations of the hardware. As the RTD is inside the FG, there is a different response c.f. the change measured by the DL30 sensor in the water bath. Figure 7.17 shows

Figure 7.15: Ice forming on the cooling element of the EK20 unit at a temperature of $\approx 2\ ^{\circ}\mathrm{C}$.

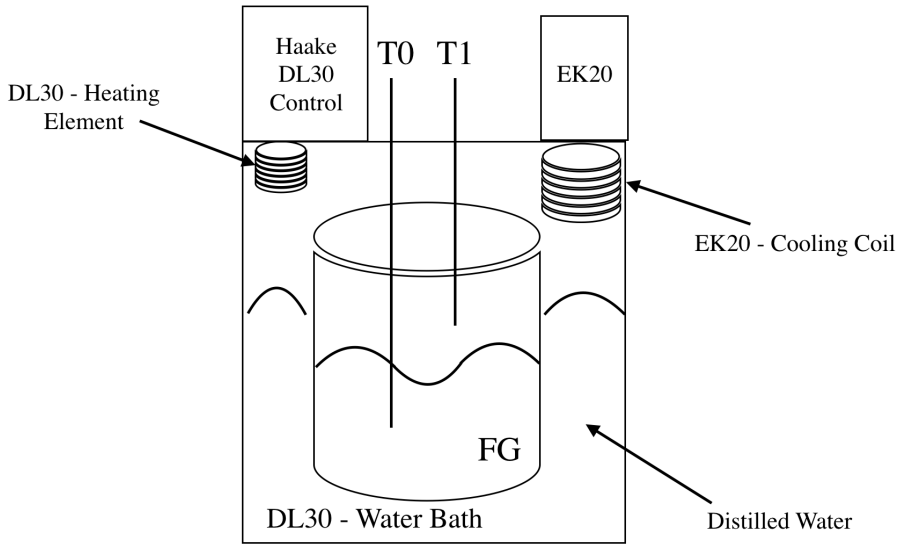

Figure 7.16: Diagram of the setup of the Haake DL30 thermal water bath, with the EK20 cooling coil and temperature probes T0 and T1. The DL30 sensor records the temperature in the water bath

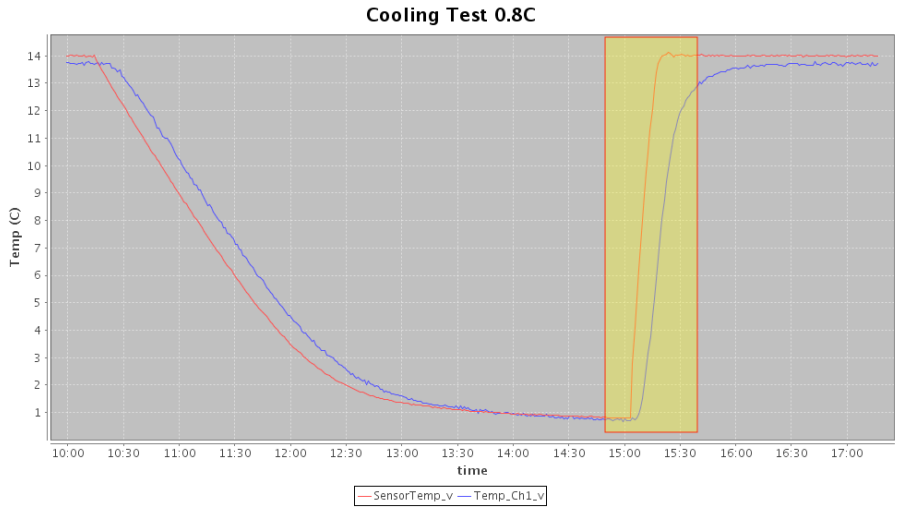

Figure 7.17: Graphical display from the ProSys OPCUA client, showing the temperature from the DL30 sensor (red) in the water bath, and the RTD in the FG (blue).

the temperature gradients cooling from 14 °C to 0.8 °C over ≈ 4.5 h, and then reheating to 14 °C in ≈ 15 min. To check the effect of the ice build up on the temperature gradient another test was performed cooling to 5 °C and reheating to 14 °C (not shown). For both scenarios an approximate gradient of 0.8 °C/ min was calculated for the reheating section (see highlighted example in Figure 7.17). Therefore, if ice forms in the water bath, the nominal temperature can be recovered quickly. However, for both of these tests the pump in the bath was still circulating the water. When the water bath level drops below threshold, the pump will also stop. Another test was performed to monitor the water bath with both the heater and pump off on the DL30.

Due to the lack of circulation in the bath, ice formed around the cooling element at 13 °C. The existing ice then acted as an insulator, slowing down the cooling process. Unlike the previous test, the temperature did not fall below 6 °C. It is possible that the temperature was lower close to the cooling element. This is certainly the case if ice is present. With the DL30 heater and pump reactivated the temperature rose to 14 °C in ≈ 15 min. With the pump off, the system was stable over a period of ≈ 4 h. The test was not performed over several days, so the long term effects of a deactivated DL30 unit are unknown. Given the requirement of a system that must be able to be left for three days without manual intervention, it was decided to replace the EK20 chiller with a more advanced unit.

An alternative Haake EK90 chiller was available with an independent temperature sensor. Unlike the EK20, a set point can be configured so that the chiller only cools to a nominal temperature. In the event of the DL30 failing, the EK90 could maintain the bath at a fixed set point. Testing the EK90 involved switching off the DL30 and using a set point of 6.5 °C. Temperatures were monitored as before, using the client. Initially there was a regular oscillation between ≈ 4.4 and 5.8 °C. This could have been cause by the chiller continuously stopping and starting. The data recorded by the client can be seen in Figure 7.18.

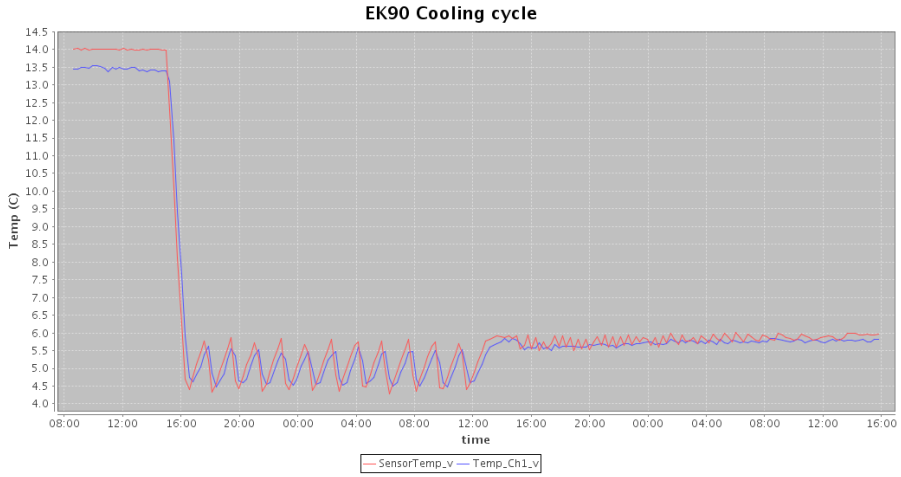

Figure 7.18: Graphical display from the ProSys OPCUA client, showing the temperature from the DL30 sensor (red) in the water bath, and the RTD in the FG (blue). Shows the oscillations in temperature during EK90 chiller testing.

Oscillations in temperature occurred for ≈ 20 h before the temperature stabilised at ≈ 6 °C. The client was then used to check the unit continued to function as expected. The offset between the set point and measured temperature is most likely due to a mis-calibration of the EK90 temperature sensor. Running the DL30 alongside the EK90 gave a stable temperature, and the EK20 was replaced.

This was a good test of the client-server technology and data flow. Values were successfully readout from the RTD probe and the serial DL30 unit. The server requested and transmitted the data to the client, with successful monitoring over a four day period (Figure 7.18). Data was also saved in raw format, allowing for further analysis if necessary.

A limitation of the server was the maximum buffer size. Historical data stored by the server was the last 1000 values recorded. Depending on the monitoring rate of the datapoint the time period you could view changed. It was requested that this buffer size be configurable, and the change was implemented in MOS version 4.0.1. CMS will incorporate automatic archiving of old data. However, it was helpful for debugging purpose to have long term data logging during commissioning.

Ambient Pressure Monitoring

As mentioned in §7.1, passing heavy road vehicles can cause pressure fluctuations at the LSM. If this variation is faster than the gas flow through the detector can counteract, it leads to potentially damaging under/over pressures. To check the amplitude of ambient pressure fluctuations in the laboratory, a barometric pressure USB data logger (Model B1100-1) was installed on the gas system Figure 7.19.

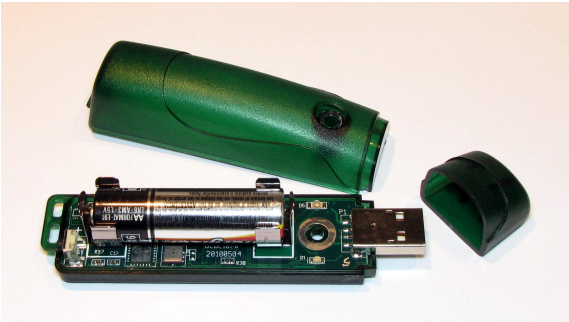

Figure 7.19: Image of a barometric pressure USB data logger, used to monitor the ambient pressure in the clean room at the LSM.

A maximum tolerated pressure fluctuation was estimated for the full SuperNEMO demonstrator, using Boyle's law:

$$PV = k, \tag{7.3}$$

where P is the pressure, V the volume and k a constant for an ideal gas in a closed system. This assumes a constant temperature and overall amount of gas. The product rule was applied to find:

$$\left|\frac{dP}{dt}\right| = \frac{P}{V}\frac{dV}{dt}, \tag{7.4}$$

where t is the time. These pressure fluctuations were calculated considering a gas flow ($\frac{dV}{dt}$) of 1 m^3/h, P= 0.88 bar, and V = 15.2 m^3:

$$\left|\frac{dP}{dt}\right| = \frac{0.88}{15.2} \times 1 \tag{7.5}$$

This is equivalent to 5.8 $\times$ 10^{-2} bar/h, which is 0.96 mbar /min. It was considered that anything above this level could be damaging to the detector. Pressure readings were recorded over a four hour period during two weekdays and plotted. Figure 7.20 shows an example four hour recording on the 7th of June in 2017. The gradient has been found for one of the larger pressure fluctuations, as -1.054 $\pm$ 0.083 mbar/min.

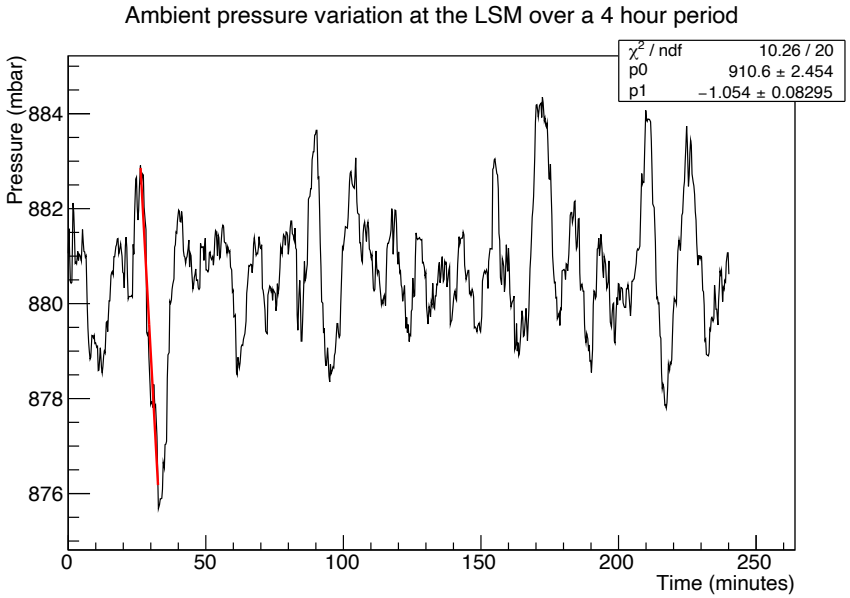

Figure 7.20: Ambient pressure fluctuations over a four hour period on the 7th of June 2017. Gradient shown in red is for one of the larger fluctuations

Figure 7.21 shows another four hour window recorded on the 8th of June 2017. Several large fluctuations can be seen in this plot. One of which has been taken as an example with the gradient found as 1.071 $\pm$ 0.050 mbar/min.

All of the larger gradients were measured in this way for the two days of recording, with all of them being $\approx$ 1 mbar/min. These fluctuations were most likely due to traffic through the adjacent tunnel, and were not considered as dangerous to

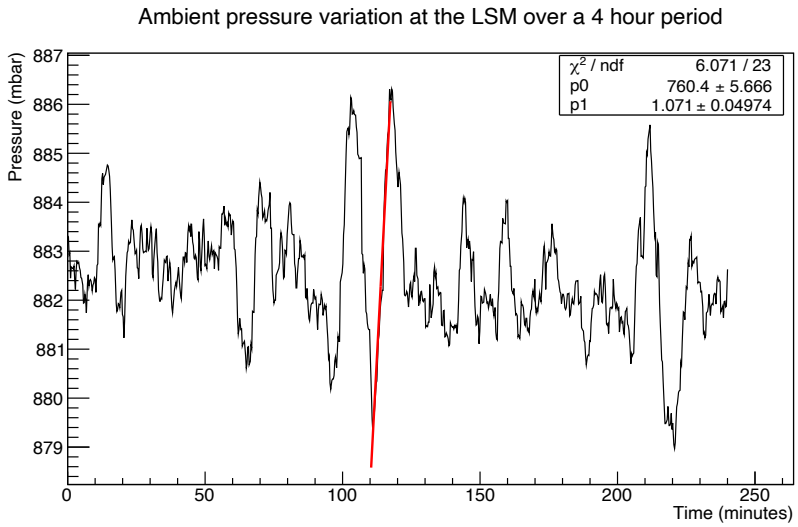

Figure 7.21: Ambient pressure fluctuations over a four hour period on the 8th of June 2017. Gradient shown in red is for one of the larger fluctuations

the detector. As part of this initial test of the ambient pressure device, data was taken for a period of 6 days, with results shown in Figure 7.22

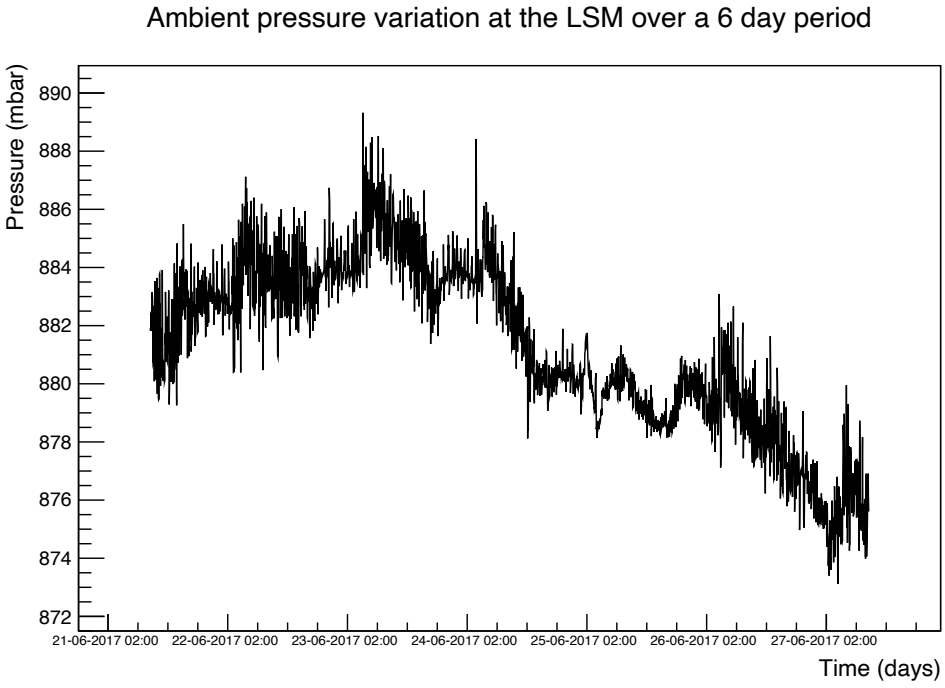

Figure 7.22: Ambient pressure fluctuations at the LSM over a 6 day period in June 2017.

On closer inspection, the fluctuations seem to reduce from around midday on the 24th of June to midnight on the 25th of June. These results were recorded over the weekend, when traffic through the tunnel reduces. These pressures will continue to be monitored in case of changes that could result in larger fluctuations.

Ethanol Level Measurement

The BP is filled with liquid ethanol that evaporates, adding $\approx 4\%$ fraction to the helium. This is then finally tuned in the secondary bubbler. Thus it is important to monitor the ethanol level in the bubbler, to ensure the correct gas mixture is supplied to the detector. Previously, one end of the BP cylinder was made of glass, allowing easy observation of the level. However, due to stringent radon requirements the glass was replaced with stainless steel. One method for calculating the ethanol level is to use the time taken to pressurise the BP. To test this method, the pressure was monitored with ethanol present and after it was drained. Figure 7.23 shows the plots saved off from the history view in the client.

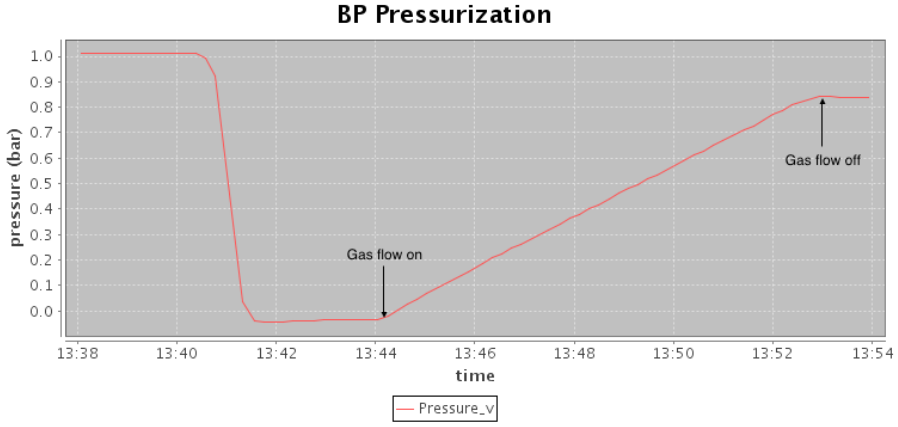

Figure 7.23: Pressurisation over time of the BP with ethanol present. Arrows indicate the times at which the flow was turned on and off

Initially the back pressure regulator on the BP was set at ≈ 0.8 *bar*, and the flow turned off. The BP was then fully depressurised using the pressure release valve. Finally, the flow rate was set at 5 ℓ/min and turned on. For all of the following tests, nitrogen was used rather than helium, due to it's availability at the MSSL. Raw data was saved off from the client and a first order polynomial fitted to the values between the gas flow being switched on and off. Figure 7.25 shows the plots

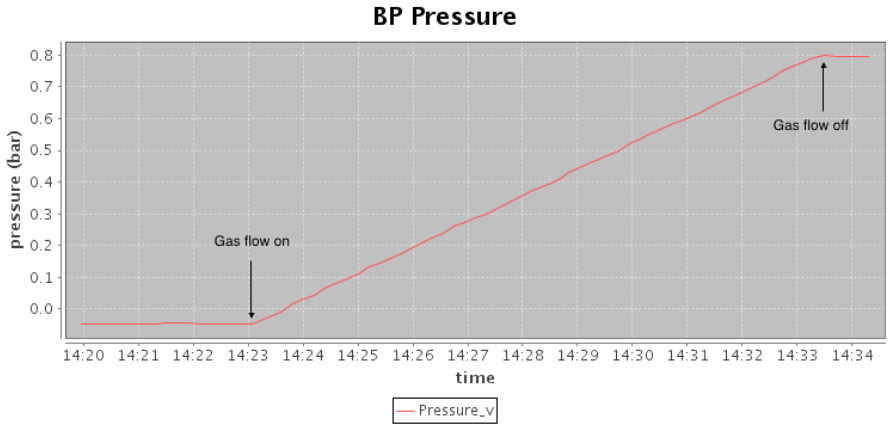

Figure 7.24: Pressurisation over time of the BP without ethanol present.

produced in root, where the error on pressure measurement have been calculated by cross checking the probe readout against the dial gauge on the back pressure regulator, resulting in a ± 2.5% uncertainty.

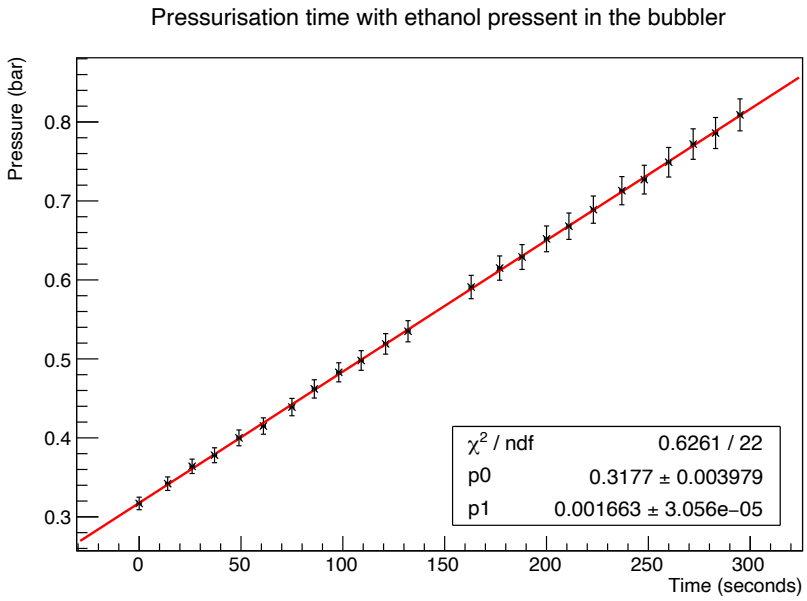

Figure 7.25: First order polynomial fitted to data recorded from pressurisation of the BP with ethanol present. Error bars on the date-time are too small to be seen.

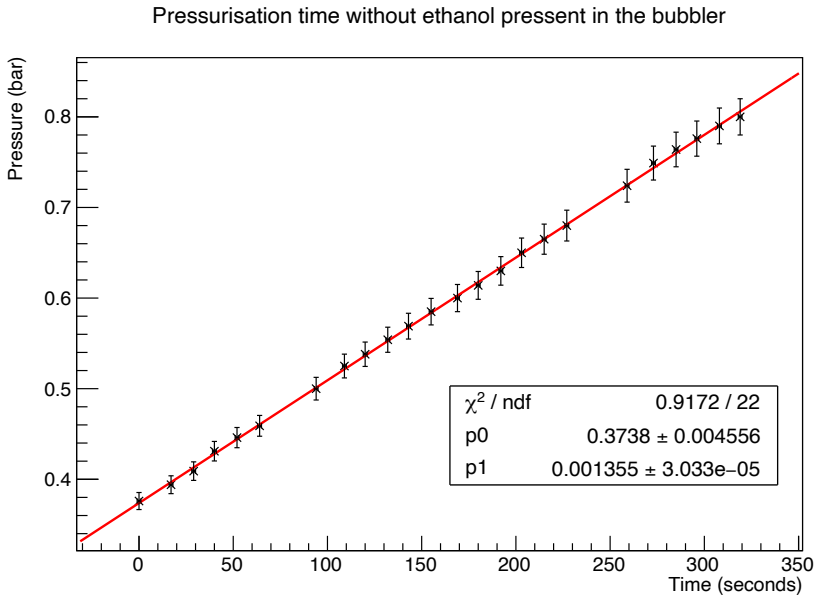

Figure 7.26: First order polynomial fitted to data recorded from pressurisation of the BP without ethanol present. Error bars on the date-time are too small to be seen.

To calculate the volume of ethanol drained from the bubbler the following formula was used :

$$\frac{\Delta P}{\Delta t} = \frac{F}{V_g}$$

where F is the flow rate, ΔP is the pressure change, Δt the time period, and V_g is the gas volume remaining in the BP. The left hand side was calculated by finding the gradient of the polynomial fitted. With the ethanol in the bubbler this was found to be $(1.66 \pm 0.03) \times 10^{-3} bar/\text{s}$. After draining the ethanol it was $(1.36 \pm 0.03) \times 10^{-3} bar/\text{s}$. Error bounds were found by fitting subsets of the data and comparing the results. Whilst the flow rate was set a 5 ℓ/min it had to be corrected by a factor of 1.4 to account for the use of nitrogen rather than helium. With a corrected flow rate of 3.57 ℓ/min $\equiv$ 0.0575 ℓ/s, an initial volume was calculated as $V_{gi} = (36 \pm 5)$ litres, and final volume $V_{gf} = (42 \pm 1)$ ℓ. Therefore $\approx$ 6 litres of ethanol were drained from the BP. The uncertainties on the gradient were calculated by propagating an error of 5% on the pressure and a 1 s uncertainty on the time readings. The uncertainty in the flow rate $\Delta F = \pm 0.005$ was

from fluctuations seen in the value. Errors were propagated from these to find the uncertainties on the gas volumes calculated.

To further simplify calculations of the volume of ethanol in the bubbler, several runs were conducted to find the conversion number from expected ethanol level to measured ethanol level. Starting from an $\approx 1\ \ell$ of ethanol, the tank was filled in stages to $\approx 6\ \ell$, $11\ \ell$, $16\ \ell$, and finally $21\ \ell$. For each stage of filling, the pressure of the bubbler over time was recorded (as in Figure 7.26). Examples of the results for the $\approx 6\ \ell$ and $11\ \ell$ results are shown in Figure 7.27. Using these plots, the measured volume of ethanol was calculated, as before, using Equation (7.6). The calculated ethanol levels were then plotted against the expected ethanol level as shown in Figure 7.28.

The errors on the gradient were found by propagating an error of 5% on the pressure and a 1 s uncertainty on the time readings. This was then propagated with the uncertainty on the flow rate of $\Delta F = \pm 0.005$ to find the errors on the x-axis of Figure 7.28. Errors in the expected ethanol volume were taken to be $\pm 0.5\ \ell$. From this plot it was then possible to extract a conversion factor of 1.266 that could be used to correct the expected ethanol level to an estimation of the actual level. A key assumption in the use of Equation (7.6) is that the temperature is constant throughout the measurement. In actuality, the temperature at the LSM can fluctuate by $\approx 2\ ^{\circ}\mathrm{C}$. There is also a dependence on the gas flow, owing to the cooling effect of the evaporating ethanol. As a result, the BP temperature probe has shown readings between 19-23 $^{\circ}\mathrm{C}$, and overpressure setting have been calculated for each of these temperatures. The calculation also assumes a known BP volume of $43\ \ell$. However, using this method it is evident that the volume of ethanol in the BP can be easily estimated in situ at the LSM.

7.5.3 Use in the Commissioning of the Demonstrator Module

Following on from its relocation to the LSM at the end of 2016, the gas system has been used to establish gas tightness, test overpressure and now commission the SuperNEMO demonstrator module. Figure 7.29 shows the gas system in po-

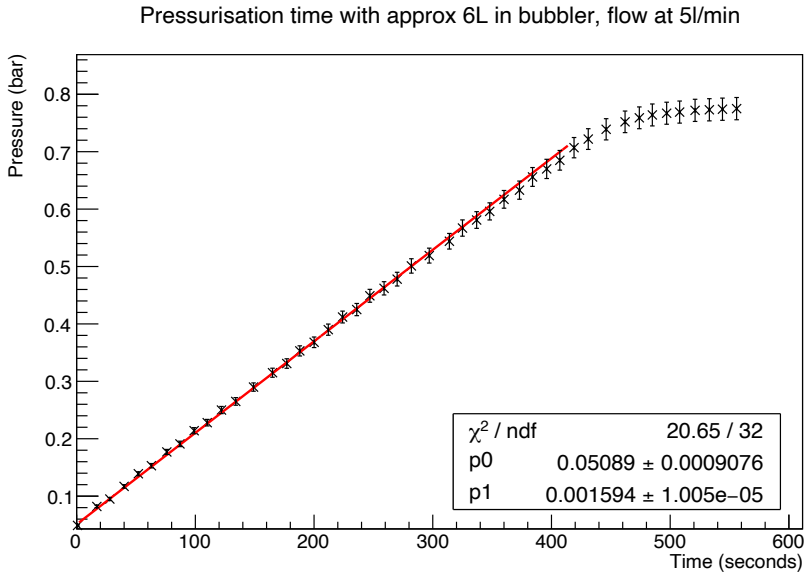

(a)

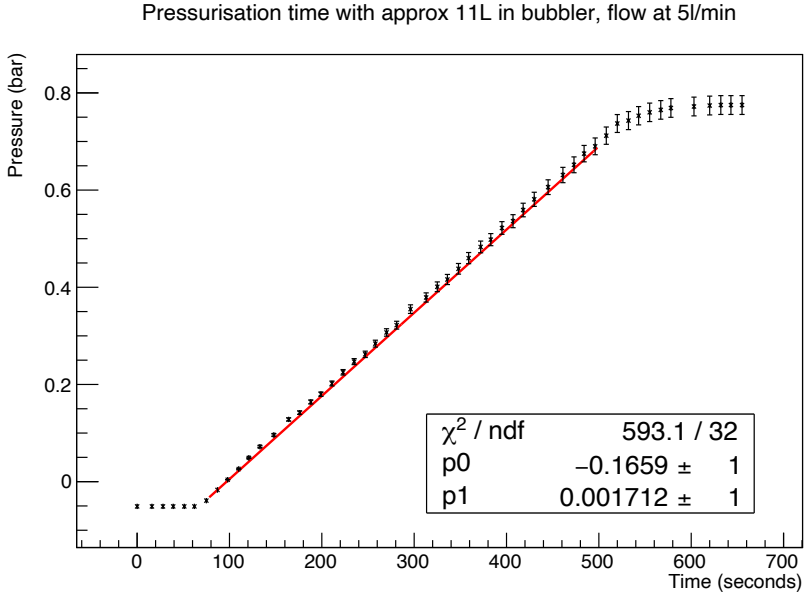

(b)

Figure 7.27: (a) Pressure over time during the filling of the ethanol bubbler to $\approx 6\ \ell$ at an expected flow rate of 5 ℓ/min, with a first order polynomial fitted. (b) Pressure over time during the filling of the ethanol bubbler to $\approx 11\ \ell$ at an expected flow rate of 5 ℓ/min, with a first order polynomial fitted.

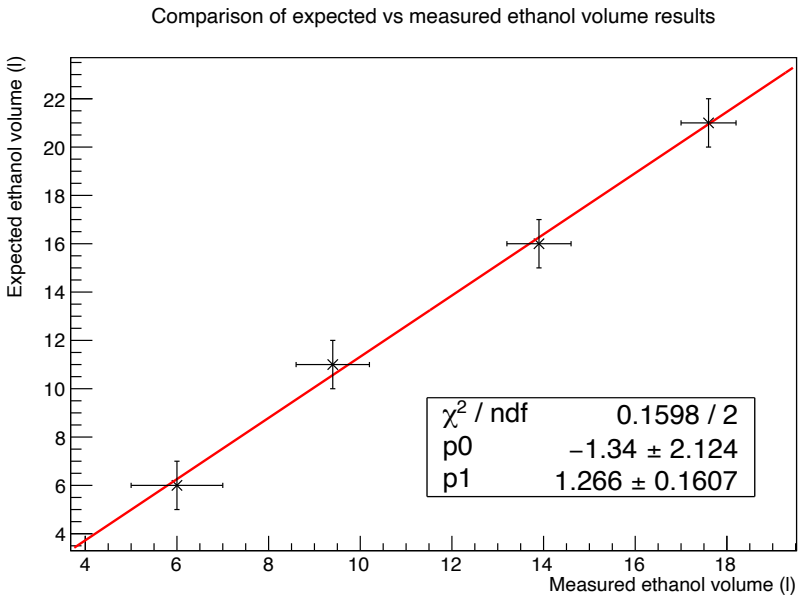

Figure 7.28: Comparison of the expected ethanol level vs the measured ethanol level

sition at the LSM with perspex surrounds to protect from dust in the laboratory environment.

Figure 7.29: Image of the gas system on location at the LSM in France.

During gas tightness tests that began in 2019, argon was supplied to the detector at a rate of between 20-40 ℓ/min. Argon sniffers were then used locate leaks in the detector. Throughout this study, all leaks found were carefully mapped in order to revisit and seal them as well as monitor how effective sealants used were. By June 2021, an overpressure of $>$ 10 mbar was achieved with a flow rate of 40 ℓ/min. Following on from continued improvement to the gas tightness, a current (at time of writing) measurable overpressure at a flow rate of $\approx$ a few ℓ/min was achieved. This was then sufficient to begin tracker commissioning. In order to do so, the gas system inputs and outputs needed to be finalised. The helium cadres were positioned and the gas supply and exhaust lines installed. A cadre is a pallet containing 9 helium cylinders, with an approximate 80 m^3 total of gas (at Standard Temperature and Pressure (STP)). Figure 7.30 illustrates the connection lines between the helium cadres, the gas system and the supply and exhaust for the detector. At the junction of the two helium cadres is a switcher, that automatically switches between cadres when one is empty. This allows for the continuous supply of helium.

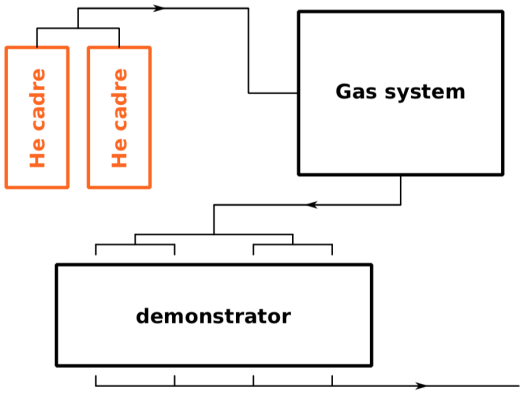

Figure 7.30: Schematic of the lines for the supply and exhaust of gases [83].

With this configuration established, the gas system was commissioned and is now able to supply the detector with the correct mixture of 95% helium, 4% argon and 1% ethanol. The feed line for the detector supplies an equalised gas distribution through 8 input points at the top of the detector. In Figure 7.31a, the blue line indicates the main supply from the gas system. Figure 7.31b is a schematic of the 8 exhaust lines at the bottom of the detector that are combined and sent to

a bubbler. Using this set up, systematic commissioning of the tracker began in September 2021.

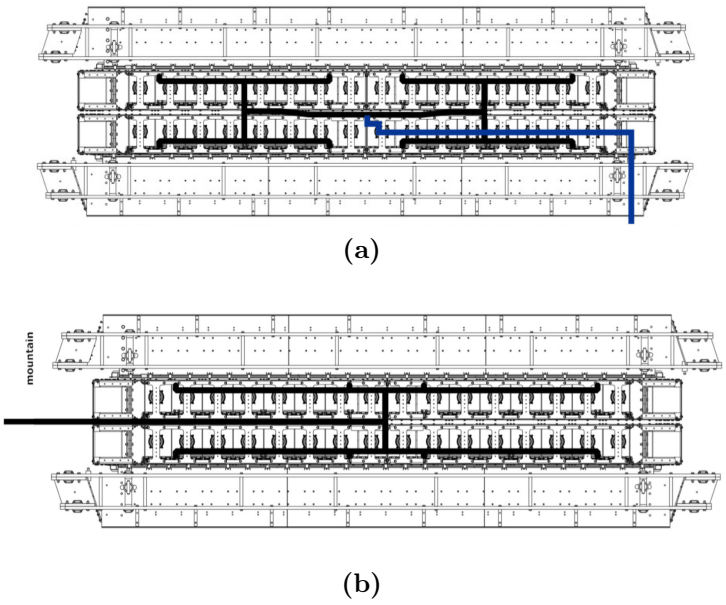

(a)

(b)

Figure 7.31: (a) Schematic showing the feed line for the detector gas supply. Blue line indicates the main supply, and the black lines the 8 input points into the tracker. (b) Schematic of the bottom of the detector indicating the 8 exhaust lines that are combined to one output feed [83].

Throughout the commissioning phase, the CMS and GUI have been used in earnest to monitor the gas system remotely and on-site (as described in §7.5). Currently, a shared spreadsheet is being used for regular gas system monitoring during use of the tracker. The BP pressure and temperature, and the FG level values are recorded over time. These are then plotted in excel to view long term variations, as shown in Figure 7.32.

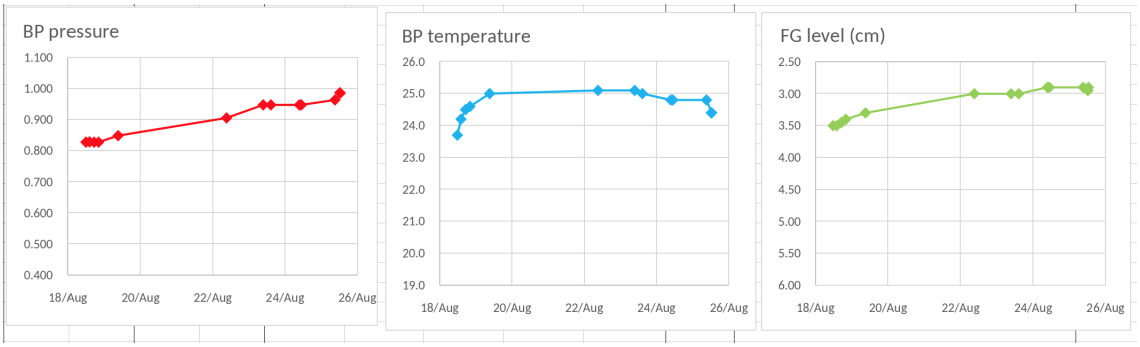

Figure 7.32: Variation over time of the BP pressure, BP temperature, and FG level for 8 days in august. All of these values were read using onsite displays and remote monitoring scripts.

Chapter 8

Conclusions

The neutrinoless double-beta ($0\nu\beta\beta$) decay process is forbidden by the SM, and is yet to be observed. It is of great scientific interest as its discovery would reveal the nature of the neutrino as a Majorana particle. In turn, if the neutrino is its own anti-particle this could help explain the matter-antimatter asymmetry in the Universe. In addition to this, the $0\nu\beta\beta$ process can be used to find the effective Majorana neutrino mass.

SuperNEMO is one of many experiments searching for this lepton number violating process. Its tracker-calorimeter design builds on its predecessor, NEMO-3, which was successful in exploring the $2\nu\beta\beta$ process for several isotopes, including ^{100}Mo and ^{82}Se. Key changes planned for SuperNEMO are to increase the source mass, improve energy resolution and, crucially, reduce backgrounds. The SuperNEMO demonstrator will test the feasibility of the new targets set. Construction of the detector at the LSM in France is now complete, with commissioning underway. Data is being taken without the final shielding present, and will be used to model background contributions.

Simulations have been run to generate internal events from two of the most significant backgrounds, ^{214}Bi and ^{208}Tl. Both of these isotopes can contribute events to the ROI, given that their $Q_\beta > Q_{\beta\beta}$. One contributor to these backgrounds is the source foil contamination. ^{214}Bi and ^{208}Tl are naturally occurring in the uranium and thorium decay chains respectively. Another source is radon gas, which, if present in the detector, can deposit its daughters on the tracker wires and source foil surfaces. Analysis to measure the sensitivity to these backgrounds was conducted using the 1e1α control channels. To reach a sensitivity equivalent

to the the target value of 2 µBq/kg for ^{208}Tl, an exposure of ≈ 5 weeks is required. For a sensitivity to the target 20 µBq/kg for ^{214}Bi, an exposure of ≈ 100 weeks is required.

Relative errors on activity measurements were also calculated using simulated data. The inputted foil bulk activities were varied to find results for the SuperNEMO target, the most recent upper value from BiPo-3 and the RnCL, and a central measurement from BiPo-3. Taking the worst case activity for the ^{214}Bi bulk a relative error of 10% would be found after an exposure of ≈ 60 days. For the tracker activity, assuming that radon is flushed at a rate of 2.0 m^3/h, a relative error of 10% can be achieved with an exposure of ≈ 180 days and 20% with an exposure of ≈ 150 days for the surface activity. Finally for ^{208}Tl, assuming an input activity of 370 µBq and a combined ^{214}Bi activity of 6.38 mBq, a 10% relative error could be found after ≈ 40 days. The combined ^{214}Bi activity could be measured down to a relative error of 5% in ≈ 5 days. In conclusion, the identification of these control channels allows for the measurement of important background to the $0\nu\beta\beta$ process with relatively short exposures.

With the ongoing commissioning of the detector underway, the SuperNEMO gas system plays a crucial role in ensuring the safe running and continuous supply of the correct mixture of gas. As described above, radon suppression to the target level can only be reached with a flow rate of 2.0 m^3/h. The developments to the system, including the addition of a central control system, allows for both manual and remote adjustments and monitoring of the status. A method for measuring the ethanol present in the BP was developed, tested and deployed. The monitoring software has been linked with SuperNEMO's CMS, and collaboration members are recording the variations in pressure, temperature and ethanol levels. Key requirements were early warning of faults and that the system can be stabilised until an engineer can attend; this has been achieved.

Bibliography

[1] G. A. et al., *nEXO: neutrinoless double beta decay search beyond 10^{28} year half-life sensitivity*, Journal of Physics G: Nuclear and Particle Physics **49** (dec, 2021) 015104.

[2] J. M.-A. et al., *Sensitivity of NEXT-100 to neutrinoless double beta decay*, Journal of High Energy Physics **2016** (may, 2016) . https://doi.org/10.1007%2Fjhep05%282016%29159.

[3] M. J. Dolinski, A. W. Poon, and W. Rodejohann, *Neutrinoless Double-Beta Decay: Status and Prospects*, Annual Review of Nuclear and Particle Science **69** (Oct, 2019) 219–251. http://dx.doi.org/10.1146/annurev-nucl-101918-023407.

[4] J. Chadwick, *The intensity distribution in the magnetic spectrum of beta particles from radium (B + C)*, Verh. Phys. Gesell. **16** (1914) 383–391.

[5] W. Pauli, *Dear radioactive ladies and gentlemen*, Phys. Today **31N9** (1978) 27.

[6] E. Fermi, *An attempt of a theory of beta radiation.*, Z.Phys. **88** (1934) 161–177.

[7] C. L. Cowan, F. Reines, F. B. Harrison, H. W. Kruse, and A. D. McGuire, *Detection of the Free Neutrino: a Confirmation*, Science **124** (1956) no. 3212, 103–104. http://science.sciencemag.org/content/124/3212/103.

[8] T. D. Lee and C. N. Yang, *Question of Parity Conservation in Weak Interactions*, Phys. Rev. **104** (Oct, 1956) 254–258. https://link.aps.org/doi/10.1103/PhysRev.104.254.

[9] C. S. Wu, E. Ambler, R. W. Hayward, D. D. Hoppes, and R. P. Hudson, *Experimental Test of Parity Conservation in Beta Decay*, Phys. Rev. **105** (Feb, 1957) 1413–1415. https://link.aps.org/doi/10.1103/PhysRev.105.1413.

[10] M. Goldhaber, L. Grodzins, and A. W. Sunyar, *Helicity of Neutrinos*, Phys. Rev. **109** (Feb, 1958) 1015–1017. https://link.aps.org/doi/10.1103/PhysRev.109.1015.

[11] G. Danby, J.-M. Gaillard, K. Goulianos, L. M. Lederman, N. Mistry, M. Schwartz, and J. Steinberger, *Observation of High-Energy Neutrino Reactions and the Existence of Two Kinds of Neutrinos*, Phys. Rev. Lett. **9** (Jul, 1962) 36–44. https://link.aps.org/doi/10.1103/PhysRevLett.9.36.

[12] M. L. e. a. Perl, *Evidence for Anomalous Lepton Production in $e^+ - e^-$ Annihilation*, Phys. Rev. Lett. **35** (Dec, 1975) 1489–1492 https://link.aps.org/doi/10.1103/PhysRevLett.35.1489.

[13] K. K. et. al., *Observation of tau neutrino interactions*, Physics Letters B **504** (2001) no. 3, 218 – 224. http://www.sciencedirect.com/science/article/pii/S0370269301003070.

[14] *Precision electroweak measurements on the Z resonance*, Physics Reports **427** (2006) no. 5, 257 – 454. http://www.sciencedirect.com/science/article/pii/S0370157305005119.

[15] B. Pontecorvo, *Mesonium and anti-mesonium*, Sov. Phys. JETP **6** (1957) 429. [Zh. Eksp. Teor. Fiz.33,549(1957)].

[16] J. Davis, Raymond, D. S. Harmer, and K. C. Hoffman, *Search for neutrinos from the sun*, Phys.Rev.Lett. **20** (1968) 1205–1209.

[17] Z. Maki, M. Nakagawa, and S. Sakata, *Remarks on the unified model of elementary particles*, Prog.Theor.Phys. **28** (1962) 870–880.

[18] B. Pontecorvo, *Neutrino Experiments and the Problem of Conservation of Leptonic Charge*, Sov. Phys. JETP **26** (1968) 984–988. [Zh. Eksp. Teor. Fiz.53,1717(1967)].

[19] SNO, Q. R. Ahmad et al., *Direct evidence for neutrino flavor transformation from neutral current interactions in the Sudbury Neutrino Observatory*, Phys. Rev. Lett. **89** (2002) 011301.

[20] Super-Kamiokande, Y. Fukuda et al., *Evidence for oscillation of atmospheric neutrinos*, Phys. Rev. Lett. **81** (1998) 1562–1567.

[21] B. Kayser, *Neutrino Physics*, . https://arxiv.org/abs/hep-ph/0506165.

[22] J. Schechter and J. Valle, *Neutrino Masses in SU(2) × U(1) Theories*, Phys.Rev. **D22** (1980) 2227.

[23] F. Capozzi, E. D. Valentino, E. Lisi, A. Marrone, A. Melchiorri, and A. Palazzo, *Addendum to "Global constraints on absolute neutrino masses and their ordering"*, Physical Review D **101** (jun, 2020) . https://doi.org/10.1103%2Fphysrevd.101.116013.

[24] Particle Data Group, M. Tanabashi et al., *Review of Particle Physics*, Phys. Rev. **D98** (2018) no. 3, 030001.

[25] R. N. Cahn, D. A. Dwyer, S. J. Freedman, W. C. Haxton, R. W. Kadel, Y. G. Kolomensky, K. B. Luk, P. McDonald, G. D. O. Gann, and A. W. P. Poon, *White Paper: Measuring the Neutrino Mass Hierarchy*, 2013. https://arxiv.org/abs/1307.5487.

[26] J. Mott, *Search for double beta decay of 82Se with the NEMO-3 detector and development of apparatus for low-level radon measurements for the SuperNEMO experiment.* PhD thesis, University Coll. London, 2013-09-25. http://www.hep.ucl.ac.uk/theses/James_Mott_Thesis.pdf.

[27] E. Majorana, *Theory of the Symmetry of Electrons and Positrons*, Nuovo Cim. **14** (1937) 171–184.

[28] C. Giunti and C. W. Kim, *Fundamentals of Neutrino Physics and Astrophysics*. Oxford University Press, 03, 2007. https://doi.org/10.1093/acprof:oso/9780198508717.001.0001.

[29] M. Thomson, *Modern particle physics*, ch. 17.8, pp. 495–497. Cambridge University Press, New York, 2013. http://www-spires.fnal.gov/spires/find/books/www?cl=QC793.2.T46::2013.

[30] G. Drexlin, V. Hannen, S. Mertens, and C. Weinheimer, *Current direct neutrino mass experiments*, Adv. High Energy Phys. **2013** (2013) 293986.

[31] KATRIN Collaboration, *KATRIN: A next generation tritium beta decay experiment with sub-eV sensitivity for the electron neutrino mass*, 2001. https://arxiv.org/abs/hep-ex/0109033.

[32] KATRIN, M. Arenz et al., *First transmission of electrons and ions through the KATRIN beamline*, JINST **13** (2018) no. 04, P04020.

[33] C. Kraus, B. Bornschein, L. Bornschein, J. Bonn, B. Flatt, et al., *Final results from phase II of the Mainz neutrino mass search in tritium beta decay*, Eur.Phys.J. **C40** (2005) 447–468.

[34] Troitsk Collaboration, V. Aseev et al., *An upper limit on electron antineutrino mass from Troitsk experiment*, Phys.Rev. **D84** (2011) 112003.

[35] M. A. et al., *Improved Upper Limit on the Neutrino Mass from a Direct Kinematic Method by KATRIN*, Physical Review Letters **123** (nov, 2019) . https://doi.org/10.1103%2Fphysrevlett.123.221802.

[36] KATRIN, M. Aker et al., *Direct neutrino-mass measurement with sub-electronvolt sensitivity*, Nature Phys. **18** (2022) no. 2, 160–166.

[37] *The effect of massive neutrinos on the matter power spectrum*, Mon. Not. R. Astron. Soc. **410** (January, 2011) 1647–1654. https://doi.org/10.1111/j.1365-2966.2010.17546.x.

[38] P.-D. et al., *Hints, neutrino bounds, and WDM constraints from SDSS DR14 Lyman-α and Planck full-survey data*, Journal of Cosmology and Astroparticle Physics **2020** (apr, 2020) 038–038. https://doi.org/10.1088%2F1475-7516%2F2020%2F04%2F038.

[39] Zen Collaboration, *First Search for the Majorana Nature of Neutrinos in the Inverted Mass Ordering Region with KamLAND-Zen*, . https://arxiv.org/abs/2203.02139.

[40] M. Agostini, G. Benato, J. A. Detwiler, J. Menéndez, and F. Vissani, *Toward the discovery of matter creation with neutrinoless double-beta decay*,

2022. https://arxiv.org/abs/2202.01787.

[41] C. F. V. Weizsacker, *Zur Theorie der Kernmassen*, Z. Phys. **96** (1935) 431–458.

[42] K. Krane, *Introductory Nuclear Physics*. Wiley, 1987. https://books.google.co.uk/books?id=ConwAAAAMAAJ.

[43] M. Goeppert-Mayer, *Double beta-disintegration*, Phys.Rev. **48** (1935) 512–516.

[44] F. T. Avignone, S. R. Elliott, and J. Engel, *Double beta decay, Majorana neutrinos, and neutrino mass*, Rev. Mod. Phys. **80** (2008) 481–516. http://link.aps.org/doi/10.1103/RevModPhys.80.481.

[45] W. H. Furry, *On transition probabilities in double beta-disintegration*, Phys. Rev. **56** (1939) 1184–1193.

[46] Y. Chikashige, R. Mohapatra, and R. Peccei, *Are there real goldstone bosons associated with broken lepton number?*, Physics Letters B **98** (1981) no. 4, 265–268. https://www.sciencedirect.com/science/article/pii/0370269381900113.

[47] T. Noblet, *Background studies and design optimisation of the SuperNEMO demonstrator module : search for $2\nu\beta\beta$ and $0\nu\beta\beta$ decays of 116Cd into the excited states of 116Sn with NEMO-3*. PhD thesis, 09, 2017. http://nile.hep.utexas.edu/DocDB/ut-nemo/docs/0045/004520/001/thesisFinalVersionDocDB.pdf.

[48] S.-F. Ge, M. Lindner, and S. Patra, *New physics effects on neutrinoless double beta decay from right-handed current*, JHEP **10** (2015) 077.

[49] M. Doi, T. Kotani, H. Nishiura, and E. Takasugi, *DOUBLE BETA DECAY*, Prog.Theor.Phys. **69** (1983) 602.

[50] R. A. et al., *Probing New Physics Models of Neutrinoless Double Beta Decay with SuperNEMO*, Eur. Phys. J. **70** (2010) 927–943.

[51] J. D. Vergados, H. Ejiri, and F. Š imkovic, *Theory of neutrinoless double-beta decay*, Reports on Progress in Physics **75** (sep, 2012) 106301. https://doi.org/10.1088%2F0034-4885%2F75%2F10%2F106301.

[52] NEMO-3, R. Arnold et al., *Results of the search for neutrinoless double-β decay in ^{100}Mo with the NEMO-3 experiment*, Phys. Rev. D **92** (2015) no. 7, 072011.

[53] SNO+, V. Lozza, *Background analysis for the SNO+ experiment*, J. Phys. Conf. Ser. **1468** (2020) no. 1, 012135.

[54] S. I. Alvis, I. J. Arnquist, F. T. Avignone, A. S. Barabash, C. J. Barton, V. Basu, F. E. Bertrand, B. Bos, M. Busch, M. Buuck, and et al., *Search for neutrinoless double- Îš decay in Ge76 with 26 kg yr of exposure from the Majorana Demonstrator*, Physical Review C **100** (Aug, 2019) . http://dx.doi.org/10.1103/PhysRevC.100.025501.

[55] GERDA Collaboration, M. e. a. Agostini, *Final Results of GERDA on the Search for Neutrinoless Double-β Decay*, Phys. Rev. Lett. **125** (Dec, 2020) 252502. https://link.aps.org/doi/10.1103/PhysRevLett.125.252502.

[56] G. C. et al., *Searching for neutrinoless double beta decay with GERDA*, . https://arxiv.org/abs/1710.07776.

[57] I. J. e. a. Arnquist, *Final Result of the MAJORANA DEMONSTRATOR's Search for Neutrinoless Double- Decay in ^{76}Ge*, 2022. https://arxiv.org/abs/2207.07638.

[58] LEGEND, A. J. Zsigmond, *LEGEND: The future of neutrinoless double-beta decay search with germanium detectors*, J. Phys. Conf. Ser. **1468** (2020) no. 1, 012111.

[59] E. Fiorini and T. O. Niinikoski, *Low Temperature Calorimetry for Rare Decays*, Nucl. Instrum. Meth. A **224** (1984) 83.

[60] C. Collaboration, *Search for Majorana neutrinos exploiting millikelvin cryogenics with CUORE*, Nature **604** (apr, 2022) 53–58. https://doi.org/10.1038%2Fs41586-022-04497-4.

[61] C. Alduino, K. Alfonso, D. Artusa, F. A. III, O. Azzolini, M. Balata, T. Banks, G. Bari, J. Beeman, F. Bellini, and et al., *CUORE-0 detector: design, construction and operation*, Journal of Instrumentation **11** (Jul, 2016) P07009–P07009. http://dx.doi.org/10.1088/1748-0221/11/07/P07009.

[62] O. Azzolini, J. Beeman, F. Bellini, M. Beretta, M. Biassoni, C. Brofferio, C. Bucci, S. Capelli, L. Cardani, P. Carniti, and et al., *Final Result of CUPID-0 Phase-I in the Search for the Se82 Neutrinoless Double- Îš Decay*, Physical Review Letters **123** (Jul, 2019) . http://dx.doi.org/10.1103/PhysRevLett.123.032501.

[63] O. e. a. Azzolini, *Final Result on the Neutrinoless Double Beta Decay of ^{82}Se with CUPID-0*, 2022. https://arxiv.org/abs/2206.05130.

[64] E. A. et al., *New Limit for Neutrinoless Double-Beta Decay of ^{100}Mo from the CUPID-Mo Experiment*, Physical Review Letters **126** (may, 2021) . https://doi.org/10.1103%2Fphysrevlett.126.181802.

[65] The CUPID Interest Group, *CUPID pre-CDR*, 2019. https://arxiv.org/abs/1907.09376.

[66] KamLAND-Zen, Y. Gando, *First results of KamLAND-Zen 800*, J. Phys. Conf. Ser. **1468** (2020) no. 1, 012142.

[67] KamLAND-Zen, J. Shirai, *Results and future plans for the KamLAND-Zen experiment*, J. Phys. Conf. Ser. **888** (2017) no. 1, 012031.

[68] SNO+, E. Caden, *Status of the SNO+ Experiment*, J. Phys. Conf. Ser. **1342** (2020) no. 1, 012022.

[69] SNO+, A. S. Inácio, *Status and Prospects of the SNO+ Experiment*, PoS **PANIC2021** (2022) 274.

[70] Sno+, E. Leming, *SNO+: Current Results and Future Prospects*, PoS **NOW2018** (2019) 027.

[71] EXO-200, R. Gornea, *Double beta decay in liquid xenon*, J. Phys. Conf. Ser. **179** (2009) 012004.

[72] G. Anton, I. Badhrees, P. Barbeau, D. Beck, V. Belov, T. Bhatta, M. Breidenbach, T. Brunner, G. Cao, W. Cen, and et al., *Search for Neutrinoless Double-Beta Decay with the Complete EXO-200 Dataset*, Physical Review Letters **123** (Oct, 2019) . http://dx.doi.org/10.1103/PhysRevLett.123.161802.

[73] NEXT Collaboration, *Sensitivity of a tonne-scale NEXT detector for*

neutrinoless double beta decay searches, 2020. https://arxiv.org/abs/2005.06467.

[74] NEMO-3, R. Arnold et al., *Detailed studies of ^{100}Mo two-neutrino double beta decay in NEMO-3*, Eur. Phys. J. C **79** (2019) no. 5, 440.

[75] NEMO-3, R. Arnold et al., *Search for the double-beta decay of ^{82}Se to the excited states of ^{82}Kr with NEMO-3*, Nucl. Phys. A **996** (2020) 121701.

[76] P. Povinec, *Background constrains of the SuperNEMO experiment for neutrinoless double beta-decay searches*, Nuclear Instruments and Methods in Physics Research Section A: Accelerators, Spectrometers, Detectors and Associated Equipment **845** (06, 2016) .

[77] P. P. Povinec, *Background constrains of the SuperNEMO experiment for neutrinoless double beta-decay searches*, Nuclear Instruments and Methods in Physics Research Section A: Accelerators, Spectrometers, Detectors and Associated Equipment **845** (2017) 398–403. https://www.sciencedirect.com/science/article/pii/S0168900216306684. Proceedings of the Vienna Conference on Instrumentation 2016.

[78] SuperNEMO, A. Jeremie and A. Remoto, *The SuperNEMO $\beta\beta$ source production*, PoS **ICHEP2016** (2017) 1018.

[79] SuperNEMO, A. S. Barabash et al., *The BiPo-3 detector for the measurement of ultra low natural radioactivities of thin materials*, JINST **12** (2017) no. 06, P06002.

[80] C. F. Vilela, *Search for $\beta\beta$-decay of ^{4}8Ca in NEMO-3 and commissioning of the tracker for the SuperNEMO experiment.* PhD thesis, University College London, 2014. https://discovery.ucl.ac.uk/id/eprint/1457059/1/cv_thesis_v2_web.pdf.

[81] A. B. et al., *Calorimeter development for the SuperNEMO double beta decay experiment*, Nuclear Instruments and Methods in Physics Research Section A: Accelerators, Spectrometers, Detectors and Associated Equipment **868** (oct, 2017) 98–108. https://doi.org/10.1016%2Fj.nima.2017.06.044.

[82] B. Guillon, *Magnetic Coil Prodution*, Internal Document - NemoDocDB-doc-5191-v1, May, 2020.

[83] E. Chauveau, *SuperNEMO demonstrator status for LSM users meeting*, Internal Document - NemoDocDB-doc-5536-v3, January, 2022.

[84] C. Bourgeois, *Status of shielding design*, Internal Document - NemoDocDB-doc-4878-v1, March, 2019.

[85] M. Hoballah, *Cobalt Analysis: Time Calibraiton and Time Resolution of the Calorimeter*, Internal Document - NemoDocDB-doc-5429-v2, May, 2021.

[86] W. Quinn, *SuperNEMO Poster Neutrino 2022*, Internal Document - NemoDocDB-doc-5567-v1, May, 2022.

[87] X. Aguerre, *Poster "Energy calibration of the SuperNEMO calorimeter"*, Internal Document - NemoDocDB-doc-5558-v1, April, 2022.

[88] SuperNEMO, R. Arnold et al., *Measurement of the distribution of ^207Bi depositions on calibration sources for SuperNEMO*, JINST **16** (2021) no. 07, T07012.

[89] M. Macko, *Simulations of Bi-207 Energy Calibration Spectrum (First Results)*, Internal Document - NemoDocDB-doc-5178-v2, April, 2020.

[90] E. Chauveau, *DO (Detector Operation) meeting - report from week 25*, Internal Document - NemoDocDB-doc-5584-v1, June, 2022.

[91] E. Chauveau, *First Tracker+Calorimeter commissioning data*, Internal Document - NemoDocDB-doc-5485-v1, September, 2021.

[92] E. Chauveau, *Summary of autumn 2021 tracker commissioning*, Internal Document - NemoDocDB-doc-5532-v1, December, 2021.

[93] E. Chauveau, *Detector Operation meeting - week 34*, Internal Document - NemoDocDB-doc-5481-v1, August, 2021.

[94] E. Chauveau, *Demonstator Status*, Internal Document - NemoDocDB-doc-5597-v1, July, 2022.

[95] Tosaka, *Uranium 238 decay chain*, Dec, 2008. https://commons.wikimedia.org/wiki/File:Decay_chain(4n%2B2,_Uranium_series).PNG.

[96] Tosaka, *Thorium 232 decay chain*, Dec, 2008.

https://commons.wikimedia.org/wiki/File:Decay_chain(4n,Thorium_series).PNG.

[97] P.Loaiza, *Source foils measurements with BiPo*, Internal Document - NemoDocDB-doc-4505-v1, Nov, 2017.

[98] X. R. Liu, *Radon Mitigation Strategy and Results for the SuperNEMO Experiment*, Internal Document - NemoDocDB-doc-4119-v2, June, 2016.

[99] *Falaise GitHub Repository*, https://github.com/SuperNEMO-DBD/Falaise.

[100] *Cadfael GitHub Repository*, https://github.com/SuperNEMO-DBD/homebrew-cadfael.

[101] CERN, *An object oriented framework for large scale data analysis.*, http://root.cern.ch/drupal/ **Version 5.26** .

[102] CERN, *Platform for the simulation of the passage of particles through matter using Monte Carlo methods*, http://geant4.cern.ch .

[103] *Bayeux GitHub Repository*, https://github.com/BxCppDev/Bayeux.

[104] O. Ponkratenko, V. Tretyak, and Y. Zdesenko, *The Event generator DECAY4 for simulation of double beta processes and decay of radioactive nuclei*, Phys.Atom.Nucl. **63** (2000) 1282–1287.

[105] S. Calvez, *Development of reconstruction tools and sensitivity of the SuperNEMO demonstrator*. PhD thesis, 09, 2017. https://tel.archives-ouvertes.fr/tel-01632815.

[106] C. Patrick, *Sensitivity Module GitHub Repository*, https://github.com/SuperNEMO-DBD/SensitivityModule.

[107] T. L. Noblet, *Alpha Finder GitHub Repository*, https://github.com/lenoblet/AlphaFinder.

[108] S. Torre, *SuperNEMO sensitivity to Tl and Bi events*, Internal Document - NemoDocDB-doc-2174-v2, Mar, 2012.

[109] A. Jeremie, *82Se foil position in SuperNEMO demonstrator*, Internal Document - NemoDocDB-doc-4457-v5, April, 2021.

[110] F.Xie, *Radon Background Studies for the SuperNEMO Experiment*. PhD thesis, University College London, https://discovery.ucl.ac.uk/id/eprint/10124094, 2021.

[111] *TFractionFitter Class Reference*, https://root.cern.ch/doc/v606/classTFractionFitter.html.

[112] M. Instruments, *Digital Mass Flow Controller Type 1179B / 1479B / 2179B and Digital Mass Flow Meter 179B - Instruction Manual* -. MKS Instruments Deutschland GmbH, MKS Instruments, U.K. Ltd. 1 Anchorage Court Caspian Road Altrincham, Cheshire WA14 5HH, England, June, 2010.

[113] M. I. D. GmbH, *PR 4000B-F 2 Channel Power Supply and Readout for Flow and Pressure Instruction Manual*. MKS Instruments, 1 Anchorage Court, Caspian Road, Altrincham, Chesire, WA14 5HH, England, 2010-11-23 ed., November, 2010.

[114] X. Liu, *Low background techniques for the SuperNEMO experiment*. PhD thesis, University College London, January, 2017. https://discovery.ucl.ac.uk/id/eprint/1544146/9/XinRanLiu_Thesis.pdf.

[115] C. Vilela, *Pressure fluctuations at LSM*, Internal Document - NemoDocDB-doc-2161-v1, 2012.

[116] D. GmbH, *Saturated Vapor Pressure*, September, 2017. http://ddbonline.ddbst.com/AntoineCalculation/AntoineCalculationCGI.exe?component=Ethanol.

[117] T. Haake, *Instruction Manual Circulator DC30/DL30 including all Baths Instruction Manual Circulator DC30/DL30 including all Baths Instruction Manual Circulator DC30/DL30 including all Baths*. Thermo Haake, Dieselstraße 4, D-76227 Karlsruhe, January, 2002.

[118] T. Scientific, *Thermo Scientific EK45/EK90 Immersion Coolers*, 2016. https://www.marshallscientific.com/v/vspfiles/files/manuals/EK45.pdf.

[119] L. C.R and S. K., *RS232 - A synchronous communications adapter supporting speeds up to 64,000 bps*. Barr Systems, Gainesville, FL 32614-7015, 1988.

[120] R. P. Foundation, *Raspberry PI 2 Model B*, https://www.raspberrypi.org/products/raspberry-pi-2-model-b/.

[121] Adafruit, *Pimoroni Pan-Tilt HAT for Raspberry Pi - without pan-tilt module*, https://www.adafruit.com/product/3353?gclid=CjwKCAjwmK3OBRBKEiwAOL6t1GvE12uDpo0ZdKuCQ7jHWqnTMirg4upaWGRvLs_1oGeIDECbjVp34RoCzSUQAvD_BwE.

[122] T. Le Flour, J. Panazol, and E. Chabanne, *MOS (Multipurpose OPCUA Server) User Guide*. LAPP, August, 2015.

[123] E. Chabanne, *SuperNEMO Control and Monitoring System*, Internal Document - NemoDocDB-doc-4084-v2, 2016.

[124] Prosys OPC, *Prosys OPC UA Client - User Manual*, v2.2 ed., July, 2014.

[125] Adafruit, *Python code to use the ADS1015 and ADS1115 analog to digital converters with a Raspberry Pi or BeagleBone black.*, https://github.com/adafruit/Adafruit_Python_ADS1x15.

[126] K. AG, *EV-94 Operating Manual*. Druckmesstechnik, St. Gallerstrasse 119, CH-8404 Winterthur, January, 2001.

[127] L. L, *Cron Job: A Comprehensive Guide for Beginners 2022*, https://www.hostinger.com/tutorials/cron-job.